Kinetic and Mechanistic Studies of the Oxygen Reduction Reaction on Platinum Electrocatalysts

by

Sean T. Dix

A dissertation submitted in partial fulfillment
of the requirements for the degree of
Doctor of Philosophy
(Chemical Engineering)
in the University of Michigan
2022

Doctoral Committee:

Professor Suljo Linic, Chair
Assistant Professor Bryan Goldsmith
Assistant Professor Charles McCrory
Assistant Professor Nirala Singh

Sean T. Dix

sdix@umich.edu

ORCID iD: 0000-0002-2880-8058

© Sean T. Dix 2022

To David Covell, my grandfather. Who never got to read this work but always believed I would complete it.

Acknowledgements

I would like to thank all my friends, family, and colleagues who supported and inspired me over the past five years.

Thank you to my research advisor, Professor Suljo Linic. I joined Suljo's group wanting to expand my experimental skills in heterogeneous catalysis while still using computational methods. I was also inspired to join by the impressive resumes of his former students and the success they had. What I did not expect to find was an expert communicator, a master multi-disciplinarian in chemical physics and engineering and the ultimate advocate for his student's success. I have personally developed leaps and bounds in my presentation skills, writing skills, and research acumen under Suljo's advising. Thank you for bearing with me in my stubbornness and giving me great opportunities to succeed. I would also like to thank my committee members: Professor Bryan Goldsmith, Professor Charles McCrory and Professor Nirala Singh. Thank you for your insights and feedback to make this dissertation the best it can be. I greatly appreciate the time you put into my PhD work the past four years.

Thank you to the wonderful lab mates I have had over the years: Paul Hernley, Umar Aslam, Joseph Quinn, Valentina Igenegbai, Steven Chavez, Vishal Rao, Ali Motagamwala, Dongho Lee, John Hemmerling, Rawan Almallahi, Rachel Elias, Jacques Esterhuizen, James Wortman, Shawn Lu, Aarti Mathur, Shiuan-Bai Ann, Han-Ting Chen and Claire Yin. I have greatly enjoyed working with you all and have many fond memories of lab get-togethers, especially all the potlucks at my place. Everyone is so quick to help when asked and I have

needed a lot of help! Suljo really knows how to pick them as you are all so hard working, intelligent, and kind. A special thanks to Paul, Umar, Steven, Vishal and Ali who provided training and key insights that helped me publish.

I would like to thank my parents Mom and Pop and my sister Sarah. You have been very supportive of me the past few years even though a lot of tragedy has occurred with Mom losing both her parents and the life changing medical problems we've experienced. Through the hardest times in the past five years, we have always stuck together and supported each other as a family and that makes me so proud. In a more positive vein, during this time, Sarah moved to Michigan and Shelby and I got married. I have loved living next-door to my sister for the past few years and I feel like we have grown much closer than ever before. Thank you, Mom, for being the most empathetic and caring person I know and Pop for inspiring me and guiding me to be an excellent researcher. I hope we can all spend more time together in the future and that the next five years will be full of joy.

I want to thank my lunch crew Hannah Kim, John Hemmerling, Luke Bugada and Abdulla Alqubati. I can't tell you how many times Shelby asked me what my favorite part of my workday was and I said "lunch". I have so many fond memories including the fierce debates about Star Wars, rediscovering our couch, and Luke's blueberry. Of course, you four are some of the best friends I made while I was here and we have so many memories made from going to the cabin, to Canada, and Cleveland. I hope we can stay in touch for a long time and make more memories together.

I would also like to thank my church family from the Detroit Church of Christ. It has been an amazing blessing to be part of such a loving, caring and hospitable group of people bound by the love of Christ. I could write 30 different names of people who have impacted my

time here, but I would like to give a special thanks to Ben and Jen Weatherston, Kyle and Kristin Eastman, Chad and Kate Talo, Shon Harris, Derek Stache, and Michael Michaud. You all have a very special place in my heart.

There are a few more people I would like to acknowledge that have had a great impact on where I am today. I would like to thank Dr. Veronica Price, my 11th grade chemistry teacher whose class exposed me to chemistry for the first time and sparked the interest in science that eventually led to this dissertation. I would like to thank Professor Rachel Getman, my undergraduate research advisor. There may be no one mentioned above that had a greater impact on me pursuing a PhD. You made research fun and accessible and you gave me so much flexibility and input on the project. I think I texted you more than anyone during my time at Clemson! I can really thank you for helping me find my love of computational methods and reaction mechanisms. I hope all the success for you. I would also like to thank Essence Robinson, the “best woman” at my wedding and one of my oldest and most loyal friends. Thank you for your unending support.

Finally, I would like to thank my bride Shelby whom my love for language has little power in conveying. I will simply say thank you for your patience and your love.

Table of Contents

Dedication ii

Acknowledgements iii

List of Tables ix

List of Figures x

Abstract xv

Chapter 1 Introduction 1

1.1 Summary 1

1.2 Effects of Fossil Fuel Consumption 1

1.3 Role of Fuel Cells 7

1.4 The Role of Catalysis in Hydrogen Fuel Cells 11

1.5 Overview of Previous Work 13

1.6 Scope of Dissertation 14

1.7 References 15

Chapter 2 Experimental and Computational Methods 20

2.1 Summary 20

2.2 Electrochemical Methods 20

2.2.1 3-Electrode Cell 20

2.2.2 Rotating Disk Electrode 22

2.2.3 Measuring Solution Resistance 24

2.2.4 Capacitive Current Measurements 25

2.2.5 Rotating Ring Disk Electrode 27

2.3 Syntheses 30
2.3.1 60 nm Ag Nanoparticles 30
2.3.2 60 nm Ag-Pt Core-Shell Nanoparticles 31
2.4 In-situ Raman Electrochemical Flow Cell 31
2.4.1 Raman Spectroscopy 32
2.4.2 In-situ Flow Cell 34
2.4.3 Statistical Analysis 36
2.5 Ab-Initio Calculations 37
2.5.1 VASP basics 38
2.5.2 Calculating Lattice Constants 39
2.5.3 Optimizing Surface Slabs 42
2.5.4 Vibrational Mode Calculations 45
2.6 References 46
Chapter 3 Evaluation of Electrocatalyst Activity 48
3.1 Introduction 48
3.2 Electrocatalytic Activity as a Figure of Merit 49
3.3 Measuring Electrocatalyst Activity using Rotating Disk Electrodes 50
3.4 Techniques for Characterizing ECSA 58
3.4.1 Underpotential Deposition 58
3.4.2 Carbon Monoxide (CO) Stripping 61
3.4.3 Baseline-Corrected H_{UPD} Measurements 62
3.5 Conclusion 65
3.6 References 65
Chapter 4 Microkinetic Modeling in Electrocatalysis 70
4.1 Introduction 70

4.2 Developing MK Models in Thermal vs. Electrochemical Systems 74
4.3 Predictive Power and Uncertainties Associated with MK Modeling 79
4.4 Spectroscopy as Complementary Tool 85
4.5 Conclusions 87
4.6 References 87
Chapter 5 In-operando Probing of the ORR Mechanism on Pt Nanoparticles 97
5.1 Introduction 97
5.2 Synthesis and Characterization of Ag-Pt Core-Shell Nanoparticles 100
5.3 Spectroscopic Results and Discussion 104
5.4 Conclusions 119
5.5 References 120
Chapter 6 Conclusions and Future Directions 126
6.1 General Conclusions 126
6.2 Future Directions 126
6.3 References 130

List of Tables

Table 2.1 Mass limiting currents at different RRDE rotation speeds and the calculated collection efficiencies. 30

Table 2.2 Vibrational mode frequencies (in cm^{-1}) for 1/9 ML O_2 on 3x3 Pt(111) calculated using the dynamical matrix method or IBRION=5 and oxygen-16 or oxygen-18. 45

Table 3.1 Parameters used in the Thiele modulus equation..... 55

Table 5.1 Vibrational mode frequencies (in cm^{-1}) of O_2 in 1/3 ML H_2O 1/3 ML OH with O-16 or O-18 oxygens in O_2. 112

Table 5.2 Vibrational mode frequencies (in cm^{-1}) of OOH in H-down facing 2/3 ML H_2O with O-16 or O-18 oxygens in OOH. 112

List of Figures

Figure 1.1 World population with synthetic fertilizers and estimated population without synthetic fertilizers. Adapted from reference 1 and 2. 3

Figure 1.2 Molecular vibrations for carbon monoxide. (a) is the symmetric stretch, (b) is the asymmetric stretch and (c-d) are the degenerate bending mode. From reference 4. 4

Figure 1.3 Radiative flux and distribution of wavelengths for light coming towards the earth (yellow) and leaving the earth (red). From reference 5. 5

Figure 1.4 Worldwide energy consumption since 1800. From reference 7. 6

Figure 1.5 (left) World life expectancy over time. Adapted from reference 8 and 9. (right) percent of world population living in extreme poverty. Extreme poverty is defined by the United Nations as living on less than 1.9-international $ a day. Adapted from reference 3 and 10. 6

Figure 1.6 (left) Worldwide annual CO_2 emissions from fossil fuel usage. Adapted from reference 11. (right) Global atmospheric concentration of CO_2. Adapted from reference 12 and 13..... 7

Figure 1.7 U.S. Energy consumption with sources on the left and utilizing sectors on the right. For the year 2020. From reference 20. 8

Figure 1.8 Schematic of a hydrogen fuel cell. 9

Figure 1.9 Reaction energy diagram for A→B with and without a catalyst..... 12

Figure 2.1 Schematic of 3-electrode cell 20

Figure 2.2 Typical IV curve for the ORR on a Pt rotating disk electrode in oxygen saturated electrolyte..... 23

Figure 2.3 Resistance vs. frequency during a hybrid impedance spectroscopy measurement of a Pt electrode in 0.1 M NaOH 25

Figure 2.4 Cyclic voltammogram of Pt nanoparticles on carbon black in Ar saturated 0.1 M NaOH 26

Figure 2.5 Schematic of a rotating disk ring electrode 27

Figure 2.6 Example of RRDE in operation during ORR 28

Figure 2.7 Variations in limiting current with respect to rotation rate. In black is the current measured at the ring and in red is the current measured at the disk. The ring is held at a potential of 1.1 V while the disk varies potential from 0.75 to -0.25 V. The reduction begins around 0.3 V where it is then limited at lower potentials. 29

Figure 2.8 Diagram of Rayleigh, Stokes Raman, and anti-Stokes Raman scattering..... 32

Figure 2.9 Diagram of LSPR on a metal nanoparticle..... 34

Figure 2.10 Schematic of the in-situ flow cell during normal operation. He or O_2 is bubbled into both reservoirs simultaneously. The reference electrode is contained in one of the electrolyte reservoirs and the counter electrode is contained within the spectroelectrochemical cell. 36

Figure 2.11 One Raman data point at 750 mV in He saturated electrolyte in blue. In yellow and green are two gaussian line forms centered around 1600 and 1664 cm^{-1} fitted to the blue data. This fitting has an $R^2 = 0.92$. 37

Figure 2.12 NxNxN k-point values on bulk Pt energy 41

Figure 2.13 Optimization of bulk Pt lattice constant. In blue is the initial set of constants and red is a more focused region. 42

Figure 2.14 A 3x3 Pt(111) surface slab. The four catalytic sites (FCC, HCP, ATOP, and Bridge) are marked..... 43

Figure 2.15 Optimal K-point configuration for a 3x3 Pt(111) slab 44

Figure 3.1 Tafel plot of the ORR current density for a Pt-poly electrode rotating at 1600 RPM in O_2 saturated 0.1 M NaOH. Currents are corrected for solution resistance loses and the capacitive current from the electrochemical double layer. 54

Figure 3.2: (a) RDE linear sweep voltammograms for a Pt-poly electrode in oxygen saturated 0.1 M NaOH at 1600 RPM. An effectiveness factor model is imposed on the data to simulate the effects of various Thiele moduli. As the Thiele modulus increases, the electrode requires a greater overpotential to reach the mass limiting current. (b) Effects of the Thiele modulus on the kinetic current measured at 0.9 V vs. RHE and (c) at 0.8 V vs. RHE using a model from the literature. 57

Figure 3.3 H_{UPD} analysis for a pure Pt (yellow) and Pt monolayer electrocatalyst (blue) developed within our group. The H_{UPD} peak is integrated from 0.05 to 0.40 V vs RHE using either a constant or slanted baseline shown by the dotted lines. CV curves were obtained in Ar saturated 0.1 M $HclO_4$ using a scan rate of 50 mV/s without electrode rotation. 60

Figure 3.4 CO stripping voltammogram (scan rate: 10 mV/s) for Pt/C and Pt-monolayer electrocatalyst in Ar saturated 0.1 M $HClO_4$ electrolyte under no rotation. Raw currents are shown as dashed lines while the background subtracted currents are shown as solid lines. 62

Figure 3.5 ORR specific activities for the different ECSA measuring protocols. Results for both the novel and standard Pt electrocatalyst are shown in blue and yellow respectively. Error bars represent the standard deviation of the ECSA measurements. 63

Figure 3.6 RDE linear sweep voltammograms for a Pt-poly electrode in oxygen saturated 0.1 M NaOH at 1600 RPM. In black is the properly normalized IV curve using equation 6 (in the case of Pt-poly electrode $A_{ECSA} = A_{RDE}$). The dotted green line represents a normalized IV curve derived if the magnitude of A_{ECSA} is underestimated to 50 % of the real value and the full green line represents a normalized IV curve assuming a two-fold overestimated A_{ESCA}. 64

Figure 4.1(a) Calculated Tafel slopes and (b) reaction orders with respect to the concentration of $[H^+]$ for the ORR on Pt as a function of the OH^* coverage. Different lines correspond to the assumptions of different rate determining steps. 76

Figure 4.2 (a) Reaction order (Ψ_A) and reversibility (z_{ads} defined as: $r - i, jri, j$) of a simple $A + A \leftrightarrow A2$ reaction with respect to the rate constant (k_{ads}) for the adsorption of A calculated with Langmuir Hinshelwood (0^{th}-order), 1^{st}-order and KMC models. (b) Comparison of steady-state surface coverages and TOFs for CO-oxidation on RuO_2(110) calculated with phenomenological kinetics and (c) with KMC. (d) Steady-state TOFs at the edges of a 5.2 nm truncated octahedron calculated with KMC for CO-oxidation with and without neighboring (100) and (111) facets... 82

Figure 5.1(a) Energy-dispersive X-ray spectroscopy (EDS) map of the Ag-Pt nanoparticle. Ag is pink while Pt signal is green. (b) ORR current(rate)/voltage curve measured for the Ag-Pt nanoparticles at 50 mV/s in the in-operando flow cell in 0.1 M NaOH with O_2 (red) or He (black) saturating the electrolyte. (Inset) Electrochemical surface area normalized ORR current measured in a rotating disk electrode (RDE) setup of the Ag-Pt on carbon and monometallic Ag spheres on carbon. The kinetic current was measured at 0.9 V vs. RHE in O_2 saturated 0.1 M NaOH. (c) Raman spectra of methylene blue (MB) on a silica chip with and without the Ag-Pt nanoparticles or Pt nanoparticles (~ 20 nm diameter). The MB was deposited on the three substrates at identical concentration. The Raman laser wavelength was 532 nm. (d) UV-vis extinction spectra of the Ag nanoparticle (60 nm diameter) and the identical Ag particles covered by a thin Pt shell..... 100

Figure 5.2 (a) Dark-Field STEM image of a Ag-Pt nanocube edge showing a Pt shell of 0.93 nm around a silver core. (b) Bright-Field STEM image of a single Ag-Pt nanosphere where a thin Pt shell of 0.95 nm around the Ag core can be seen. (c) Dark-field STEM image of an 80 nm edge length Ag-Pt nanocube. (d) EDS elemental line scan taken across the center of a Ag-Pt nanocube showing the elemental composition of the core and shell with Pt counts represented in red and black for Ag. 101

Figure 5.3 Tafel curves for Ag/C, and Ag-Pt/C at 1600 RPM in O_2 saturated 0.1 M NaOH. Each curve is corrected for capacitive currents and solution resistance. 102

Figure 5.4 Electrochemical surface area normalized current measured on a Pt-poly electrode, 60 nm Ag-Pt/C, and 60 nm Ag spheres at 0.9 V vs. RHE in O_2 saturated 0.1 M NaOH measured using conventional rotating disk electrodes. 3 data points were taken for each catalyst. 103

Figure 5.5 FDTD modeling of a 60 nm Ag core, 1 nm Pt shell nanoparticle exposed to incident 532 nm laser in water. The heat map shows up to 35-fold electric field intensity enhancement $(E/E_0)^2$. 104

Figure 5.6 (a) Measured in-operando PER spectra of Ag-Pt nanoparticles in O_2 and He saturated 0.1 M NaOH at electrode voltages from 50 to 900 mV vs. RHE. (b) Statistical analysis of potential dependent intensity changes for oxygen sensitive bands of peaks at 933, 1072, 1102, 1131, 1404, and 1441 cm^{-1}. Error bars are ± the standard error of the population mean of n spectra taken for each potential where n is a minimum of 3. (c) The arrows represent the DFT calculated movement of atoms corresponding to different Raman vibrational modes. A 3x3 surface unit cell was employed. 105

Figure 5.7 In-operando measurements of 60 nm Ag spheres in 0.1 M NaOH. The Ag spheres show large amounts of potential dependence that could be its own study. Most interesting is the strong potential dependence of peaks around 700 cm^{-1} that does not show up for Ag-Pt. In general, the most intense peak is ~10x the intensity of Ag-Pt's which is to be expected as pure Ag spheres have higher electric field enhancements at their surface. The Ag-Pt spectra is shown in black at 50 mV for comparison..... 106

Figure 5.8 Simulated potential dependent electrified Pt(111)/electrolyte interfaces. Specific DFT models are created based on ab-initio thermodynamic calculations found before vibrational analysis is performed to create a database of possible vibrational modes found with experiment. (a) 2/3 ML H_2O + 1ML H-UPD. (b) 2/3 ML H_2O. (c) 1/3ML-OH/1/3ML-H_2O and 5/12ML-OH/3/12ML-H_2O. (d) 1/4 ML O. 108

Figure 5.9 Operando Raman spectra of the Ag-Pt nanoparticles in 0.1 M NaOH at (a) 50 mV and (b) 900 mV where bubbled O_2-16 is in black and O_2-18 is in red. 111

Figure 5.10 (a) 1/9 ML O_2 adsorbed in a bridge site on a 3x3 Pt(111) surface. (b) DFT calculated Raman modes with oxygen masses of 16 in the left column and 18 in the right column..... 113

Figure 5.11 (a) Measured in-operando PER spectra of Ag-Pt nanoparticles in O_2 and He saturated 0.1 M NaOH from 50 to 900 mV vs. RHE. (b) Statistical analysis of potential dependent changes for oxygen insensitive modes at 1600, 1664, and 2020 cm^{-1}. Error bars are ± the standard error of the population mean of n spectra taken for each potential where n is a minimum of 3. (c) The arrows represent the DFT calculated movement of atoms corresponding to different Raman vibrational modes. A 3x3 surface unit cell was employed. 113

Figure 5.12 (Left) In-situ PERS measurements of CO on Ag-Pt nanoparticles in CO saturated 0.1 M NaOH. Two distinct CO peaks appear in the region between 1900 and 2100 wavenumbers. These peaks shift to higher wavenumber at higher potential. (Right) In-situ measurements on the Ag-Pt nanoparticles in the CO-free, oxygenated electrolyte for comparison. We ascribe this spectrum to H on Pt..... 115

Figure 5.13 (a) Integrated band intensities of Raman peaks at 2854 and 2933 cm^{-1} in O_2 (red) and He (black). When O_2 concentrations are high in the electrolyte, no clear trend is observed with respect to potential. When O_2 is absent, the two peaks appear to reach a maximum size at 500 mV before decreasing in intensity. The band at 2933 cm^{-1} could not be detected at 50 mV

without oxygen present in the electrolyte. Error bars are ± the standard error of the population mean of n spectra taken for each potential where n is a minimum of 3. (b) DFT calculated vibrational modes associated with the Raman active movement of H_2O on the Pt surface. Molecule perturbations are indicated with blue arrows for each simulated peak. 116

Figure 5.14 Potential energy surface for various intermediates of the ORR on Pt derived from the PERS data. High potential is consistent with ~750-900 mV while low potential refers to ~50-500 mV. The red barriers indicate kinetically relevant steps that trap reactant intermediates on the Pt surface allowing for spectroscopic detection. 118

Figure 6.1 HOR exchange current densities for various metal electrocatlaysts with respect to hydrogen binding energy and pH. Adapted from ref [5]. 129

Abstract

Hydrogen fuel cells are promising devices that can be utilized as a carbon-neutral mobile energy source. These devices can produce electric power from pressurized hydrogen gas and oxygen from the air with only water as a by-product. However, the adoption of this technology has been hampered by its poor technoeconomic performance, especially at scale. The high costs arise from the expensive platinum group metal catalysts needed to speed up the rate of the oxygen reduction reaction (ORR) at the fuel cell cathode. Efforts to improve the catalytic performance focus on novel electrocatalyst design (through metal alloying, nanostructuring, etc.) and understanding the mechanism of ORR at the elementary step level under relevant reaction conditions. The former relies on accurate measures of catalytic activity but is hampered by incorrect measurements of active catalytic area and mass transport limitations. The latter has proven challenging as mechanistic analyses (in particular: spectroscopic analysis of relevant surface intermediates) are confounded by solvent and electric field effects.

The first scope of this thesis is to establish fundamental tools and methods to accurately quantify catalyst activity. A modeling example shows the impact on the catalyst film construction and how a thin, conductive film is required to eliminate internal mass transport limitations. Different surface area measurements are discussed, with examples demonstrating the effects of improper surface area characterization. The accurate measurement of catalyst activity is essential for any novel catalyst design studies and mechanistic studies vying to explain observed catalyst performance from elementary steps.

The second scope of this thesis pertains to mechanistic analyses of electrochemical reactions and the ORR specifically. Microkinetic modeling is one tool that can be used to explain macroscopic observables (such as reaction orders and Tafel slopes) by solving a system of elementary rate equations with certain initial conditions based on the chemical environment. The accuracy of these models is heavily impacted by the inherent assumptions such as the mean-field approximation and the treatment of the electrochemical potential, solvent effects, electric field effects, and ion/electrolyte effects. The accuracy of these models can be improved by advanced modeling techniques such as kinetic Monte Carlo and through in-situ/operando spectroscopy. To demonstrate, this work presents an in-operando study of the ORR that sheds light on the potential-dependent mechanism. A unique spectroscopic platform to probe the electrified Pt surface at realistic reaction conditions is created to accomplish this. A non-model Ag-Pt core-shell nanoparticle is synthesized and characterized with UV-vis spectroscopy, and STEM with elemental mapping showing a distinct core-shell architecture. Localized surface plasmons resonance enables plasmon-enhanced Raman spectroscopy (PERS) measurements at the reactive and electrified Pt/electrolyte interface. Data analysis shows how experimental spectra matches with density functional theory (DFT) derived vibrational modes to shed light on the reaction mechanism. The vibrational model assignments are further verified and validated by isotopic labeling studies. This analysis reveals critical insights on the ORR mechanism, showing a crowded network of OH/H_2O at low overpotentials We also present evidence of an OOH species adsorbed on a cleaner surface at high overpotentials. These insights can be adopted as design criteria for future electrocatalyst optimizations and increase the accuracy of microkinetic models. Furthermore, the spectroscopic platform can be expanded to other chemistries to yield fundamental insights into electrochemical reaction mechanisms.

Chapter 1 Introduction

1.1 Summary

This section describes the motivation for researching fuel cells, their background, and their workings, along with the challenges for commercialization. A broad view on the global effects of human fossil fuel consumption is presented as well as how fuel cells help mitigate its negative impacts. The basics of electrochemistry and catalysis are described, and basic cell design is presented with a focus on low temperature hydrogen fuel cells and their performance relative to internal combustion engine vehicles and battery electric vehicles. The technoeconomic limitations of current hydrogen fuel cell technologies are discussed and possible routes for improvement are highlighted. A focus on previous work in improving fuel cell efficiency is also presented. Finally, an outline of the remainder of the dissertation is presented along with the work's scope.

1.2 Effects of Fossil Fuel Consumption

In the 18^{th} to 20^{th} centuries, a confluence of three separate, but related, phenomena was occurring:

1. The proliferation of heat engines
2. The ability to synthesize fertilizer at large scales
3. The understanding of how light interacts with gaseous molecules

The invention of the steam engine in the 18^{th} century and subsequent mass adoption in the 19^{th} century resulted in a great increase in economic productivity due to their ability to convert chemical energy into mechanical work. Steam engines rely on the burning of fossil fuels, such as

coal, to produce heat that is imparted to steam to run mechanical devices. The basic (unbalanced) chemical reaction of combustion is listed below:

$C_xH_y + O_2 \rightarrow CO_2 + H_2O$

Where C_xH_y can be a variety of molecules called hydrocarbons. The combustion reaction for one of the most common hydrocarbons, methane (primary component of natural gas), is shown below:

$CH_4 + 2O_2 \rightarrow CO_2 + 2H_2O$

Where each molecule of methane (CH_4) is reacted with 2 molecules of oxygen to form one molecule of carbon dioxide and 2 molecules of water. This reaction releases large amounts of heat (~800 kJ for a mol of methane), and since it occurs spontaneously after an initial spark, can heat water continuously to produce steam and drive the engine.

This invention was revolutionary in that it enabled both large-scale manufacturing, such as in textiles, but also laid the groundwork for electric power generation though steam powered turbines and electrical generators. This technology, and subsequent innovations, had the effect of greatly increasing the average quality of life for mankind, especially when considering the manufacturing of medicines, building materials, and ease of transportation.

The second important phenomenon that occurred during this period was the invention of the Haber-Bosch process to produce synthetic fertilizers. This process converts nitrogen from the air into ammonia, the main component of fertilizer, through the following reaction:

$N_2 + 3H_2 \rightarrow 2NH_3$

Where one molecule of nitrogen reacts with 3 molecules of hydrogen to form 2 molecules of ammonia. Before the mass production of synthetic fertilizer using the Haber-Bosch process, fertilizer was derived from manure, compost, or other naturally derived sources such as mineral deposits. With the Haber-Bosch process, fertilizer could be produced on an industrial scale and

crop yields across the world became more consistent and prolific. The effect of this invention can be seen in Figure 1.1[1,2] where soon after the first industrial scale plant using the Haber-Bosch process opened in 1913, the world population exploded due to the increased access to reliable crop yields.

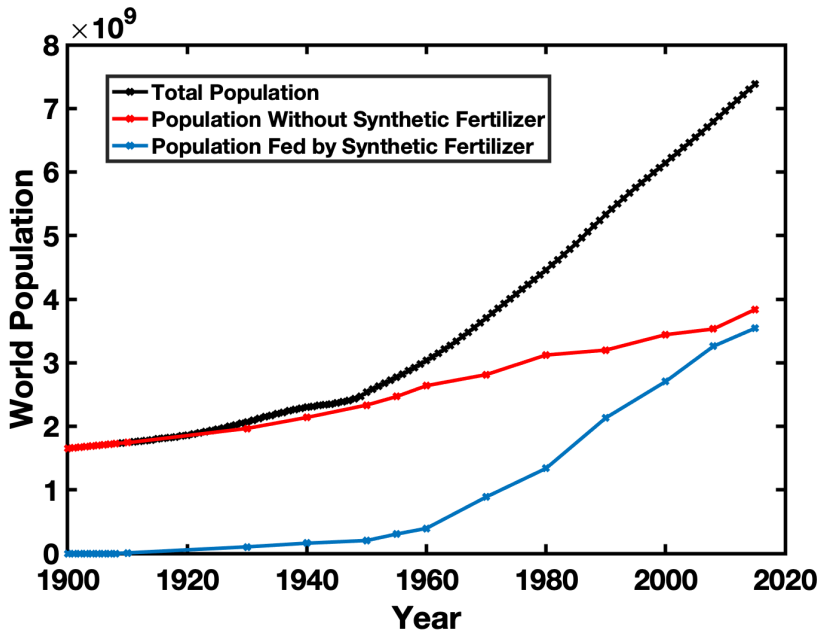


Figure 1.1 World population with synthetic fertilizers and estimated population without synthetic fertilizers. Adapted from reference 1 and 2.

The first two phenomena can be simplified to be an increase in the quality and quantity (through the large increase in population) of life. These effects are multiplicative in theory, though it should be noted that quality of life improvements have not been equally distributed across the globe[3]. However, the rapid development of the economies of China and India over the last 30 years, for example, demonstrates how the most populous developing countries are quickly increasing the quality of life of their citizens.

The third and possibly most crucial phenomenon to this dissertation is how light from the sun interacts with gaseous molecules such as carbon dioxide. Gaseous molecules, such as oxygen, nitrogen and carbon dioxide contain chemical bonds that connect their constituent elements. For

oxygen and nitrogen, a double and triple bond connect the two oxygen and nitrogen atoms respectively. For carbon dioxide, two oxygen atoms surround a central oxygen atom connected by two double bonds. These molecules vibrate at different frequencies due to their unique geometries. For oxygen and nitrogen, the linear molecules have only one vibrational mode called the symmetric stretch where the atoms move towards and away from each other like an accordion. Carbon dioxide, however, has 3 additional vibrational modes as seen in Figure 1.2[4].

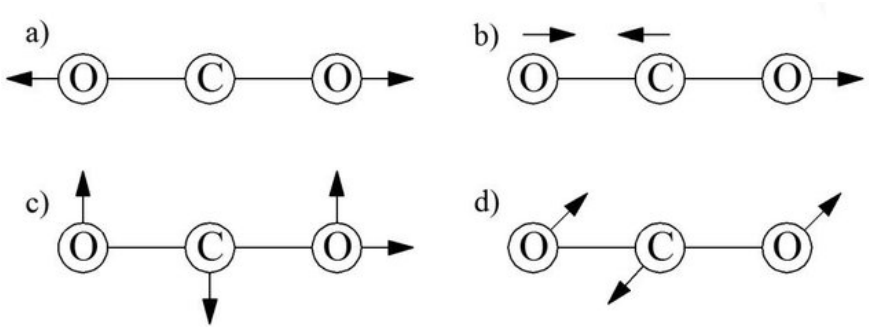


Figure 1.2 Molecular vibrations for carbon monoxide. (a) is the symmetric stretch, (b) is the asymmetric stretch and (c-d) are the degenerate bending mode. From reference 4.

When light at a particular wavelength interacts with a carbon dioxide molecule, the molecule begins to vibrate. For the asymmetric stretch and degenerate bending modes (shown as b, c and d in Figure 1.2) this wavelength is 15 μm and 4.2 μm respectively. After absorption of light, the bonds vibrate, and the molecule enters an excited state. This excited state is unfavorable, however, and the molecule will return to its ground state and radiate light in all directions. This is relevant to the motivations of this dissertation due to the relationship between the carbon dioxide in the atmosphere and the effect that has on the Earth's surface temperature. The Earth is constantly being bombarded with high energy light from the sun, which is absorbed by the Earth and heats it up. This heat (like the heat from a stove) is radiated back out into space and follows a wavelength distribution as seen in Figure 1.3[5].

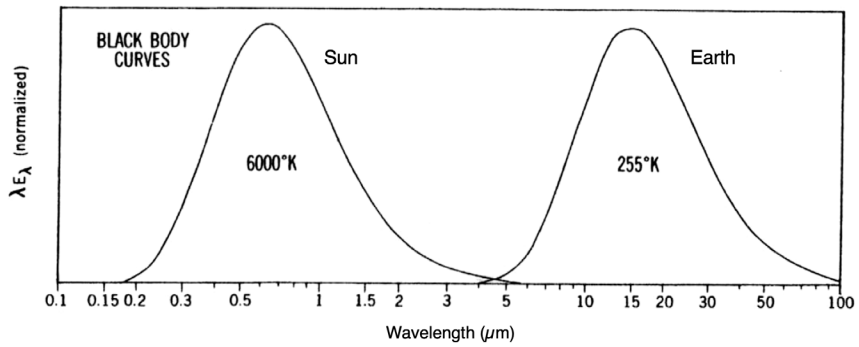


Figure 1.3 Radiative flux and distribution of wavelengths for light coming towards the earth (yellow) and leaving the earth (red). From reference 5.

Notice that the radiative flux leaving the earth peaks around 15 μm and covers a significant range from 4 to 100 μm. This light (thermal radiation) that is radiated by the earth can interact with the asymmetric stretch (15 μm) of carbon dioxide in the atmosphere and be "reflected" back towards the earth. This is in essence what is happening due to the so-called "greenhouse gas effect," which has the effect of trapping heat in Earth's atmosphere. The effect of the amount of carbon dioxide could have on Earth's climate was not posited until 1896 by Swedish chemist (and great (x5) academic parent of this author) Svante Arrhenius. Based on Arrhenius' calculations in 1896, a doubling of the atmospheric carbon dioxide concentration would lead to a 5-6 ºC (9-11 ºF) increase in surface temperatures[6]. Notably, this was well after the development and proliferation of fossil fuel burning heat engines and the increase in standard of living they were beginning to bring.

The effects of these three phenomena bring us to our current state of affairs described in Figure 1.4, Figure 1.5, and Figure 1.6 [3,7–13].

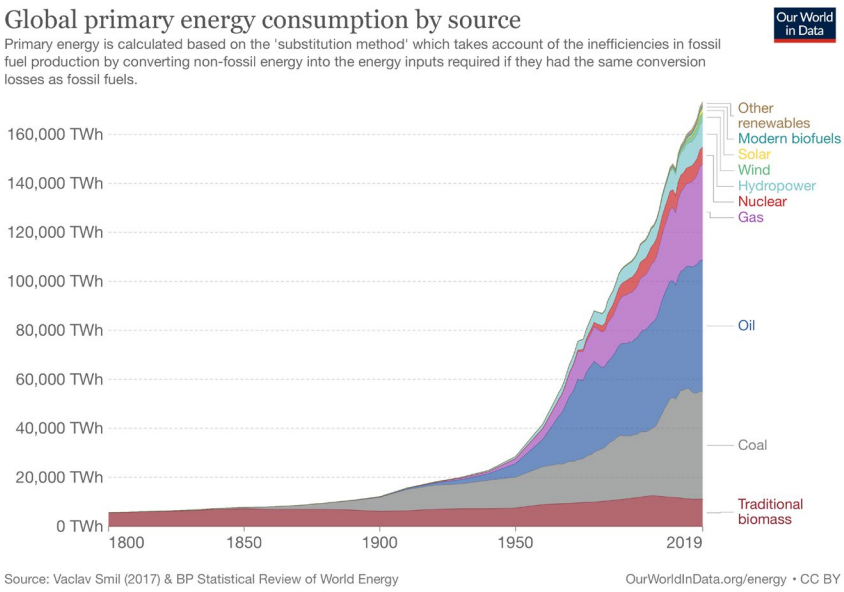


Figure 1.4 Worldwide energy consumption since 1800. From reference 7.

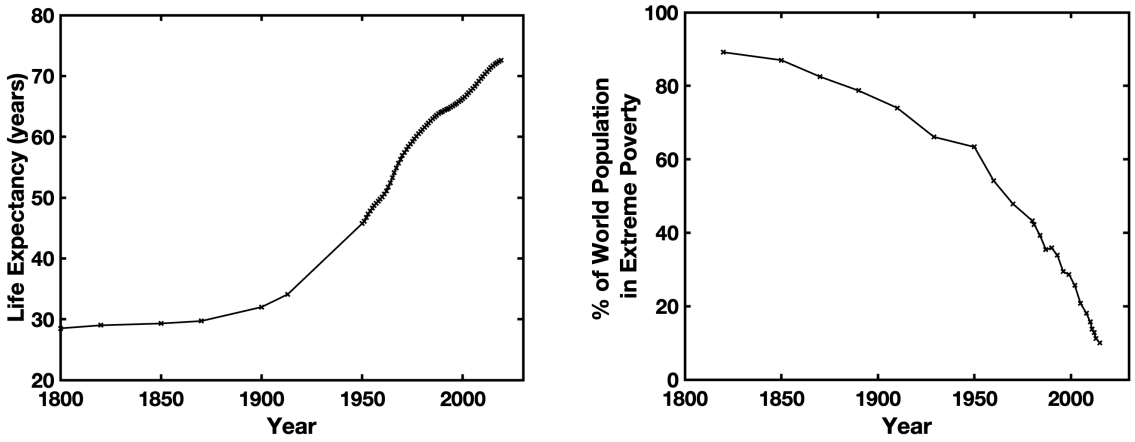


Figure 1.5 (left) World life expectancy over time. Adapted from reference 8 and 9. (right) percent of world population living in extreme poverty. Extreme poverty is defined by the United Nations as living on less than 1.9-international $ a day. Adapted from reference 3 and 10.

Figure 1.4 and Figure 1.5 show a strong correlation between energy consumption and the rise of human life expectancy and the decline of extreme poverty in the past 200 years. A significant portion of this increased quality of life can be attributed to the Haber-Bosch process and the associated increase in food security. The Haber-Bosch process itself, however is very energy intensive and makes up an estimated 1% of global energy consumption[14]. These amazing achievements in increased life expectancy and diminished poverty wrought by the science and

engineering of the past two centuries have come with their own costs. The vast majority of the energy consumed (see Figure 1.4) has been derived from the burning of fossil fuels (oil, coal and natural gas). Due to the burning of these fossil fuels, an immense and increasing amount of carbon dioxide is being released into the atmosphere each year (Figure 1.6). This has had the effect to increase the concentration of carbon dioxide in the atmosphere by ~130 ppm since 1800, an almost 50% increase. The year 1800 is selected as a benchmark since the measured CO_2 concentration of 280 ppm has been relatively stable at this level for the past 2000 years[13].

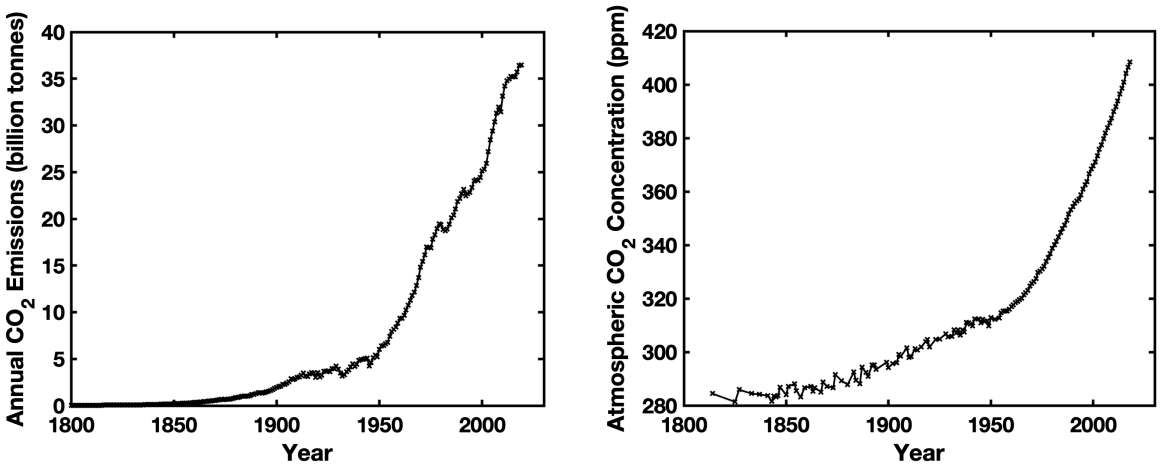


Figure 1.6 (left) Worldwide annual CO_2 emissions from fossil fuel usage. Adapted from reference 11. (right) Global atmospheric concentration of CO_2. Adapted from reference 12 and 13.

Besides the primary effect of increased global temperatures predicted by Arrhenius, the secondary effects of increased CO_2 in the atmosphere have been discussed at length elsewhere[15–19]. In short, increased concentrations of CO_2 in the atmosphere have been linked to ocean acidification, rising sea levels, extreme heat, ecological disruptions, and more.

1.3 Role of Fuel Cells

To tackle the monumental challenge of transitioning our energy sources from carbon producing to carbon neutral or even carbon negative, alternative energy technologies targeted at specific sectors are required. Figure 1.7 shows the energy balance for the United States in 2020 detailing where

the total energy consumed was sourced and what sectors utilize these sources[20]. Looking at the sources on the left, 35% of energy came from petroleum, 34% from natural gas, 12% renewables, 10% coal and 9% nuclear. Taking nuclear as an example, 100% of energy produced using nuclear went to the electric power generation sector, which is then distributed to the sectors shown on the right.

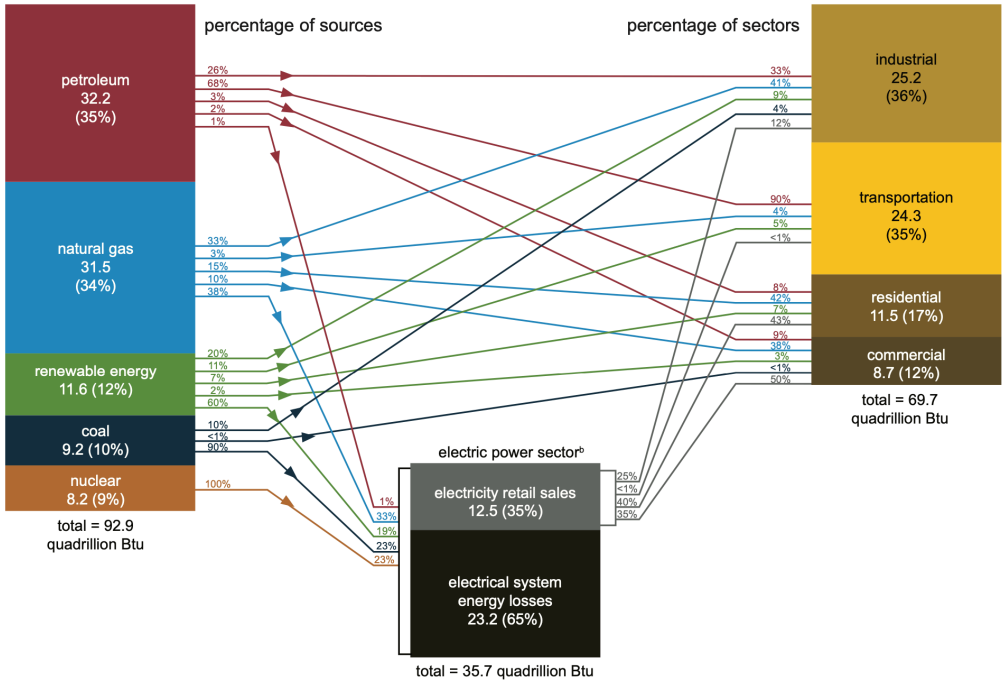


Figure 1.7 U.S. Energy consumption with sources on the left and utilizing sectors on the right. For the year 2020. From reference 20.

Of interest to this dissertation, the transportation sector used 35% of the nation's total energy consumption or 24.3 quadrillion Btu. Of this energy, 90% was sourced from petroleum. Internal combustion engine vehicles (ICE) burn this petroleum (gasoline and diesel fuel) and convert the mixture of hydrocarbons to carbon dioxide, water, and heat to run the vehicles. Targeting the transportation sector for carbon mitigation is attractive due to the ubiquity of internal combustion engines throughout the sector and its large (35%) share of total energy consumed. Alternatives to ICE vehicles have been researched, with the main two competitors being fuel cell electric vehicles (FCEV) and battery electric vehicles (BEV).

Fuel cells are electrochemical devices that convert chemical energy from a fuel into electrical energy that can be used to power an electrical device such as a passenger vehicle or truck. Hydrogen fuel cells, which use hydrogen gas as the fuel, are the most common type of fuel cells. More specifically, the most common hydrogen fuel cell used is the proton exchange membrane fuel cell or PEM fuel cell. A basic schematic of a PEM hydrogen fuel cell is shown in Figure 1.8.

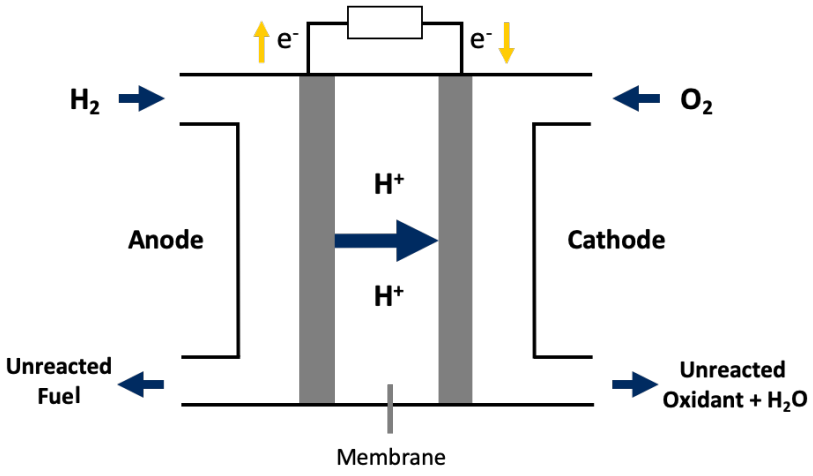


Figure 1.8 Schematic of a hydrogen fuel cell.

On one side of the fuel cell, called the anode, hydrogen gas reacts to form 2 protons and 2 electrons following this reaction (hydrogen oxidation):

$H_2 \rightarrow 2H^+ + 2e^-$

The protons travel through a selective proton conducting membrane and the electrons travel through an external circuit, with both finishing on the other side of the cell called the cathode. At the cathode, oxygen reacts with the electrons and protons to form water through the following reaction (oxygen reduction):

$O_2 + 4e^- + 4H^+ \rightarrow 2H_2O$

The overall reaction for the hydrogen fuel cell is:

$2H_2 + O_2 \rightarrow 2H_2O$

This reaction is exergonic (releases energy) at room temperature by releasing high-energy electrons from the cell. This can be seen by the individual free energies of the anodic and cathodic reactions (also known as half-reactions). For the hydrogen oxidation reaction, the standard reaction potential (at standard conditions) is 0 V vs. RHE (Reversible hydrogen electrode. This reaction is where 0 V is defined on the RHE scale. All voltages are with respect to RHE unless otherwise stated.) while for the oxygen reduction reaction the standard potential is 1.23 V. The potential, i.e. the voltage, can be converted in free energy through the Nernst equation:

$$E = \frac{-\Delta G}{nF}$$

Where ΔG is the free energy, n is the number of electrons transferred, and F is a constant called Faraday's constant. The maximum energy an electrochemical cell can produce is the potential at the cathode minus the potential at the anode ($E_{cathode} - E_{anode}$). For a hydrogen fuel cell this is 1.23 V – 0 V or 1.23 V. Using the Nernst equation, the maximum energy derived from reacting one mol of hydrogen in a hydrogen fuel cell is 237 kJ.

The advantage of hydrogen fuel cells is that they can produce electrons to drive an electric motor without producing carbon dioxide. This, however, assumes that the hydrogen fuel itself is produced without making carbon dioxide (so called "green hydrogen"). Currently, ~95% of hydrogen is produced as "grey hydrogen" through methane steam reforming and the water gas shift reaction which releases 1 molecule of CO_2 for every 4 molecules of hydrogen produced[21]. Green hydrogen can be produced with water electrolysis to split water into oxygen and hydrogen gas using renewable energy or sunlight and is its own active research area worldwide and in the Linic group[22]. Even when sourcing the hydrogen from natural gas (grey hydrogen), FCEVs still produce much less CO_2/mile driven than the average vehicle. For example, the Toyota Mirai FCEV

produces 278 gCO_2/mile vs. 504 gCO_2/mile for the sales-weighted fleet average of personal vehicles in the United States[23].

1.4 The Role of Catalysis in Hydrogen Fuel Cells

The value of 237 kJ that can be derived from reacting one mol of hydrogen in a fuel cell is a purely thermodynamic calculation. Thermodynamics tells us what *can* happen but not what *will* happen, and 1.23 V is the maximum amount of voltage that can be derived from the fuel cell. To determine what will happen, or, to be more precise, what will *probably* happen, we must turn to kinetics. Kinetics, and in this case chemical kinetics, describes the frequency of which a chemical event will occur given the thermodynamic constraints. When mixing gasoline and oxygen at room temperature very little gasoline will combust (so little it is not noticeable). However, mix gasoline and water at 1000 ºC and the mixture will react violently. Thermodynamically, both reactions are favorable (at room temperature and at 1000 ºC) but kinetically, the reaction happens much faster at higher temperatures. Temperature is not the only way to speed up reactions. Materials called catalysts can also speed up reactions by lowering the barrier for the reaction to occur. To illustrate how catalysts work, we consider a simple reaction A → B as seen in Figure 1.9.

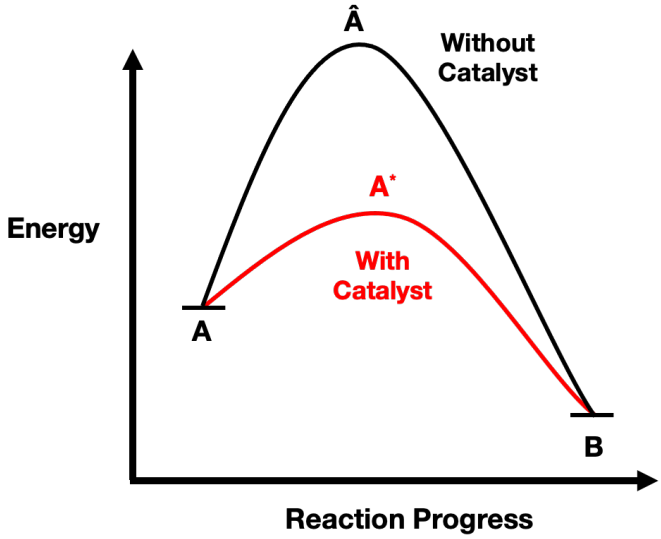


Figure 1.9 Reaction energy diagram for A→B with and without a catalyst

For the reaction to proceed, it must go through a transition state of higher energy. This is marked as Â in Figure 1.9. A catalyst will lower the energy of this transition state (also called the activation barrier) to make the reaction proceed more quickly. The reaction rate constant can be described through the Arrhenius equation:

$$k = Ae^{-\left(\frac{E_a}{RT}\right)}$$

Where k is the reaction rate constant (tells the frequency of a reaction event), A is a pre-exponential factor, R is the universal gas constant, T is the temperature and E_a is the activation barrier. For our simple example in Figure 1.9, E_a is the energy difference between Â and A. From this equation, the exponential dependence of the activation barrier on the rate constant can be seen.

For hydrogen fuel cells, catalysts are required at both the anode and cathode to run the cell at maximum power. For PEM fuel cells specifically, the anodic hydrogen oxidation reaction (HOR) has a very low activation barrier and thus requires little amounts of catalyst. The cathodic oxygen reduction reaction (ORR), however, has a large barrier and requires large amounts of catalyst (around twice as much as the anode). The catalysts at both the anode and cathode are platinum (Pt)

based as it is the most stable and active pure metal in the acidic conditions of PEM fuel cells[24]. Pt, however, represents a major limiting factor in the technoeconomic evaluation of PEM fuel cells because of its high costs and scarcity[25]. One analysis indicated that the cost of the ORR catalyst becomes >40% of the total fuel cell cost at mass production volumes (>500,000 units a year)[26]. Due to the large amounts of expensive catalysts required, FCEVs today are considerably more expensive than the comparable ICE vehicle. As of 2021, there are only two FCEV you can purchase in the U.S.:

1. 2021 Toyota Mirai sedan: $49,500
2. 2021 Hyundai Nexo crossover: $58,935

Both the Mirai and the Nexo are around twice as expensive as the average new vehicle in their class, which makes this technology non-competitive for the average consumer.

1.5 Overview of Previous Work

To increase adoption of hydrogen fuel cells, the cost of the cathodic catalyst needs to decrease. Broadly, this can be achieved in two main ways:

1. Increase the activity of the expensive catalyst
2. Replace the expensive catalyst material with cheaper materials

Increasing the activity of the expensive catalyst (and therefore necessitating less of it to achieve equivalent power densities) has been researched by many groups and consists of tailoring the electronic structure of Pt through alloying it with other metals or nanostructuring the Pt catalyst[27–35]. The second approach has also been heavily investigated, albeit with less success, and has focused on replacing platinum with cheaper metals such as silver or utilizing metal-free catalysts[36–40]. Knowing which parameters to change in order to increase catalyst activity is an active area of research and is discussed further in of Chapters 4 and 5.

1.6 Scope of Dissertation

This dissertation covers tools and analyses for improving ORR electrocatalysts through mechanistic analysis starting from the best practices for quantification of electrocatalyst activity to how this activity originates through elementary processes.

Chapter 2 contains descriptions of experimental and computational methods used throughout the dissertation. For the experimental section, a focus is placed on fundamental electrochemical techniques needed to do impactful work on electrocatalysis: from the basics of the three-electrode cell to measuring ORR selectivity. In-situ spectroscopic techniques are also covered and how they can be used to evaluate reaction mechanisms. Computational techniques, with a focus on quantum chemistry tools, are covered. Special attention is paid to the consistent use of these methods to yield reliable results.

Chapter 3 contains a discussion on critical practices for evaluating electrocatalyst activity. A discussion of current literature trends is provided followed by examples and modeling showing the effect of poor thin-film construction for rotating disk measurements and improper surface area calculations. Recommendations for the best practices in measuring electrocatalyst surface area are also provided.

Chapter 4 describes how using microkinetic modeling can be used to derive insights on electrocatalyst mechanisms. Common challenges of microkinetic modeling for electrochemical systems are discussed and ways to overcome them are presented. A brief discussion on how in-situ/in-operando spectroscopic analysis can inform microkinetic models and the tools available to researchers is also included.

Chapter 5 describes an in-operando study of the ORR on Pt nanoparticles to derive mechanistic insights for electrocatalyst design criteria. The nanoparticle design and synthesis is shown along

with materials characterizations. Raman measurements using a dye molecule demonstrate the viability of the platform for an in-operando study. Raman data is collected using a flow cell and is paired with computationally derived vibrational spectra to identify active coverages at various potentials. Finally, a potential dependent reaction landscape is presented with insights on future electrocatalyst design.

Chapter 6 concludes the dissertation and describes future work that can build off the insights derived from the proceeding chapters.

1.7 References

(1) How many people does synthetic fertilizer feed? https://ourworldindata.org/how-many-people-does-synthetic-fertilizer-feed (accessed 2021 -09 -13).

(2) Erisman, J. W.; Sutton, M. A.; Galloway, J.; Klimont, Z.; Winiwarter, W. How a Century of Ammonia Synthesis Changed the World. *Nature Geosci* **2008**, *1* (10), 636–639. https://doi.org/10.1038/ngeo325.

(3) Ravallion, M. *The Economics of Poverty: History, Measurement, and Policy*; Oxford University Press: New York, 2016. https://doi.org/10.1093/acprof:oso/9780190212766.001.0001.

(4) Olbrycht, R.; Kałuża, M.; Wittchen, W.; Borecki, M.; Więcek, B.; Mey, G. Gas Identification and Estimation of Its Concentration in a Tube Using Hyperspectral Thermography Approach; 2016. https://doi.org/10.21611/qirt.2016.095.

(5) Brunetti, M.; Prodi, F. The Climate System. *EPJ Web of Conferences* **2015**, *98*, 02001. https://doi.org/10.1051/epjconf/20159802001.

(6) Arrhenius, S. On the Influence of Carbonic Acid in the Air upon the Temperature of the Ground. *The London, Edinburgh, and Dublin Philosophical Magazine and Journal of Science* **1896**, No. Fifth Series.

(7) Ritchie, H.; Roser, M. Energy. *Our World in Data* **2020**.

(8) Roser, M.; Ortiz-Ospina, E.; Ritchie, H. Life Expectancy. *Our World in Data* **2013**.

(9) Riley, J. C. Estimates of Regional and Global Life Expectancy, 1800–2001. *Population and Development Review* **2005**, *31* (3), 537–543. https://doi.org/10.1111/j.1728-4457.2005.00083.x.

(10) Roser, M.; Ortiz-Ospina, E. Global Extreme Poverty. *Our World in Data* **2013**.

(11) Ritchie, H.; Roser, M. CO_2 and Greenhouse Gas Emissions. *Our World in Data* **2020**.

(12) Friedlingstein, P.; O'Sullivan, M.; Jones, M. W.; Andrew, R. M.; Hauck, J.; Olsen, A.; Peters, G. P.; Peters, W.; Pongratz, J.; Sitch, S.; Le Quéré, C.; Canadell, J. G.; Ciais, P.; Jackson, R. B.; Alin, S.; Aragão, L. E. O. C.; Arneth, A.; Arora, V.; Bates, N. R.; Becker, M.; Benoit-Cattin, A.; Bittig, H. C.; Bopp, L.; Bultan, S.; Chandra, N.; Chevallier, F.; Chini, L. P.; Evans, W.; Florentie, L.; Forster, P. M.; Gasser, T.; Gehlen, M.; Gilfillan, D.; Gkritzalis, T.; Gregor, L.; Gruber, N.; Harris, I.; Hartung, K.; Haverd, V.; Houghton, R. A.; Ilyina, T.; Jain, A. K.; Joetzjer, E.; Kadono, K.; Kato, E.; Kitidis, V.; Korsbakken, J. I.; Landschützer, P.; Lefèvre, N.; Lenton, A.; Lienert, S.; Liu, Z.; Lombardozzi, D.; Marland, G.; Metzl, N.; Munro, D. R.; Nabel, J. E. M. S.; Nakaoka, S.-I.; Niwa, Y.; O'Brien, K.; Ono, T.; Palmer, P. I.; Pierrot, D.; Poulter, B.; Resplandy, L.; Robertson, E.; Rödenbeck, C.; Schwinger, J.; Séférian, R.; Skjelvan, I.; Smith, A. J. P.; Sutton, A. J.; Tanhua, T.; Tans, P. P.; Tian, H.; Tilbrook, B.; van der Werf, G.; Vuichard, N.; Walker, A. P.; Wanninkhof, R.; Watson, A. J.; Willis, D.; Wiltshire, A. J.; Yuan, W.; Yue, X.; Zaehle, S. Global Carbon Budget 2020. *Earth System Science Data* **2020**, *12* (4), 3269–3340. https://doi.org/10.5194/essd-12-3269-2020.

(13) Bereiter, B.; Eggleston, S.; Schmitt, J.; Nehrbass-Ahles, C.; Stocker, T. F.; Fischer, H.; Kipfstuhl, S.; Chappellaz, J. Revision of the EPICA Dome C CO2 Record from 800 to 600 Kyr before Present. *Geophysical Research Letters* **2015**, *42* (2), 542–549. https://doi.org/10.1002/2014GL061957.

(14) Capdevila-Cortada, M. Electrifying the Haber–Bosch. *Nat Catal* **2019**, *2* (12), 1055–1055. https://doi.org/10.1038/s41929-019-0414-4.

(15) Hoegh-Guldberg, O.; Mumby, P. J.; Hooten, A. J.; Steneck, R. S.; Greenfield, P.; Gomez, E.; Harvell, C. D.; Sale, P. F.; Edwards, A. J.; Caldeira, K.; Knowlton, N.; Eakin, C. M.; Iglesias-Prieto, R.; Muthiga, N.; Bradbury, R. H.; Dubi, A.; Hatziolos, M. E. Coral Reefs Under Rapid Climate Change and Ocean Acidification. *Science* **2007**, *318* (5857), 1737–1742. https://doi.org/10.1126/science.1152509.

(16) Nerem, R. S.; Beckley, B. D.; Fasullo, J. T.; Hamlington, B. D.; Masters, D.; Mitchum, G. T. Climate-Change–Driven Accelerated Sea-Level Rise Detected in the Altimeter Era. *PNAS* **2018**, *115* (9), 2022–2025. https://doi.org/10.1073/pnas.1717312115.

(17) van Oldenborgh, G. J.; Philip, S.; Kew, S.; van Weele, M.; Uhe, P.; Otto, F.; Singh, R.; Pai, I.; Cullen, H.; AchutaRao, K. Extreme Heat in India and Anthropogenic Climate Change. *Natural Hazards and Earth System Sciences* **2018**, *18* (1), 365–381. https://doi.org/10.5194/nhess-18-365-2018.

(18) Walther, G.-R.; Post, E.; Convey, P.; Menzel, A.; Parmesan, C.; Beebee, T. J. C.; Fromentin, J.-M.; Hoegh-Guldberg, O.; Bairlein, F. Ecological Responses to Recent Climate Change. *Nature* **2002**, *416* (6879), 389–395. https://doi.org/10.1038/416389a.

(19) IPCC. *Climate Change 2021: The Physical Science Basis. Contribution of Working Group I to the Sixth Assessment Report of the Intergovernmental Panel on Climate Change*; Cambridge University Press, 2021.

(20) U.S. energy facts explained - consumption and production - U.S. Energy Information Administration (EIA) https://www.eia.gov/energyexplained/us-energy-facts/ (accessed 2021 -09 -14).

(21) LeValley, T. L.; Richard, A. R.; Fan, M. The Progress in Water Gas Shift and Steam Reforming Hydrogen Production Technologies – A Review. *International Journal of Hydrogen Energy* **2014**, *39* (30), 16983–17000. https://doi.org/10.1016/j.ijhydene.2014.08.041.

(22) Hemmerling, J. R.; Mathur, A.; Linic, S. Design Principles for Efficient and Stable Water Splitting Photoelectrocatalysts. *Acc. Chem. Res.* **2021**, *54* (8), 1992–2002. https://doi.org/10.1021/acs.accounts.1c00072.

(23) Miotti, M.; Supran, G. J.; Kim, E. J.; Trancik, J. E. Personal Vehicles Evaluated against Climate Change Mitigation Targets. *Environ. Sci. Technol.* **2016**, *50* (20), 10795–10804. https://doi.org/10.1021/acs.est.6b00177.

(24) A. Hansen, H.; Rossmeisl, J.; K. Nørskov, J. Surface Pourbaix Diagrams and Oxygen Reduction Activity of Pt , Ag and Ni(111) Surfaces Studied by DFT. *Physical Chemistry Chemical Physics* **2008**, *10* (25), 3722–3730. https://doi.org/10.1039/B803956A.

(25) Fuel Cells | Department of Energy https://energy.gov/eere/fuelcells/fuel-cells (accessed 2018 -06 -20).

(26) James, B.; et. al. Fuel Cell System Cost - 2017. Department of Energy 2017.

(27) Luo, M.; Sun, Y.; Zhang, X.; Qin, Y.; Li, M.; Li, Y.; Li, C.; Yang, Y.; Wang, L.; Gao, P.; Lu, G.; Guo, S. Stable High-Index Faceted Pt Skin on Zigzag-Like PtFe Nanowires Enhances Oxygen Reduction Catalysis. *Advanced Materials* **2018**. https://doi.org/10.1002/adma.201705515.

(28) Cleve, T. V.; Moniri, S.; Belok, G.; More, K. L.; Linic, S. Nanoscale Engineering of Efficient Oxygen Reduction Electrocatalysts by Tailoring the Local Chemical Environment of Pt Surface Sites. *ACS Catal.* **2017**, *7* (1), 17–24. https://doi.org/10.1021/acscatal.6b01565.

(29) Xin, H.; Holewinski, A.; Linic, S. Predictive Structure–Reactivity Models for Rapid Screening of Pt-Based Multimetallic Electrocatalysts for the Oxygen Reduction Reaction. *ACS Catal.* **2012**, *2* (1), 12–16. https://doi.org/10.1021/cs200462f.

(30) Huang, X.; Zhao, Z.; Cao, L.; Chen, Y.; Zhu, E.; Lin, Z.; Li, M.; Yan, A.; Zettl, A.; Wang, Y. M.; Duan, X.; Mueller, T.; Huang, Y. High-Performance Transition Metal–Doped Pt3Ni Octahedra for Oxygen Reduction Reaction. *Science* **2015**, *348* (6240), 1230–1234. https://doi.org/10.1126/science.aaa8765.

(31) Zhang, G.-R.; Wöllner, S. Hollowed Structured PtNi Bifunctional Electrocatalyst with Record Low Total Overpotential for Oxygen Reduction and Oxygen Evolution Reactions. *Applied Catalysis B: Environmental* **2018**, *222* (Supplement C), 26–34. https://doi.org/10.1016/j.apcatb.2017.09.066.

(32) Wang, C.; Zhang, L.; Yang, H.; Pan, J.; Liu, J.; Dotse, C.; Luan, Y.; Gao, R.; Lin, C.; Zhang, J.; Kilcrease, J. P.; Wen, X.; Zou, S.; Fang, J. High-Indexed Pt3Ni Alloy Tetrahexahedral Nanoframes Evolved through Preferential CO Etching. *Nano Lett.* **2017**, *17* (4), 2204–2210. https://doi.org/10.1021/acs.nanolett.6b04731.

(33) Chen, C.; Kang, Y.; Huo, Z.; Zhu, Z.; Huang, W.; Xin, H. L.; Snyder, J. D.; Li, D.; Herron, J. A.; Mavrikakis, M.; Chi, M.; More, K. L.; Li, Y.; Markovic, N. M.; Somorjai, G. A.; Yang, P.; Stamenkovic, V. R. Highly Crystalline Multimetallic Nanoframes with Three-Dimensional Electrocatalytic Surfaces. *Science* **2014**, *343* (6177), 1339–1343. https://doi.org/10.1126/science.1249061.

(34) Jensen, K. D.; Tymoczko, J.; Rossmeisl, J.; Bandarenka, A.; Chorkendorff, I.; Escudero-Escribano, M.; Stephens, I. E. L. Elucidation of the Oxygen Reduction Volcano in Alkaline Media Using a Copper-Platinum(111) Alloy. *Angew. Chem. Int. Ed.* n/a-n/a. https://doi.org/10.1002/anie.201711858.

(35) Wang, D.; Xin, H. L.; Hovden, R.; Wang, H.; Yu, Y.; Muller, D. A.; DiSalvo, F. J.; Abruña, H. D. Structurally Ordered Intermetallic Platinum–Cobalt Core–Shell Nanoparticles with Enhanced Activity and Stability as Oxygen Reduction Electrocatalysts. *Nature Materials* **2013**, *12* (1), 81–87. https://doi.org/10.1038/nmat3458.

(36) Holewinski, A.; Idrobo, J.-C.; Linic, S. High-Performance Ag–Co Alloy Catalysts for Electrochemical Oxygen Reduction. *Nat Chem* **2014**, *6* (9), 828–834. https://doi.org/10.1038/nchem.2032.

(37) Luo, J.; Tang, H.; Tian, X.; Liao, S.; Ren, J.; Zhao, W.; Qiao, X. Glucose-Derived Carbon Supported Well-Dispersed CrN as Competitive Oxygen Reduction Catalysts in Acidic Medium. *Electrochimica Acta* **2019**, *314*, 202–211. https://doi.org/10.1016/j.electacta.2019.05.078.

(38) Li, J.-C.; Xiao, F.; Zhong, H.; Li, T.; Xu, M.; Ma, L.; Cheng, M.; Liu, D.; Feng, S.; Shi, Q.; Cheng, H.-M.; Liu, C.; Du, D.; Beckman, S. P.; Pan, X.; Lin, Y.; Shao, M. Secondary-Atom-Assisted Synthesis of Single Iron Atoms Anchored on N-Doped Carbon Nanowires for Oxygen Reduction Reaction. *ACS Catal.* **2019**, 5929–5934. https://doi.org/10.1021/acscatal.9b00869.

(39) Wang, H.-F.; Chen, L.; Wang, M.; Liu, Z.; Xu, Q. Hollow Spherical Superstructure of Carbon Nanosheets for Bifunctional Oxygen Reduction and Evolution Electrocatalysis. *Nano Lett.* **2021**, *21* (8), 3640–3648. https://doi.org/10.1021/acs.nanolett.1c00757.

(40) Krivenko, A. G.; Manzhos, R. A.; Kochergin, V. K.; Kotkin, A. S.; Pleskov, Yu. V.; Krotova, M. D.; Ekimov, E. A. Effect of Plasma-Assisted Electrochemical Treatment of the Boron-Doped Synthetic Diamond Compact Electrodes on the Oxygen Electroreduction

Kinetics. *Electrochimica Acta* **2021**, *390*, 138843.
https://doi.org/10.1016/j.electacta.2021.138843.

Chapter 2 Experimental and Computational Methods

2.1 Summary

This chapter goes over the various methods used to complete the work in this dissertation. A brief discussion on background and purpose of each method is also provided. The sections are intended to be detailed enough that a future researcher could apply these methods to their own work and yield useful results.

2.2 Electrochemical Methods

2.2.1 3-Electrode Cell

To study the electrochemical processes of one half-reaction, it is useful to measure the potential/current on just one electrode while disregarding the full cell system. This can be accomplished by constructing a 3-electrode cell as seen in Figure 2.1.

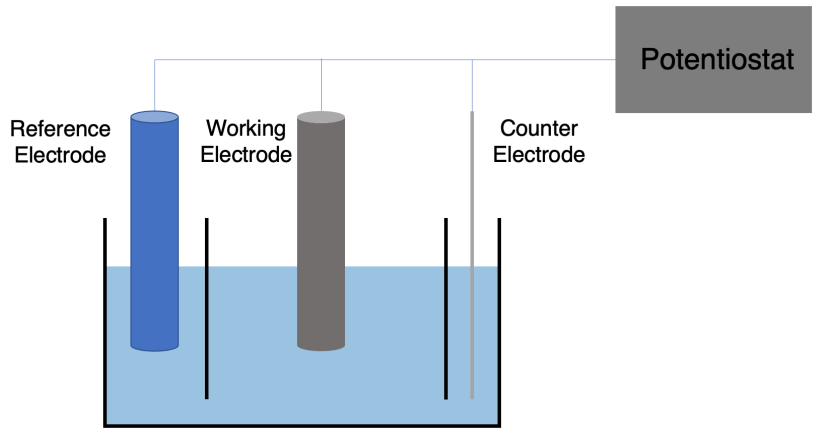


Figure 2.1 Schematic of 3-electrode cell

In a 3-electrode cell, the main components are:

- The working electrode, which contains the material of interest conducting the reaction of interest.
- The reference electrode, which contains a stable and known redox potential to provide a reference for the working electrode's potential.
- The counter electrode, which balances the charge in the system.
- The potentiostat, which controls and measures the potential/current at the working electrode and connects the three electrodes.

The potentiostat has several controls to ensure that no current runs through the reference electrode. This is done to prevent the known potential from drifting due to concentration changes of reactant and products. The potentiostat also controls the potential at the counter electrode to mirror the current produced at the working electrode. When studying reduction reactions at the working electrode, the counter electrode will be doing an oxidation, often oxygen evolution in aqueous solutions.

Common reference electrodes include:

- Ag/AgCl in KCl. Silver metal in equilibrium with silver chloride contained in a concentrated potassium chloride electrolyte. This reference is best for neutral to low pHs and for systems where possible Cl contamination is not a large concern. A Luggin capillary can be used to prevent this.
- Hg/HgO in KOH. Mercury in equilibrium with mercury oxide contained in a concentrated potassium hydroxide solution. This reference is best for high pH solutions and is often found in a plastic housing instead of glass to prevent etching from the base.

- $Hg/HgSO_4$ in K_2SO_4. Mercury in equilibrium with mercury sulfate contained in a concentrated potassium sulfate solution. This reference is best used for sulfuric acid electrolytes.

For counter electrodes, either Pt wires or graphene is generally used. There is debate between which counter electrode is the best to use in laboratory research. Pt has been shown to dissolve then redeposit on the working electrode giving artificially high catalytic rates[1]. However, graphene has been shown to form carbon monoxide (due to the high potentials experienced when balancing a reduction at the working electrode) which can poison Pt catalyst sites at the working electrode giving artificially lower catalytic rates[2]. The counter electrode material should always be reported and kept consistent for all runs. For this dissertation, all data was collected using a Pt wire counter electrode.

2.2.2 Rotating Disk Electrode

When studying electrochemical reactions at a working electrode, the inherent kinetics of the material can be convoluted by the mass transport of reactants to the electrode surface. As an example, take the oxygen water redox couple:

$$O_2 + 4H^+ + 4e^- \leftrightarrow 2H_2O$$

At electrode potentials below 1.23 V the reaction begins to move toward the right with oxygen being reduced to form water. The overall speed of this reaction on a non-porous electrocatalyst is governed by two effects:

- The chemical kinetics of the reaction, i.e. the speed of which an oxygen molecule at the catalyst surface undergoes four subsequent proton coupled electron transfers to two water molecules.
- The speed of an oxygen molecule diffusing to the catalyst surface from the bulk electrolyte.

At some point the kinetics of the reaction are so fast that oxygen cannot reach the surface of the catalyst fast enough, and a "mass limiting" current is observed. At this mass limiting current, no matter how high energy the electrons are (low potential, far from equilibrium) the observed current does not change.

The relationship between the observed current, the kinetic current and the mass limiting current is described by the Koutecky-Levich equation:

$$i = \left(\frac{1}{i_k} + \frac{1}{i_L}\right)^{-1}$$

Where i is the total current, i_k is the kinetic current and i_L is the mass limiting current. An example of a typical S-shaped curve that is observed when measuring the rates of ORR on a Pt electrocatalyst is shown in Figure 2.2.

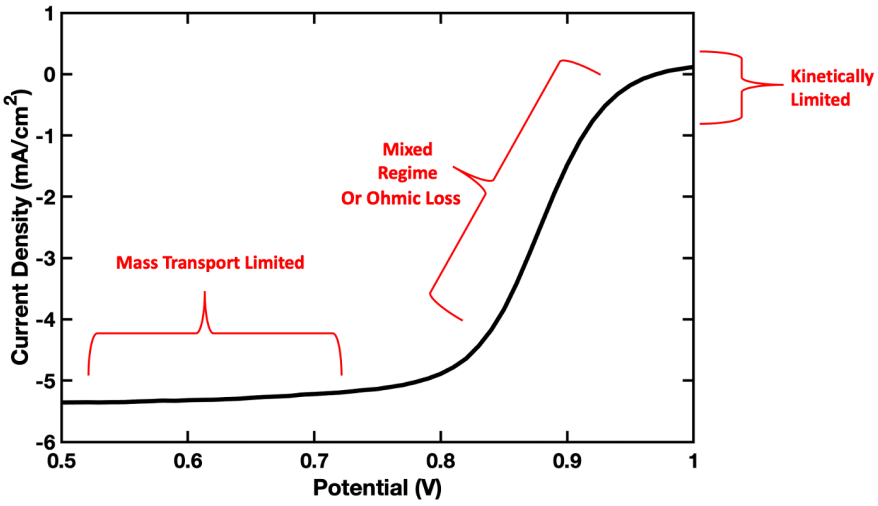


Figure 2.2 Typical IV curve for the ORR on a Pt rotating disk electrode in oxygen saturated electrolyte

This curve has three regions that dominate the shape. At high potentials close to equilibrium, the current is dominated by the kinetics of the catalyst and shows an exponential increase with respect to potential. At very low potentials far from equilibrium, the current is dominated by mass transport limitations and is insensitive to the applied potential. In between the kinetically limited and mass limited region there is a "mixed" region whose shape is dominated by both kinetics and transport,

but also the ohmic losses from series resistance throughout the cell (how to calculate this will be discussed in the next section).

After collecting the IV curve shown in Figure 2.2 the potential independent mass limiting current can be used in conjunction with the total current to calculate the potential dependent kinetic current. This should not be done, however, before correcting the IV curve for the capacitive current (see below) and the series (solution) resistance.

2.2.3 Measuring Solution Resistance

The current that moves through the electrochemical cell encounters a resistance that follows Ohm's law:

$$V = IR$$

Where V is the voltage, I is the current and R is the resistance. The solution resistance in the electrochemical cell has the effect of a "voltage loss" where the voltage you apply does not equal the voltage at the working electrode. The voltage loss follows this relationship:

$$V_{actual} = V_{applied} - I * R_{solution}$$

Where V_{actual} is the voltage at the working electrode, $V_{applied}$ is the voltage applied by the potentiostat, I is the current and $R_{solution}$ is the solution resistance. From this relationship, it is easy to see how important the solution resistance is. If the current and solution resistance is large, the potential at the working electrode will be very different from the potential that is applied, giving misleading data. Some potentiostats have features to automatically correct for this voltage loss, but such techniques should be tested to ensure accurate data.

To calculate the solution resistance, impedance spectroscopy can be used. Impedance spectroscopy is a technique used to apply a small voltage signal around the open circuit potential of the working electrode and to analyze the resulting current. In lieu of a more comprehensive explanation, I refer

the reader to the following reference from Gamry Instruments (the maker of the potentiostat used throughout this dissertation) that provides the technical background for this technique[3]. For practical measurements, I use the hybrid electrochemical impedance spectroscopy method in the Gamry Framework software to measure the impedance between 100 kHz and 1 Hz. A typical response in shown in Figure 2.3.

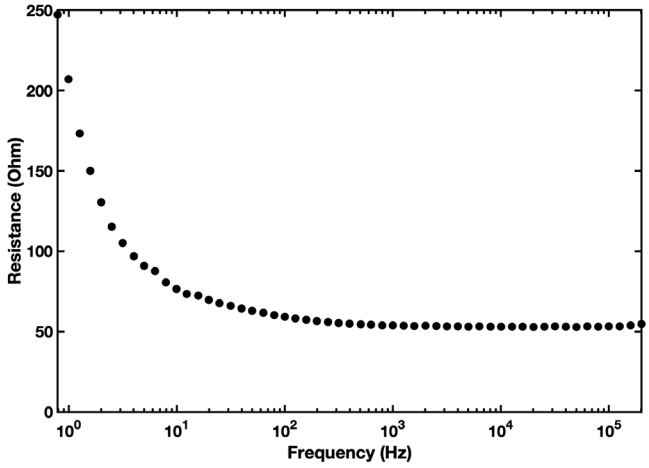


Figure 2.3 Resistance vs. frequency during a hybrid impedance spectroscopy measurement of a Pt electrode in 0.1 M NaOH

The solution resistance is taken at 1 kHz where the flat high frequency region begins. In this region, the solution resistance dominates while at lower frequencies, the impedance from charge transfer and the double layer dominate. For a Hg/HgO reference electrode in 0.1 M NaOH the solution resistance was typically between 40-60 Ω. For Ag/AgCl reference electrode in 0.1 M $HClO_4$ the resistance is typically between 20-30 Ω. All potentials should be corrected for solution resistance before any data analysis is performed.

2.2.4 Capacitive Current Measurements

Besides the solution resistance, the capacitive currents must also be accounted for before data analysis is performed. The capacitive currents arise from the charging and discharging of the electrochemical double layer (EDL) that forms at the interface of the solid electrode and liquid

electrolyte. The capacitive current is "non-faradaic" i.e. no charge transfer between species occurs. When the potential at the working electrode is changing (like during linear and cyclic voltammetry), a constant capacitive current is measured based on the scan rate of the potential sweep following this relationship:

$$I_{cap} = C * SR$$

Where I_{cap} is the capacitive current with units of Amperes (A), C is the capacitance with units of Farads (F) and SR is the scan rate with units of V/s. To measure the capacitive current, a cyclic voltammogram must be performed in a potential region where no Faradic processes are occurring. For Pt electrodes, this region is found between 0.4-0.7 V in an inert (Ar, N_2, He) saturated electrolyte. This region can be seen in the voltammogram of a Pt electrode shown in Figure 2.4.

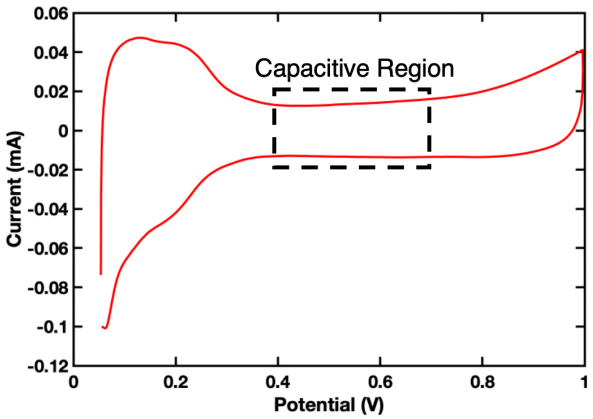


Figure 2.4 Cyclic voltammogram of Pt nanoparticles on carbon black in Ar saturated 0.1 M NaOH

The region positive of the capacitive region contains several faradic processes including carbon oxidation, Pt-OH formation, and Pt-O formation. The region negative to the capacitive region is dominated by H_{upd} adsorption and desorption. This region, and its use for calculating surface area is further discussed in Chapter 3. The overall capacitive current can be calculated by averaging the values of the anodic and cathodic currents through the capacitive region and then averaging their

absolute values together. This can then be converted to a raw capacitance using the relationship above and the scan rate used to collect the voltammogram.

2.2.5 Rotating Ring Disk Electrode

One powerful technique for analyzing the mechanism of the ORR is using a rotating ring disk electrode (RRDE) with a bipotentiostat setup. This technique uses two potentiostats (bipotentiostat) connected to the rotating disk and to a concentric ring around the disk separated by a spacer (Figure 2.5).

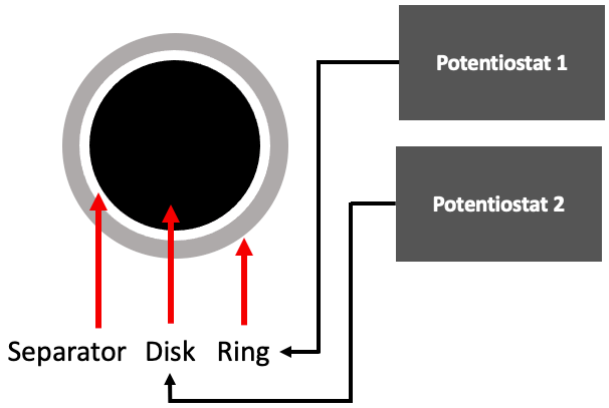


Figure 2.5 Schematic of a rotating disk ring electrode

The electrocatalyst of interest is deposited on the disk electrode while the ring (which is often made of gold or platinum) potential is controlled independently of the disk. For the ORR this technique can be used to analyze the products leaving the disk during operation. For fuel cells, the 4-electron ORR to product water is the desired reaction, but there is another competing route where 2 electrons are transferred to produce hydrogen peroxide that is undesirable in fuel cell applications as peroxide can damage other components in the cell. This unwanted side reaction with equilibrium potential of 0.7 V is:

$O_2 + 2H^+ + 2e^- \rightarrow H_2O_2$

The RRDE method can determine the selectivity toward the 4-electron mechanism by setting the ring to an oxidizing potential to convert some fraction of peroxide that is formed back into oxygen. These processes are shown in Figure 2.6 where an oxygen molecule diffuses to the disk surface.

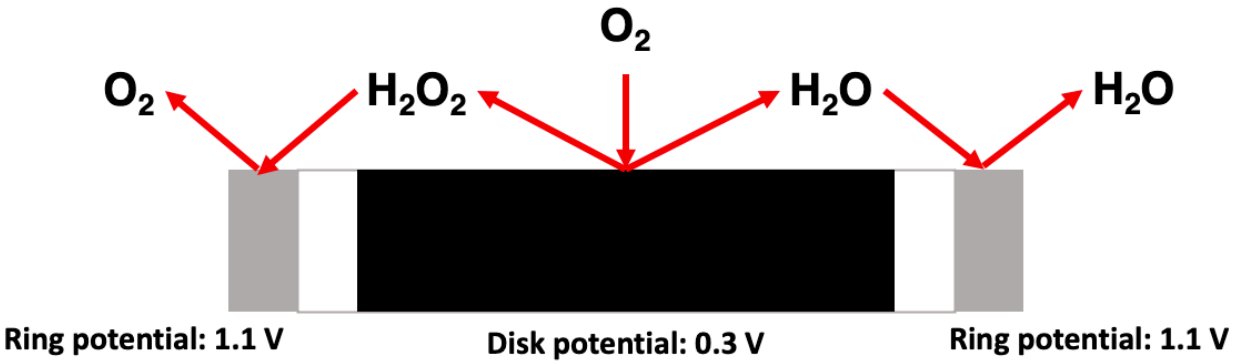


Figure 2.6 Example of RRDE in operation during ORR

Upon reaching the surface, the ORR will occur either converting the oxygen into water or hydrogen peroxide. If water is formed, it will travel to the ring (which is set at 1.1 V) and not be oxidized as water splitting does not occur below 1.23 V. If hydrogen peroxide is formed at the disk however, it will migrate to the ring and be oxidized back into molecular oxygen and a current will be measured. The currents measured at the disk and ring can be used to calculate the average number of electrons transferred (a proxy for selectivity) using this equation:

$$n = \frac{4 * i_{disk}}{i_{disk} + \frac{i_{ring}}{\varepsilon}}$$

Where n is the number of electrons transferred, i_{disk} is the measured disk current, i_{ring} is the measured ring current and ε is the ring collection efficiency.

The value of the collection efficiency, which describes what fraction of reactive product from the disk reaches and reacts with the ring, is critically important and should be calibrated as often as possible. To calibrate the collection efficiency, the single electron redox couple of $K_3Fe(CN_6)$(III) and $K_3Fe(CN_6)$(II) can be used. For this experiment, 10 mM of $K_3Fe(CN_6)$(III) is dispersed in 1

M KNO_3 as the electrolyte. The three-electrode setup is constructed with glassy carbon as the working electrode, a Ag/AgCl as the reference and Pt wire as counter. Ideally, the working electrode used in calibration should match what will be used in the ORR experiments. This is because the thin-film application of the electrocatalyst will affect the flow pattern around the working electrode with increased turbulence from the heterogenous film resulting in less fluid packets from the disk interacting with the ring. Sweeping the potential from 0.75 to -0.25 V vs. the reference results in a voltammogram seen in Figure 2.7 for RRDE rotation speed of 400, 900, 1600 and 2500 RPM.

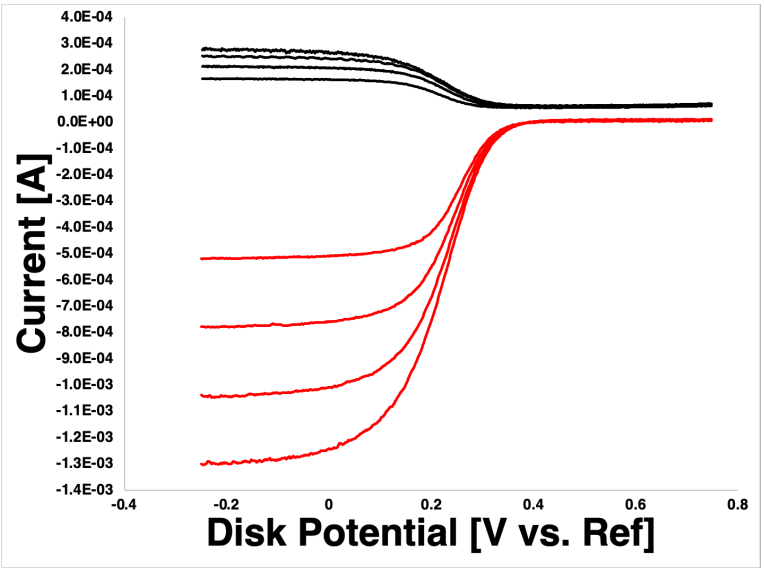


Figure 2.7 Variations in limiting current with respect to rotation rate. In black is the current measured at the ring and in red is the current measured at the disk. The ring is held at a potential of 1.1 V while the disk varies potential from 0.75 to -0.25 V. The reduction begins around 0.3 V where it is then limited at lower potentials.

Unsurprisingly, as the rotation speed increases, the mass limiting current for the reduction of $K_3Fe(CN_6)$(III) also increases. The collection efficiency is simply the ratio of the mass limiting current for the ring and the disk:

$$\varepsilon = \frac{i_{ring}}{i_{disk}}$$

For the experiment above, the collection efficiencies are shown in Table 2.1.

Table 2.1 Mass limiting currents at different RRDE rotation speeds and the calculated collection efficiencies.

	Current [μA]	RPM	Collection Efficiency
Disk	-517.9	400	**0.32**
Ring	165.8	400	
Disk	-776.6	900	**0.27**
Ring	210.7	900	
Disk	-1042	1600	**0.24**
Ring	249.8	1600	
Disk	-1300	2500	**0.21**
Ring	274.8	2500	

Rotation speed is an important parameter during ORR experiments as the collection efficiency appears to decrease with increasing RRDE rotation speeds.

2.3 Syntheses

In the following subsections, syntheses used in this dissertation are described.

2.3.1 60 nm Ag Nanoparticles

60 nm Ag nanospheres were synthesized using a polyol synthesis. 8 mL of ethylene glycol (EG, JT Baker), which serves as a reducing agent, is heated up to 160ºC for 1 hour in a glass vial contained in an oil bath. 500 mg of polyvinylpyrrolidone (PVP, Aldrich. MW: ~55,000) in 8 mL of EG is then added to the heated glass vial as a stabilizing agent for the nanoparticle seeds. After 10 minutes, 50 mg of the silver precursor, silver nitrate (Acros, 99.5%) in 2 mL of EG, is added to the heated vial. The EG reduces the silver nitrate into colloidal silver nanoparticles causing the solution to change from a clear color to a yellowish then yellowish-brown to greenish-yellow color over 30 minutes. The glass vial is then taken out of the oil bath and placed in an ice bath to quench the reaction. This solution is then washed by centrifugation 2-3 times at 8000 rpm for 15 minutes, initially in acetone (Fisher, 99.6%) then twice in E-pure water (18.2 MΩ cm, Millipore) to remove

the excess precursor, reducing agent and stabilizing agent. 300 μL of 36 mM hydrochloric acid (Fisher, 36.5-38%) in E-pure water is added after the first wash to prevent aggregation of the ~60 nm Ag spheres.

2.3.2 60 nm Ag-Pt Core-Shell Nanoparticles

This synthesis uses the 60 nm Ag nanoparticles as a seed on which to grow a Pt shell. To form the Pt shell, the seed solution is diluted to 16 mL in E-pure water and added to a Teflon reactor vessel with a stir bar. 300 mg of PVP is then added to the spheres to stabilize the nanoparticles. 300 μL of 1.25 M sodium hydroxide (NaOH pellets, Merck) in E-pure water is added to the vessel to raise the solution pH as the final Ag-Pt particles are sensitive to pH and will hollow out if kept in a neutral or acidic environment. 250 mg of glucose (Sigma, 99.5%) is added as a mild reducing agent before a solution of 30 mg of potassium tetracholoroplatinate (Acros, 46-47% Pt) in 15 mL of E-pure water and 150 μL of 1.25 M NaOH is added to the vessel starting the Pt deposition. The reaction is allowed to proceed for 30 hours under stirring as the green solution grows slightly darker over time. After the reaction is completed, the solution is washed at least twice in basic E-pure water at 11000 rpm for 20 minutes. This procedure yields between 30-40 mg of Ag-Pt nanospheres.

2.4 In-situ Raman Electrochemical Flow Cell

In Chapter 5, in-operando Raman measurements of the oxygen reduction reaction at the electrified Pt surface are conducted to reveal mechanistic insights. This method utilizes a flow cell that allows the Raman laser to interact with the Pt nanoparticles while also controlling the potential of the nanoparticles. This section will go over the flow cell setup but also describe Raman spectroscopy as a powerful tool for mechanistic analysis.

2.4.1 Raman Spectroscopy

Raman spectroscopy was first developed by Indian physicist Sir C.V. Raman in 1928. He observed that there was a shift in the vibrational frequency of some scattered light when the incident light interacted with a transparent material. This shift in reflected light is called Raman scattering and can be detected using a Raman spectrometer. Raman scattering occurs when incident light is absorbed by a molecule in the ground state and is excited to an extremely short-lived virtual energy state and subsequently relaxes back to a higher vibrational energy state. The photon emitted from relaxing back to the higher vibrational state is called a Stokes Raman scattered photon and can be detected by a Raman spectrometer to determine the frequency of the molecule's vibrational modes. The opposite transition (from higher vibrational state to lower vibrational state via the virtual state) is called anti-Stokes Raman scattering. Both Stokes and anti-Stokes Raman scattering are very rare events and most of the time the molecule relaxes directly back to its initial state after absorbing an incident photon. This type of scattering is called Rayleigh scattering and it is ~10^8 times more likely to occur than Raman scattering[4].

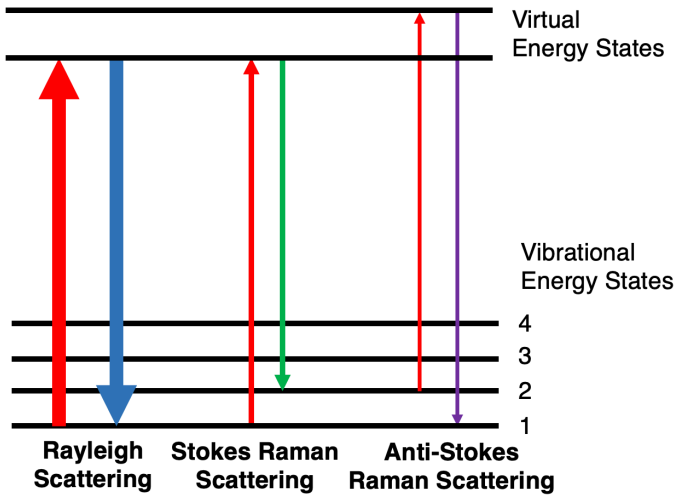


Figure 2.8 Diagram of Rayleigh, Stokes Raman, and anti-Stokes Raman scattering

Which molecular vibrations can produce Raman scattering depend on the polarizability of the molecule's bonds. The polarizability can be understood to mean the degree of which the electron cloud around the molecule or bond can change when interacting with an external electric field. For an example, consider the four stretches of the carbon dioxide molecule discussed in Chapter 1. The symmetric stretch, which is IR inactive, is found to be Raman active due to the increased polarizability of the CO bonds as they are stretched. For the asymmetric stretch, the increase of polarizability in one bond is offset by the decrease of polarizability of the other and is therefore Raman inactive. Similarly, for the O_2 molecule (of which there is only one vibrational mode), the symmetric stretch is Raman active but not IR active making Raman spectroscopy attractive for studying the oxygen reduction reaction.

One issue with Raman spectroscopy is how rare Stokes Raman scattering events are, making Raman spectroscopy difficult/impossible to use for detecting individual molecules on a catalyst surface. It was observed in 1977, however, that the Raman intensity was greatly enhanced when the molecule of interest was near a nanostructured material[5,6]. These works gave rise to the field of surface enhanced Raman spectroscopy or SERS which has been shown to enhance Raman intensities up to 10^{14} times.

SERS is enabled by local surface plasmon resonance (LSPR) which is a phenomenon that occurs in certain metal nanostructures (Ag, Au, and Cu nanoparticles for example) smaller than the wavelength of incident light. Incident photons incite an oscillating dipole in the electron cloud of the nanoparticles producing LSPR as shown in Figure 2.9.

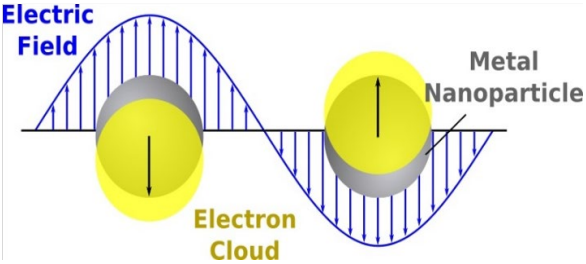


Figure 2.9 Diagram of LSPR on a metal nanoparticle

LSPR produces enhanced electric fields at the surface of the nanoparticles which has been shown to greatly increase the probability of Raman scattering from adsorbates on the nanoparticle surface[7]. The SERS enhancement factor, G, has been shown to approximately follow this relation:

$$G = |E|^4$$

Where |E| is the electric field intensity. This relationship demonstrates the huge effect electric field intensity has on Raman enhancement. Previous research in the Linic group has shown that this strong electric field can transfer energy to non-plasmonic metals coating a plasmonic core enabling SERS on metals such as Pt[8]. These enhancements are further increased by "hotspots" between nanoparticles in close proximity (<1 nm) of each other, allowing aggregates of plasmonic nanoparticles to be an excellent SERS substrate. In Chapter 5, the Raman measurements were conducted on a Horiba, LabRAM HR using a 50 mW, 532 nm diode-pumped solid-state laser with a 10x objective (Olympus, MPlan N). A 15 s acquisition time was used and at least 3 spectra were averaged together for each potential to minimize heterogeneity in the data from differing nanoparticle aggregates.

2.4.2 In-situ Flow Cell

To simultaneously collect Raman spectra and electrocatalyst current/potential, an in-situ flow cell was used. The flow cell was based on a commercially available spectroelectrochemical cell (Redox.me, MM Raman ECFC) with a few modifications[9]. The working electrodes were

fabricated starting with a 25x25x1 mm piece of glass that was coated with 10 nm of titanium as an adhesive layer and 100 nm of silver using e-beam evaporation at the Lurie Nanofabrication Facility of the University of Michigan. Silver was chosen as it is stable in the basic electrolyte used but does not produce hydrogen peroxide like gold at the high pH condition. The counter electrode was a Pt wire that encircles the working electrode to enable consistent flow fields from working to counter electrode. The flow cell was attached to two electrolyte reservoirs on inlet and outlet sides with a peristaltic pump circulating electrolyte from one reservoir to the other at 0.5 ml/min. A Hg/HgO reference electrode was placed in one of the reservoirs and all three electrodes were connected to a potentiostat (Gamry). For experiments, the reference electrode was calibrated against a reversible hydrogen electrode in the same 0.1 M NaOH to ensure accurate voltages. The full setup is visualized in Figure 2.10. There peristaltic pump had the effect of keeping a constant pressure head between the two reservoirs allowing constant flow through the cell. This design was chosen to prevent air bubbles from entering the cell due to the peristaltic action if directly connected. Solution resistance was measured to be 80 Ω using electrochemical impedance spectroscopy. O_2 or He (both Ultra High Purity Grade) was bubbled into the two reservoirs depending on operation.

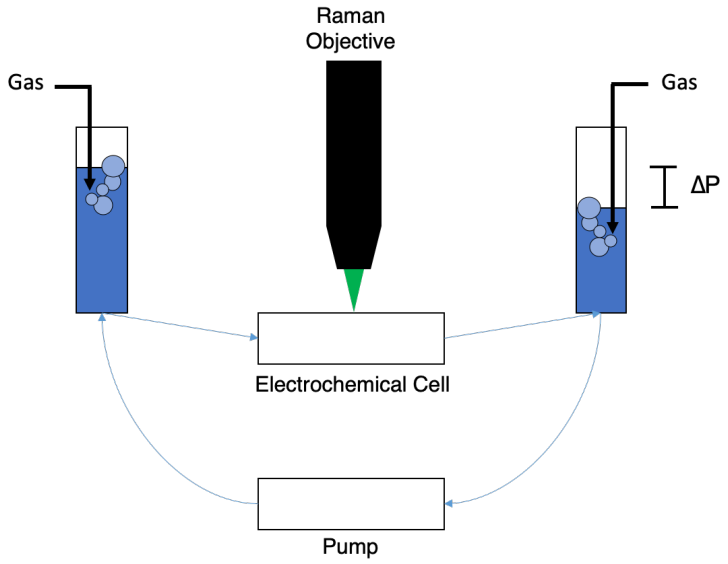


Figure 2.10 Schematic of the in-situ flow cell during normal operation. He or O_2 is bubbled into both reservoirs simultaneously. The reference electrode is contained in one of the electrolyte reservoirs and the counter electrode is contained within the spectroelectrochemical cell.

For the operando study in Chapter 5, a ~1mg/ml mixture of the Ag-Pt nanoparticles in basic H_2O was washed 5 times in basic water at 11000 rpm for 20 minutes to remove PVP from the nanoparticle surface. This solution was then deposited dropwise on the silver film working electrode. The glass was then placed in a vacuum oven (100 mbar, 50ºC) for 30 minutes to allow the solvent to evaporate. The nanoparticles were then washed to remove loose particles and contaminants with 0.1 M NaOH (Milipore Suprapur, 30%) in E-pure (18.2 MΩ cm, Millipore) water. The 0.1 M NaOH solution was mixed with Chelex 200 resin (Biorad) overnight to remove trace transition metal impurities. After mixing, the resin was removed with vacuum filtration 2 times. Before Raman spectra were collected, the Ag-Pt nanoparticles are electrochemically cleaned (cycling between 0.05-1.1 V vs. RHE 10 times) to further remove any organic ligands from the Pt surface.

2.4.3 Statistical Analysis

It is important to quantify the effects on changing potential with changing peak size to aid in data analysis. The statistical analysis of the intensity changes with potential was quantified by the following procedure: A minimum of 3 spectra were collected for each potential. For each data point, a gaussian line form was fit to the data using MATLAB. In case of peaks at 1600 and 1664 cm^{-1} a two term gaussian was fit and then decoupled in order to deconvolute the two peaks (see Figure 2.11). These gaussians are then integrated to yield a total band intensity for each data point.

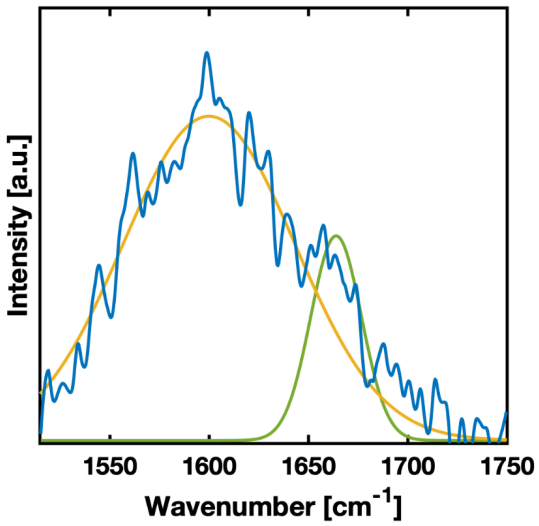


Figure 2.11 One Raman data point at 750 mV in He saturated electrolyte in blue. In yellow and green are two gaussian line forms centered around 1600 and 1664 cm^{-1} fitted to the blue data. This fitting has an R^2 = 0.92.

2.5 Ab-Initio Calculations

To complement experimental findings, computational chemistry techniques like ab-initio modeling have been extensively used in the field of catalysis. Ab-initio modeling, meaning "from the beginning" or "first principles", seeks to model the electronic structure of atoms and molecules by solving or approximating the Schrödinger equation:

$$\hat{H}\Psi = E\Psi$$

Where $\hat{H}$ is the Hamiltonian, E is energy and Ψ is the wavefunction. This simple representation of the Schrödinger equation belies the vast complexities of solving it for many-body problems. To

simplify and speed up these types of calculations, density functional theory (DFT) was developed in the 1960's and was increasingly used for quantum chemistry applications in the 1990's[10]. Kohn-Sham DFT (KS-DFT) in particular has been very successful in the field of quantum chemistry and is incorporated in many packages such as VASP[11–14] (Vienna ab-inito Simulation Package). In this section, I will provide practical tutorials using VASP to yield accurate and repeatable simulations while also describing the methods I used to calculate the vibrational modes in Chapter 5.

2.5.1 VASP basics

To run a job using VASP, there are 5 essential files that are needed. Each file has many options and the user should refer to the VASP wiki for more information on each file[15]:

- POSCAR: This is the geometry file for VASP. At the top of the file, the scaling parameter is set and the size of the box is formed from 3 vectors. Often, the scaling parameter is set to 1 or some lattice constant. Below this, the number of atoms is set, and the coordinate system (direct or cartesian) is also specified. Selective dynamics can be enabled to freeze atoms in the x, y or z direction. An example POSCAR is given in the next section.
- INCAR: This file sets the calculation parameters for VASP. There are many flags and options including EDIFF which sets the convergence energy criteria, IBRION which determines what type of calculation is performed (molecular dynamics, ion relaxation, vibrational modes, etc.), and NSW which determines how many steps to run, among many others.
- KPOINTS: This file sets the number of k-points used in the calculation. The most common method, and the method I use throughout the dissertation, is the Monkhorst-Pack method where k-points along the 3 lattice vectors are manually supplied. This method gives the greatest flexibility and reproducibility. It should be noted that after VASP version 5.2.12,

the KPOINTS file is no longer needed and can be controlled by the KSPACING tag in the INCAR.

- POTCAR: This file supplies the pseudopotentials for each atom specified in the POSCAR. It is a catenated list of each element's individual POTCAR and should be organized in order of how elements appear in the POSCAR.
- Submission script: VASP can be ran directly from the command line, but in most instances a submission script will be needed in order to send the job to a compute node for faster calculations. This file can interact with job schedulers (such as PBS, Slurm, etc.) and also enable parallelization across multiple nodes.

When VASP is finished running, it will produce several files that can be used for analysis. The CONTCAR file mimics the POSCAR and contains the final geometry of the calculation. The OUTCAR provides the final electronic structure information and can be parsed for total free energy, entropy and vibrational modes (if running a job with IBRION=5 or 6). Though VASP energies are mostly used for comparisons, i.e. relative differences, the best absolute energy to reference is the "energy(sigma→0)" found in the OUTCAR as it is the energy at 0 K and not an elevated temperature calculated from the default Methfessel-Paxton smearing of partially occupied orbitals.

2.5.2 Calculating Lattice Constants

Before calculating physically significant attributes of a system (geometries, adsorption energies, vibrational modes, etc.) the lattice constant of the underlying metal needs to be properly converged. The exact lattice constant for a particular metal can change depending on the functionals used and often does not exactly match the experimental value[16]. With the rise of software packages that construct initial surface geometries based on predefined lattice constants and run DFT codes all in

one step (such as the Atomic Simulation Environment (ASE)), this step can be often overlooked. Below is an example of converging the lattice constant for platinum.

The first step is to find the best set of k-points with bulk Pt that gives a consistent energy that is insensitive to the k-points used. Generally, higher k-points give more accurate results at the expense of computation time. To do this, start with the following files:

POSCAR:

```
Pt
3.95000000000
     1.000000000000000    .0000000000000000    .0000000000000000
     .0000000000000000    1.000000000000000    .0000000000000000
     .0000000000000000    .0000000000000000    1.000000000000000
  4
Selective dynamics
Direct
     0              0              0      T T T ! Pt
     0.5            0.5            0      T T T ! Pt
     0.5            0              0.5    T T T ! Pt
     0              0.5            0.5    T T T ! Pt
```

KPOINTS:

```
Automatic mesh
0
Gamma
  1  1  1
  0.  0.  0.
```

INCAR:

```
System = Pt(bulk)
 NWRITE = 1 ! determines how much will be written to the OUTCAR
 LWAVE = .FALSE. ! write WAVECAR?
 LCHARG = .FALSE. ! write CHGCAR?
 LVTOT = .FALSE. ! write LOCPOT?

Electronic relaxation
 ISMEAR = 1 ! determines how the partial occupancies fnk are set for each orbital
 EDIFF = 1e-6 !convergence criterion
 SIGMA = 0.1 ! specifies the width of the smearing in eV
 LREAL = Auto ! projection in real space (default .FALSE.)
 ROPT = 2e-4 ! one for each species in POTCAR

Ionic relaxation
 NSW = 100 ! # of steps in optimization (default 0!)
 IBRION = 1 ! 1: quasi-NR, 2:CG algorithm for ions
 NFREE  = 20 ! steps remembered (20 good for large systems)

Parallel
 NCORE = 1 ! num of cores
```

The POTCAR should be that of Pt with the desired psuedopotentials. In this case I am using PBE. In the KPOINTS file, the 1 1 1 can be changed to 2 2 2, 3 3 3, N N N and so on. After running various N k-points, N is plotted against the energy per atom as seen in Figure 2.12.

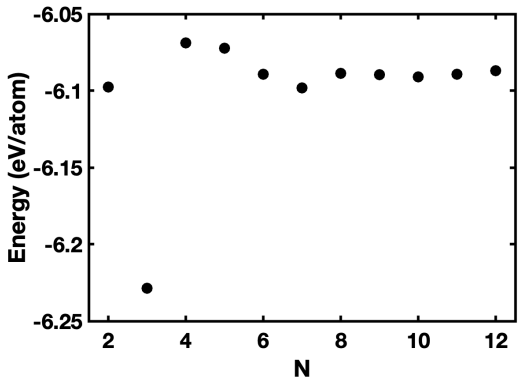


Figure 2.12 NxNxN k-point values on bulk Pt energy

For 1x1x1 k-points, the energy/atom was very different from the other k-points with a value of -0.082 eV/atom. For this analysis, it is not important which k-point scheme would give the lowest energy, rather it is what lowest k-point scheme gives the most consistent energy with higher k-points. For this system, a k-point scheme of 8x8x8 gives within 0.002 eV/atom of 12x12x12 so it is selected for lattice constant optimization.

To optimize the lattice constant, the same files as written above can be used with 8x8x8 k-points. All that needs to be changed is the 3.95 value at the top of the POSCAR. I recommended varying this value by 0.1 Å and then homing in on a narrower region to get the final optimized value. This can be seen in Figure 2.13.

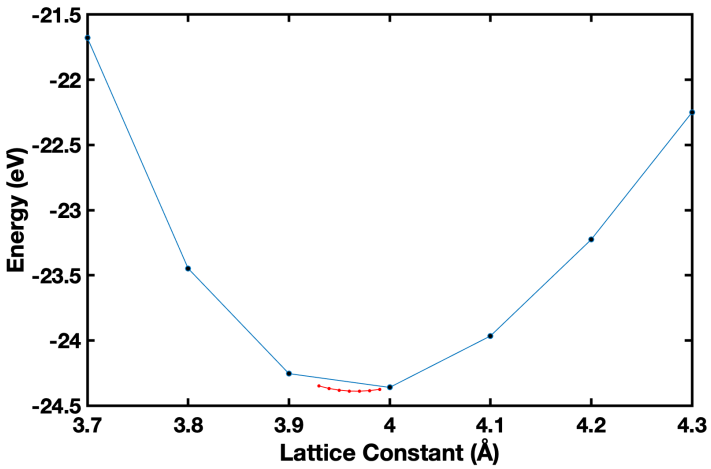


Figure 2.13 Optimization of bulk Pt lattice constant. In blue is the initial set of constants and red is a more focused region.

Going from 3.7 to 4.3 Å in 0.1 Å increments, the optimal lattice constant appeared to be between 3.9 and 4.0. Another set of calculations was done from 3.93 to 3.99 Å in 0.01 Å increments revealing the optimal lattice constant to be between 3.96 and 3.97. A function can be fit to this data and a minimum found to yield a more precise result. The optimal lattice constant for these parameters and PBE functionals was found to be 3.965 Å which is very close to the literature value of 3.985 Å[16].

2.5.3 Optimizing Surface Slabs

With the optimal lattice parameter for the bulk metal found, metal surface slabs can be constructed with a variety of indexes, cell sizes and thicknesses. These slabs are intended to represent the relevant experimental metal surfaces where chemical reactions are taking place. Therefore, the surface facet should be chosen wisely for the modeled system. For spherical nanoparticles, low-indexed surfaces dominate such as the (111), (100) and (110). For cubes, the (100) makes up much of the surface. For very small nanoparticles, < ~5 nm, higher indexed kink and edge sites become prevalent. Each surface facet has its own unique set of surface sites for molecules to bind. The (111) facet, for example, has four unique surface sites as depicted in Figure 2.14.

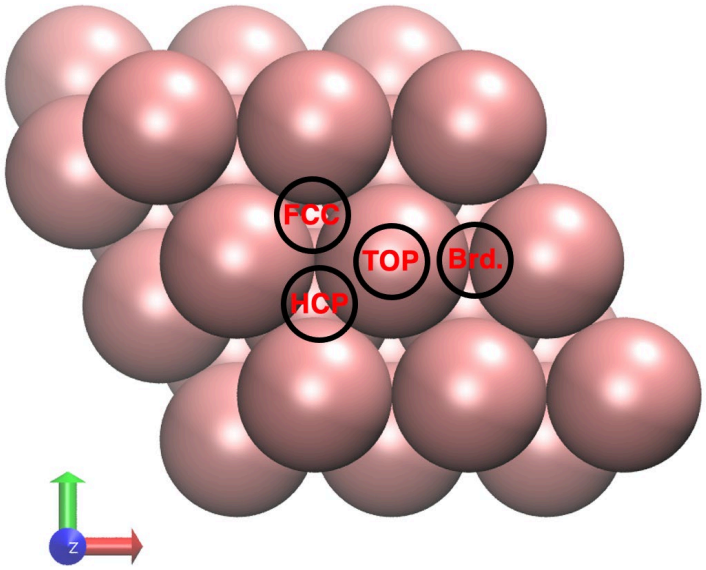


Figure 2.14 A 3x3 Pt(111) surface slab. The four catalytic sites (FCC, HCP, ATOP, and Bridge) are marked

The four sites are the three-fold hollow site (FCC), the two-fold hollow site (HCP), the on-top site (TOP or ATOP) and the bridge site. Single atom adsorbates (such as O and H) tend to prefer the highly coordinated FCC site while molecules like OH and CO prefer the TOP site[17].

Choosing the cell size is a critical consideration as it will drastically affect the computational speed, but also the adsorbate coverage. For example, in Figure 2.14 the cell size is 3x3 meaning 3 Pt atoms by 3 Pt atoms for a total of 9 Pt atoms on the surface for each unit cell. If one O atom adsorbs in an FCC site, then the coverage of O on the surface will be 1/9 monolayer (ML). Since VASP is a periodic code, the slab is repeated in all three directions. Therefore, the cell size also dictates how far each adsorbate is from the next. For a 1/9 ML O coverage, the next nearest neighbor (NN) is 3 sites away producing very little interference for the adsorption energy of O. The larger the cell size, however, the more expensive the calculations so a balance is needed. Due to VASP repeating the cell in the Z direction (or whatever direction is perpendicular to the surface) a certain amount of vacuum space is required between the top layer of the slab and the bottom layer. Generally, 15 Å is sufficient to keep interferences low without increasing computational expenses too much. The

number of layers is another critical variable in VASP calculations. As we are trying to simulate both a bulk material and a surface interface, a single layer of Pt atoms would be a very poor analog. Therefore, researchers will include multiple layers (4-5) to capture the bulk configuration more accurately. It is recommended to "freeze" the bottom few layers to represent the interior of the bulk structure and save on computation costs. The top layers should be able to move slightly to accommodate adsorbates (and lowering total energy) while the bottom layers can be restricted. This can be accomplished by changing the "T" flags in the POSCAR to "F" and using selective dynamics. Once the cell size, vacuum space and number of layers is chosen, the best k-point configuration should be optimized the same way as was done for the slab to balance computational expense and accuracy. The N k-points can be plotted against the energy per atom as before. The results for a 4 layer, 3x3 Pt(111) surface are shown in Figure 2.15 where 5x5 is chosen to minimize cost and maximize accuracy.

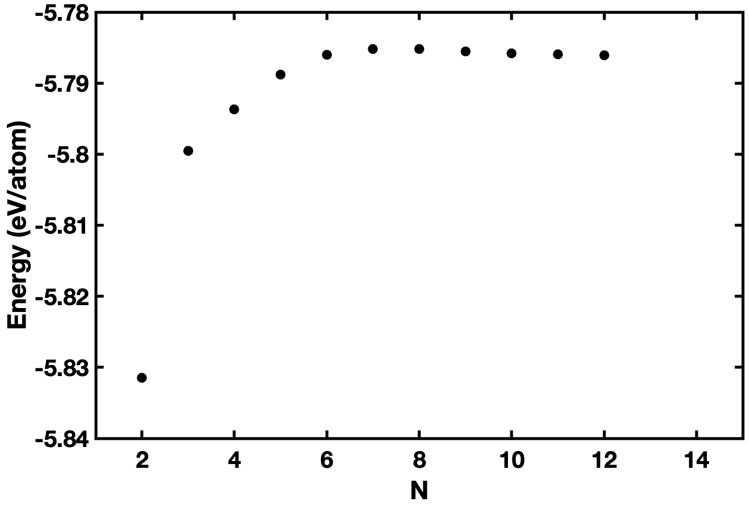


Figure 2.15 Optimal K-point configuration for a 3x3 Pt(111) slab

All DFT calculations reported in this dissertation were run on an in-house super-computing cluster. PBE functional[18,19] and PAW potentials[20,21] with an energy cut-off of 500 eV, 5x5x1 gamma centered k-point meshes are used for all calculations. As described above, the Pt lattice constant

was converged to be 3.965 Å in line with literature values[16]. All slabs are made with 4 layers with the bottom 2 layers frozen in place, except for vibrational calculations where all atoms are able to move. 15 Å of vacuum space is included above the top Pt surface layer.

2.5.4 Vibrational Mode Calculations

Calculating the vibrational modes of adsorbed species on catalytic surfaces is a powerful technique when combined with in-situ spectroscopy. This technique allows the researcher to identify the abundant intermediates on the surface by matching the observed vibrational bands with DFT predicted modes.

To perform these calculations, several methods can be utilized. For this dissertation, I used two different methods: the dynamical matrix method developed by Graeme Henkelman's group at UT-Austin[22] and the IBRION=5 method to calculate the full Hessian matrix[15]. The main differences between the two methods are that the dynamical matrix approach is much faster than IBRION=5 but it is unable to correctly predict isotopic shifts in vibrational modes. To illustrate, an oxygen molecule was added at a bridge site on the 3x3 Pt(111) surface. The vibrational mode frequencies were then calculated using the two methods with oxygen-16 atoms and heavy oxygen-18 atoms. The results are shown in Table 2.2.

Table 2.2 Vibrational mode frequencies (in cm^{-1}) for 1/9 ML O_2 on 3x3 Pt(111) calculated using the dynamical matrix method or IBRION=5 and oxygen-16 or oxygen-18.

Method	**Dynamical Matrix (cm^{-1})**		**IBRION=5 (cm^{-1})**	
mode	O_2-16	O_2-18	O_2-16	O_2-18
1	251.4	250.3	254.5	243.1
2	399.9	400.0	405.9	384.7
3	541.5	541.7	545.8	515.0
4	856.0	854.9	857.7	808.1

The differences in predicted vibrational mode frequencies are slight (<7 cm^{-1}) between the two methods with oxygen-16, but the dynamical matrix method fails to correctly capture the vibrational shift due to the heavy oxygen. Mode 4 is the symmetric oxygen-oxygen stretch that follows a Hooke's law approximation showing a nearly (6%) 50 cm^{-1} shift when switching from oxygen-16 to oxygen-18.

2.6 References

(1) Chen, R.; Yang, C.; Cai, W.; Wang, H.-Y.; Miao, J.; Zhang, L.; Chen, S.; Liu, B. Use of Platinum as the Counter Electrode to Study the Activity of Nonprecious Metal Catalysts for the Hydrogen Evolution Reaction. *ACS Energy Lett.* **2017**, *2* (5), 1070–1075. https://doi.org/10.1021/acsenergylett.7b00219.

(2) Ji, S. G.; Kim, H.; Park, C.; Kim, W.; Choi, C. H. Underestimation of Platinum Electrocatalysis Induced by Carbon Monoxide Evolved from Graphite Counter Electrodes. *ACS Catal.* **2020**, *10* (18), 10773–10783. https://doi.org/10.1021/acscatal.0c01783.

(3) Basics of EIS: Electrochemical Research-Impedance https://www.gamry.com/application-notes/EIS/basics-of-electrochemical-impedance-spectroscopy/ (accessed 2021 -09 -18).

(4) Butler, H. J.; Ashton, L.; Bird, B.; Cinque, G.; Curtis, K.; Dorney, J.; Esmonde-White, K.; Fullwood, N. J.; Gardner, B.; Martin-Hirsch, P. L.; Walsh, M. J.; McAinsh, M. R.; Stone, N.; Martin, F. L. Using Raman Spectroscopy to Characterize Biological Materials. *Nature Protocols* **2016**, *11* (4), 664–687. https://doi.org/10.1038/nprot.2016.036.

(5) Albrecht, M. G.; Creighton, J. A. Anomalously Intense Raman Spectra of Pyridine at a Silver Electrode. *J. Am. Chem. Soc.* **1977**, *99* (15), 5215–5217. https://doi.org/10.1021/ja00457a071.

(6) Jeanmaire, D. L.; Van Duyne, R. P. Surface Raman Spectroelectrochemistry: Part I. Heterocyclic, Aromatic, and Aliphatic Amines Adsorbed on the Anodized Silver Electrode. *Journal of Electroanalytical Chemistry and Interfacial Electrochemistry* **1977**, *84* (1), 1–20. https://doi.org/10.1016/S0022-0728(77)80224-6.

(7) Pilot, R.; Signorini, R.; Durante, C.; Orian, L.; Bhamidipati, M.; Fabris, L. A Review on Surface-Enhanced Raman Scattering. *Biosensors (Basel)* **2019**, *9* (2), 57. https://doi.org/10.3390/bios9020057.

(8) Aslam, U.; Chavez, S.; Linic, S. Controlling Energy Flow in Multimetallic Nanostructures for Plasmonic Catalysis. *Nature Nanotechnology* **2017**, *12* (10), 1000–1005. https://doi.org/10.1038/nnano.2017.131.

(9) Redox.me. Magnetic Mount Raman Electrochemical Flow Cell https://redox.me/collections/spectro-electrochemical-cells/products/raman-efc-4-mm-path-0-7-ml-raman-electrochemical-flow-cell.

(10) Burke, K. *The ABC of DFT*; Department of Chemistry, University of California, Irvine, CA 92697, 2007.

(11) Kresse, G.; Hafner, J. Ab Initio Molecular Dynamics for Liquid Metals. *Phys. Rev. B* **1993**, *47* (1), 558–561. https://doi.org/10.1103/PhysRevB.47.558.

(12) Kresse, G.; Hafner, J. Ab Initio Molecular-Dynamics Simulation of the Liquid-Metal--Amorphous-Semiconductor Transition in Germanium. *Phys. Rev. B* **1994**, *49* (20), 14251–14269. https://doi.org/10.1103/PhysRevB.49.14251.

(13) Kresse, G.; Furthmüller, J. Efficiency of Ab-Initio Total Energy Calculations for Metals and Semiconductors Using a Plane-Wave Basis Set. *Computational Materials Science* **1996**, *6* (1), 15–50. https://doi.org/10.1016/0927-0256(96)00008-0.

(14) Kresse, G.; Furthmüller, J. Efficient Iterative Schemes for Ab Initio Total-Energy Calculations Using a Plane-Wave Basis Set. *Phys. Rev. B* **1996**, *54* (16), 11169–11186. https://doi.org/10.1103/PhysRevB.54.11169.

(15) The VASP Manual. 2021.

(16) Haas, P.; Tran, F.; Blaha, P. Calculation of the Lattice Constant of Solids with Semilocal Functionals. *Phys. Rev. B* **2009**, *79* (8), 085104. https://doi.org/10.1103/PhysRevB.79.085104.

(17) Ford, D. C.; Nilekar, A. U.; Xu, Y.; Mavrikakis, M. Partial and Complete Reduction of O2 by Hydrogen on Transition Metal Surfaces. *Surface Science* **2010**, *604* (19–20), 1565–1575. https://doi.org/10.1016/j.susc.2010.05.026.

(18) Perdew, J. P.; Burke, K.; Ernzerhof, M. Generalized Gradient Approximation Made Simple. *Phys. Rev. Lett.* **1996**, *77* (18), 3865–3868. https://doi.org/10.1103/PhysRevLett.77.3865.

(19) Perdew, J. P.; Burke, K.; Ernzerhof, M. Generalized Gradient Approximation Made Simple [Phys. Rev. Lett. 77, 3865 (1996)]. *Phys. Rev. Lett.* **1997**, *78* (7), 1396–1396. https://doi.org/10.1103/PhysRevLett.78.1396.

(20) Blöchl, P. E. Projector Augmented-Wave Method. *Phys. Rev. B* **1994**, *50* (24), 17953–17979. https://doi.org/10.1103/PhysRevB.50.17953.

(21) Kresse, G.; Joubert, D. From Ultrasoft Pseudopotentials to the Projector Augmented-Wave Method. *Phys. Rev. B* **1999**, *59* (3), 1758–1775. https://doi.org/10.1103/PhysRevB.59.1758.

(22) Henkelman, G. *DYNAMICAL MATRIX*; http://henkelmanlab.org/vtsttools/dymmat.html.

Chapter 3 Evaluation of Electrocatalyst Activity

3.1 Introduction

Over past decades, much work has been done in developing novel electrocatalysts for various electrochemical reactions, including hydrogen oxidation, oxygen reduction, CO_2 reduction, water oxidation and N_2 reduction. Various monometallic, bimetallic, core@shell, noble metal and noble-metal free materials, in many nanoscopic form factors (*e.g.* nanoparticles of different shapes and sizes, planar structures, *etc.*) have been studied in an effort to improve electrocatalyst activity while reducing cost[1–3]. While this focus on different materials in terms of their composition and their form factors has brought a great deal of excitement to the field, it has become increasingly difficult to rigorously assess the critical figures of merit that can compare these different materials even on a relative scale[4,5]. This chapter is part tutorial and part viewpoint where we briefly discuss the figures of merit used to evaluate electrocatalysts, outline potential issues that have caught our attention as sometimes mishandled in published literature, and describe some useful practices that ensure rigorous assessment of inherent electrocatalytic activity of materials. To illustrate the central points, electrochemical oxygen reduction reaction (ORR) is used as an example. While the focus is on the ORR on Pt-based materials, we stress that the same level of rigor needs to be implemented when analyzing any electrochemical transformations and that depending on the reactions or the material this might require very different approaches.

3.2 Electrocatalytic Activity as a Figure of Merit

There are several critical "figures of merit" which are commonly used to assess the activity of electrocatalysts. **Specific activity (j_k (V))**, which is defined as the potential-dependent net kinetic current (i_k) normalized by the electrochemically active surface area (ECSA) (mA/cm^2), represents a measure of the surface activity of an electrocatalyst material. This is a critical metric that allows us to rigorously assess and compare the inherent activities of different materials. In our view, if the subject of a research effort is to study intrinsic electrocatalytic activity of a material or the mechanism of electrochemical reactions on an electrocatalyst surface, specific activity is the most important figure of merit that should always be reported. We note that if not all surface sites are active, as is the case on carbon-based electrocatalysts, then in order to obtain relevant kinetic information the kinetic currents need to be normalized by the number of active sites. Rigorously counting the active sites is a significant problem that for most materials has not been adequately solved. The **mass activity**, which is the net kinetic current normalized by the mass of the electrocatalyst (generally reported as $A/mg_{catalyst}$) and the **volumetric activity** (the net kinetic current normalized by the volume occupied by the electrocatalyst) are not only a function of the inherent activity of the material's surface (the specific activity) but also of the form factor that the material takes. For example, larger nanoparticles will have lower mass and volumetric activity than smaller nanoparticles, for an identical material with identical specific activity. While the mass and volumetric activities can be important for the technoeconomic evaluation of an electrocatalyst in a device (such as a fuel cell), these two metrics are less useful when reporting the inherent activity of a material due to the above-mentioned impact of the form factors on these metrics. Another figure of merit that is often used in the literature is the **half-wave potential,** defined as the potential where one-half of the mass transport-limiting current is reached[6]. The half-wave

potential can be used to compare the inherent activities of different materials, only if its measurement is based on properly normalizing for the effect of the ECSA. Comparing the half-wave potential (not normalized for the impact of ECSA) of two materials that have very different surface areas exposed to electrolyte should not be used to assess the relative electrochemical activity of these materials, since higher ECSA of a material compensates for a poor inherent activity. Our random sampling of 20 recently published papers in the field of ORR electrocatalysis that used half-wave potential to assess the activity of a material found that 11 did not account for the impact of different surface areas of the materials that were tested.

3.3 Measuring Electrocatalyst Activity using Rotating Disk Electrodes

Typically, these figures of merit, including the specific activity, are measured using a rotating disk electrode (RDE) setup. In one version of the measurements, the electrocatalyst activity is studied by creating a flat nonporous electrode of the electrocatalytic material, such as a polycrystalline or single crystal metal or metal alloy surface. For ORR measurements this flat RDE is placed in an oxygen-saturated electrolyte at a set rotation speed (often 1600 RPM) and connected to a reference and counter electrode. Current-potential (IV) curves are collected as the function of the voltage of the working electrode (and therefore the electrocatalyst potential), and usually reported on the reversible hydrogen electrode (RHE) scale. An example of data obtained on a flat RDE of polycrystalline Pt in ORR is shown in Figure 3.2. The data analysis in these systems is commonly based on the Koutecky-Levich approach, which assumes that there are two potential-dependent regimes that control the appearance of the IV curves. At high overpotential, the measured current is controlled by the rate of external mass transport of reactants (in ORR it is O_2) from the bulk of the electrolyte to the electrocatalytically active layer on the RDE, while at low overpotentials the reaction rate is controlled by the inherent net kinetic current of the active material (the net rate of

the reactions taking place at the electrocatalyst surface). To separate the net kinetic current from the external mass transport limiting current, the total measured current is broken down using the Koutecky-Levich equation:

$$i = \left(\frac{1}{i_k} + \frac{1}{i_m}\right)^{-1} \quad (1)$$

Where i is the net current measured, i_k is the net kinetic current and i_m is the external mass transport limiting current. The mass transport limiting current (which is dependent on several factors including the RDE rotation speed) can be extracted from the IV curve as the potential independent current at high overpotentials. For ORR on Pt surfaces this is typically the current around 0.5 V vs. RHE, where the reaction is almost completely controlled by the rate of oxygen transport from the bulk of liquid electrolyte to the electrocatalyst layer. For flat electrodes, the analysis allows us to rigorously evaluate the specific current by dividing the net kinetic current by the electrochemically active surface area (ECSA), which in this case is the geometric area of the electrode.

It is often not possible to have electrocatalytic materials in the polycrystalline or single crystal form factors, and there is a practical need to compare the activity of materials structured in different nanoscopic form factors (different shapes and sizes of nanoparticles) deposited on a RDE. In this setup, a thin porous active layer of electrocatalyst (usually electrocatalyst nanostructures are mixed with a porous carbon such as carbon black) is supported on an inert "non-porous" electrode (such as glassy carbon). This setup is known as thin-film rotating disc electrode (TF-RDE).

The IV data obtained in the TF-RDE setup is also analyzed using the Koutecky-Levich equation. We note that before applying the Koutecky-Levich analysis, all currents need to be corrected for the capacitive current caused by the electrochemical double layer (see Chapter 2). This can be very important when high surface area supports (like carbon black) are used to support the active

nanoparticle electrocatalysts. In these systems, electrical charging of the double layer can greatly alter the IV curve. One has to be mindful that in these systems, the reaction rate (*i.e.*, the net measured current) is affected not only by the rate of external mass transport of reactants (in the case of ORR, it is O_2) from the electrolyte bulk to the surface of the outmost electrocatalyst layer and the net kinetic reaction rates, but also by the internal diffusion limitations from the outmost electrocatalyst layer to the electrochemically active sites, some of which are removed from that layer and reside inside the pores of the thin film[7]. We note that for flat electrode surfaces discussed above, such as polycrystalline metallic plates, the internal diffusion limitations are non-existent since all active sites are in the outmost electrocatalyst layer and therefore easily accessible to the reactants. On the other hand, for nanoscopic form factors where nanoparticles of different shapes are packed in the porous carbon material, these internal diffusion limitations, which affect the transport of reactants (such as O_2) to the active sites, can be significant and important.

The impact of internal diffusion limitations on the measured reaction rate can be described using the concept of electrochemical effectiveness factor (EF). EF essentially represents the ratio of the measured net kinetic reaction rate to the rate that assumes no mass transport limitations. While EF can be rigorously derived if certain assumptions are made about the pore geometry that the reactant needs to navigate through the porous material to reach the active centers, EF generally takes the form of eq 2.

$$EF = \frac{i_k}{i_{k,0}} = \frac{\tanh(\phi_{Th})}{\phi_{Th}} \tag{2}$$

Where i_k and $i_{k,0}$ are the kinetic currents affected and unaffected by diffusion in the active electrocatalyst layer respectively, and ϕ_{Th} is the Thiele modulus. For low values of Thiele modulus (< than 0.1), EF is close to 1, and for higher values of Thiele modulus EF becomes increasingly smaller, asymptotically reaching $1/\phi_{Th}$. The Thiele modulus is controlled by several factors

including the active electrocatalyst layer depth (L), the diameter of the pores (D) that the reactants navigate in the active electrocatalyst layer (also affected by the packing density of the nanoparticles), the concentration (C_r) and diffusion coefficient (D_r) of the reactants and the reaction rate (j). As opposed to thermal catalytic systems and specific to electrochemical systems, the Thiele modulus is also dependent on the ohmic resistance (Ω) and ionic conductivity (σ) of the active layer.[8–10]

$$\phi_{Th} \sim f(L, D, C_r, D_r, j, \Omega, \sigma) \quad (3)$$

It is important to analyze how some of these parameters impact the Thiele modulus of an active electrocatalyst layer. For example, a thicker active porous layer with smaller pores and more crowded nanoparticles will increase the Thiele modulus and lower the measured kinetic current of the electrocatalyst. Conversely, larger pores (less crowding of the electrocatalyst particles) and thinner active layers will decrease the Thiele modulus. Furthermore, larger kinetic currents will also lead to a larger Thiele modulus, i.e., the effectiveness factor is a function of overpotential, and for a given system the effectiveness factor is smaller at larger overpotentials.

To demonstrate how Thiele modulus and EF can affect experimental IV curves, we applied eq 2 to a set of data that we obtained using a planar polycrystalline Pt electrode (which has no internal diffusion limitations, EF = 1) in electrochemical ORR. This data was obtained by using a planar Pt-poly (Pine) fixed electrode in a traditional 3-electrode RDE setup. An in-house built all Teflon cell housed the reference electrode (Hg/HgO, Pine), counter electrode (Pt wire, Fisher) and the 0.1 M NaOH (30 wt%, Fisher). The reference electrode was calibrated against the reversible hydrogen electrode (RHE) in H_2 (UHPG) saturated electrolyte before ORR voltammograms were measured. Surface area was measured in Ar (UHPG) saturated electrolyte by integrating the H-UPD potential region (0.05-0.4 V vs. RHE) of the Pt surface using a CO-poisoned baseline further described later in the chapter. The solution resistance was measured to be 40 ohms using hybrid electrochemical

impedance spectroscopy. ORR measurements were done in O_2 (UHPG) saturated electrolyte which was purged with gas for at least 20 minutes. A linear sweep voltammogram showing the Tafel plot of kinetic current density is shown in Figure 3.1.

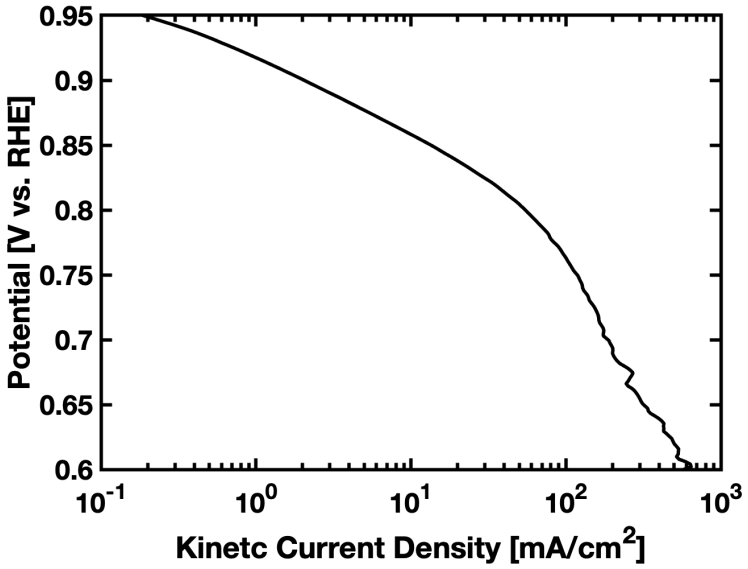


Figure 3.1 Tafel plot of the ORR current density for a Pt-poly electrode rotating at 1600 RPM in O_2 saturated 0.1 M NaOH. Currents are corrected for solution resistance loses and the capacitive current from the electrochemical double layer.

The Thiele modulus in the effectiveness model was based off of equation 4:

$$\phi_T = \sqrt{\frac{\Gamma K \gamma L^2}{nFD_c} * \frac{1}{j_0} * j_k(pt)} \tag{4}$$

Where ϕ_T is the Thiele modulus, Γ is a temperature parameter, K is a lump kinetic term, γ is the surface area to volume ratio of the pores, L is the film thickness, n is the number of electrons transferred, F is Faraday's constant, D_c is the diffusion coefficient, j_0 is the exchange current density and j_k is the kinetic current density of the Pt-poly electrode. The values used for the constants are shown in Table 3.1. The overpotential loses through the active layer, which depend on the ionic conductivity of the film, was not included in our model.

Table 3.1 Parameters used in the Thiele modulus equation

Parameter	Value [units]
Γ	6
K	$12.2*10^{-6}$ [A/cm^2]
γ	0.0037 [cm^{-1}]
L	varied [cm]
n	4
D_c	$12*10^{12}$ [$mol*cm^{-1}s^{-1}$]
j_0	$2.4*10^{-7}$ [$A*cm^{-2}$]

The data in Figure 3.2a show that an increase in the Thiele modulus, which leads to a decrease in the effectiveness factor of the electrocatalyst, results in the IV curves that have two characteristic differences compared to the data unimpeded by the internal diffusion limitations. The differences are that for systems with low EF, the slope of the IV curve in the region where the reactions rate (current) takes off is lower and the mass transport limiting current is reached at larger overpotential. An inspection of published data suggests that these behaviors (low EF) are exhibited in many systems where various materials with different nanoscale form factors are studied and compared to each other, indicating that in these studies there were artifacts that resulted in internal diffusion limitations which compromised the results and conclusions. We note that the Thiele modulus is higher at higher overpotentials (higher currents), and therefore the EF is lower and the deviation from the true kinetic current is greater as shown in Figure 3.2b and c.

To avoid these internal diffusion limitations, it is recommended that electrocatalyst nanostructures are well dispersed on a conductive porous support with an active layer film thickness of < 0.1 μm

in the TF-RDE setup[11–13]. While it is proposed that under these conditions a low Thiele modulus can be achieved, one has to be cognizant of the fact that Thiele modulus is effectively a dimensionless number that quantifies the ratio between kinetic reaction rates and internal diffusion rates.[8,14,15] As such, it is highly dependent on the particular geometry of the system (including the local packing of nanostructures and their shape), the size of the pores in the material that is packed on the TF-RDE, the reactant and product diffusion constants in the electrolyte as well as the rates of electrochemical reactions. Therefore, when comparing the electrochemical activity of different nanoscale form factors for different materials it is important to assess the values of Thiele moduli to make sure that the internal diffusion rates of reactants are not significantly impacting the results.

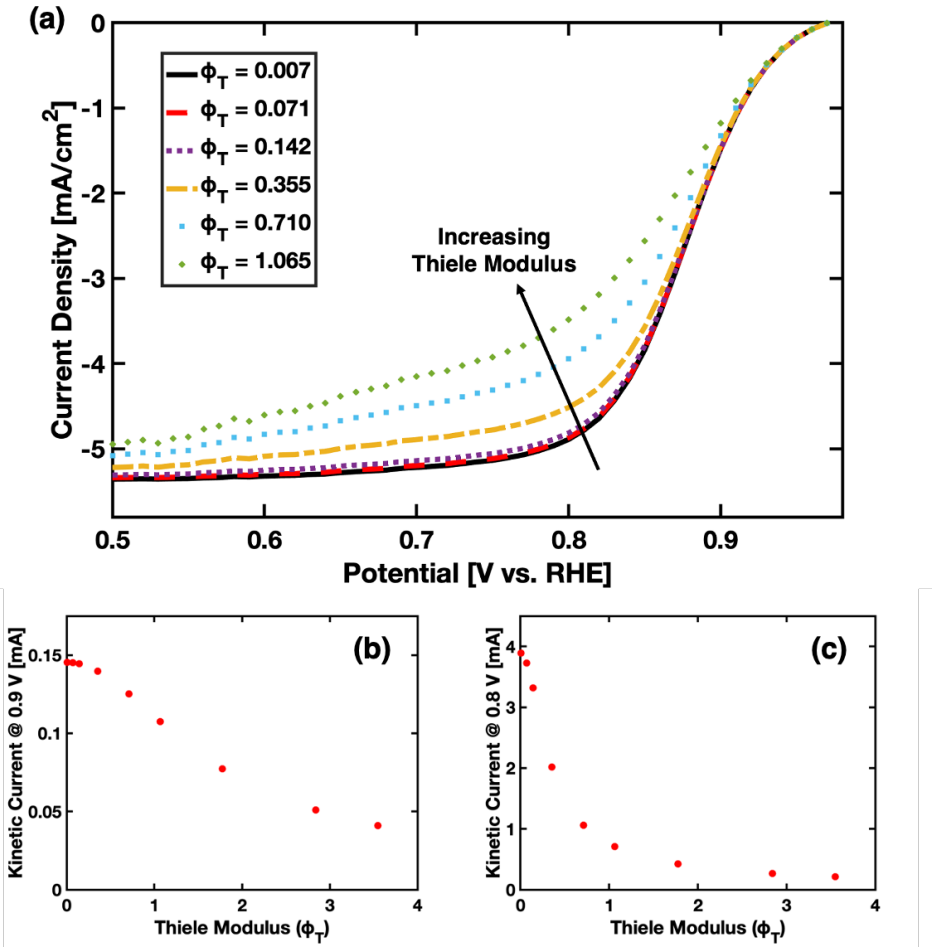


Figure 3.2: (a) RDE linear sweep voltammograms for a Pt-poly electrode in oxygen saturated 0.1 M NaOH at 1600 RPM. An effectiveness factor model is imposed on the data to simulate the effects of various Thiele moduli. As the Thiele modulus increases, the electrode requires a greater overpotential to reach the mass limiting current. (b) Effects of the Thiele modulus on the kinetic current measured at 0.9 V vs. RHE and (c) at 0.8 V vs. RHE using a model from the literature.

Though the accurate calculation of electrocatalyst activity can be compromised due to slow diffusion in the active layer (low EF and large Thiele modulus) in TF-RDE as detailed above, we find that even greater misrepresentations of electrocatalyst activity originate from improper measurements of electrocatalyst surface area (ECSA). To obtain an accurate measure of specific electrocatalyst activity, the net kinetic current (i_k) must be normalized against an accurately measured ECSA of the electrocatalyst. Accurate measurements of ECSA are critical for assessing relevant activity of different materials and comparing their performance. Unfortunately, a random

sampling of 20 recent papers on ORR electrocatalysis found that ~ 50 % failed to properly normalize the kinetic current density against ECSA. In the following section we describe experimental procedures used to accurately determine ECSA. Our focus is on Pt-based electrocatalysts, where electrochemical transformations take place on Pt surface sites. We note that comparing the activity of materials different than Pt requires a similar level of rigor for ECSA evaluations.

3.4 Techniques for Characterizing ECSA

3.4.1 Underpotential Deposition

One of the most common techniques for evaluating electrocatalyst surface area is underpotential deposition (UPD)[16]. This is a voltammetric method in which the charge involved in electrochemically adsorbing/desorbing an adlayer of a selected chemical species is measured by integrating the area under the IV curve in the UPD region. For Pt group metals like Pt, Ir, Ru, Rh, and Pd, atomic hydrogen can be used[17–21] while for Ag, atomic lead (Pb) can be used[22–24]. Cu-UPD can also be used for a variety of metals including Au, Pt, Ru and Ag[25,26].

For Pt based electrocatalysts, hydrogen-underpotential deposition (H_{UPD}) is most commonly used to measure the ECSA. The Pt surface area is determined by integrating the IV-curve from ~ 0.05 – 0.4 V *vs.* RHE under a suitable (nonadsorbing) electrolyte condition. This integration yields the charge associated with desorption of an underpotentially deposited adlayer of H (H_{UPD}) and can be converted to surface area through a conversion factor of 210 μC/cm^2 (charge associated with electrochemical desorption of one H layer on a Pt surface)[27,28]. It should be noted that the dominant Pt facet will affect the conversion factor, necessitating precise nanoparticle characterization for the most accurate surface area measure[5]. To obtain accurate ECSA measurements from the current

associated with the desorption of H_{UPD} through the integration of the IV curve, the background (noise) current (both potential dependent and independent) must be properly removed. Commonly, the potential-independent, double layer capacitive current is assumed to be half of the difference between the limiting current of the anodic and cathodic sweeps between 0.4 and 0.5 V vs. RHE. This is reflected in Figure 3.3 as the horizontal, dashed baseline from 0.05 to 0.40 V *vs.* RHE. The measured H_{UPD} desorption peak is then reduced by this amount to remove contributions from the surface capacitance[29]. The background current can also include potential-dependent contributions (often related to the catalyst support effects) in addition to the constant capacitive current, leading to a potential dependent baseline rather than a horizontal baseline[27,30,31]. One way these potential dependent currents can be accounted for is by using a slanted baseline as shown by the dashed lines in Figure 3.3[26]. Using the horizontal over the sloped baseline for the background subtraction can have a large effect on the measured ECSA. We demonstrated this in Figure 3.3, where we measured ECSA for a commercial, high surface area Pt/C electrocatalyst and a Pt monolayer core-shell electrocatalyst (Pt on Ag/Cu alloy), deposited on carbon, developed in our laboratory. Using the sloped rather than horizontal baseline resulted in a measured ECSA increase of ~45% for the core-shell electrocatalyst, resulting in a dramatic decrease in calculated activity. A downside to this approach is that the choice of slope for the slanted baseline is somewhat subjective, leading to uncertainty in the measurement.

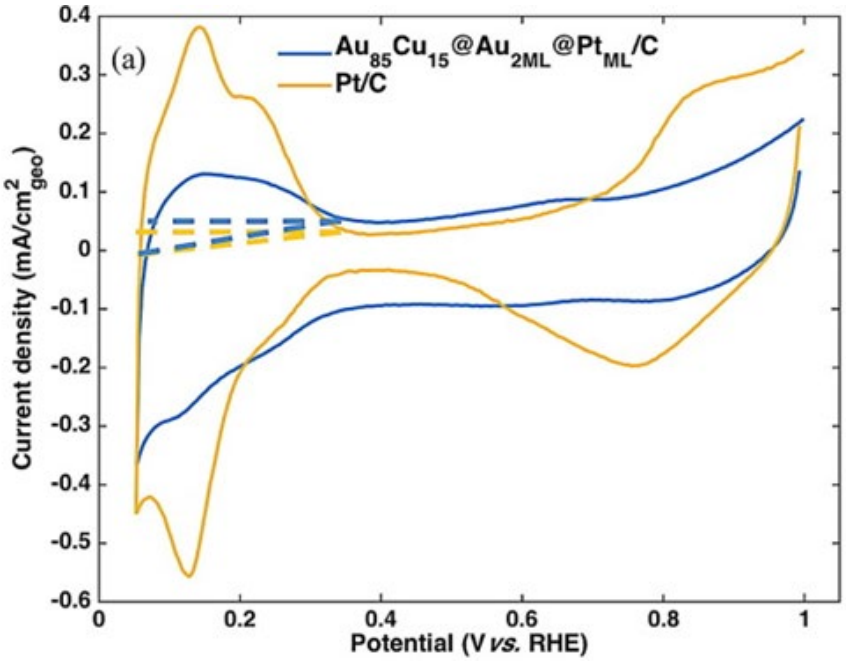


Figure 3.3 H_{UPD} analysis for a pure Pt (yellow) and Pt monolayer electrocatalyst (blue) developed within our group. The H_{UPD} peak is integrated from 0.05 to 0.40 V vs RHE using either a constant or slanted baseline shown by the dotted lines. CV curves were obtained in Ar saturated 0.1 M $HclO_4$ using a scan rate of 50 mV/s without electrode rotation.

Another disadvantage of using the HUPD method for surface area calculations stems from the assumption that HUPD atoms cover the entire electrocatalyst surface, which is most likely the case (based on extensive single crystal studies) for pure monometallic Pt samples but might not be the case for some Pt alloys. Changes in electrocatalyst electronic structure due to alloying can affect the adsorption energy of the H atoms and therefore can impact the H coverage[28,32]. For example, $Pt_3Ni(111)$ was shown to not adsorb a complete monolayer of HUPD resulting in sometimes erroneously low surface area and an artificially high specific activity reports for this alloy[33]. To correct for this incomplete adsorption, modified ECSA calculation methods have been developed that account for the less than 1 coverage of HUPD on the surface such as shown in equation 5:

$$ECSA = \frac{Q_H}{\theta_H * 210\ \frac{\mu C}{cm^2}} \tag{5}$$

Where Q_H is the charge associated with H_{UPD} desorption and θ_H is the hydrogen coverage. It is important to recognize that rigorous characterization of the surface coverage θ, under relevant electrochemical conditions, has not been widely adopted in the literature, with most reports in the literature assuming a value of unity for any Pt tested Pt alloy[34].

3.4.2 Carbon Monoxide (CO) Stripping

Due to the uncertainties associated with the H coverage on Pt alloy electrocatalysts, other voltammetric techniques such as CO stripping have been investigated[28,35,36]. In CO stripping experiments, an adlayer of CO is adsorbed on the electrocatalyst surface at reducing potentials (e.g. 0.05 V vs. RHE for Pt surfaces) prior to the electrolyte being purged with an inert gas to remove any unbound CO. The potential is then swept to higher potentials and CO is oxidized from the surface. Similar to the H_{UPD} technique, the surface area can be determined by integrating the CO oxidation peak and converted to the ECSA by a conversion factor of 420 μC/cm^2 (*i.e.*, this is a 2-electron oxidation process)[28,37,38]. One major advantage of CO stripping for ECSA characterization is that on Pt alloys and pure Pt electrocatalysts the saturation CO surface coverage tends to be identical, which removes some degree of uncertainty present in the H_{UPD} method[28,33]. The baseline for integration (i.e. the background subtraction) can be viewed in the same way as for the H_{UPD} method. During the oxidation of CO in the anodic sweep, other currents such as those associated with OH adsorption on the Pt surface and Pt-oxide formation occur and need to be corrected for. This can be accomplished by subtracting the anodic current measured post-stripping (when there is no longer CO on the surface) from the CO-stripping current. This operation yields only the net current associated with CO oxidation. Data in Figure 3.4 show the effect of background current subtraction on the measured current and therefore the measured ECSA. We note that the CO oxidation peak from 0.7 to 0.8 V *vs.* RHE is higher when the background current

is not subtracted out (dashed line) compared with the peak when the background current is properly subtracted (solid line). The data in Figure 3.4 show that for the Au-Cu/Pt core-shell and Pt commercial standard electrocatalysts, the measured ECSA was reduced by ~4% and ~15% respectively when using the potential-dependent baseline to remove the background noise.

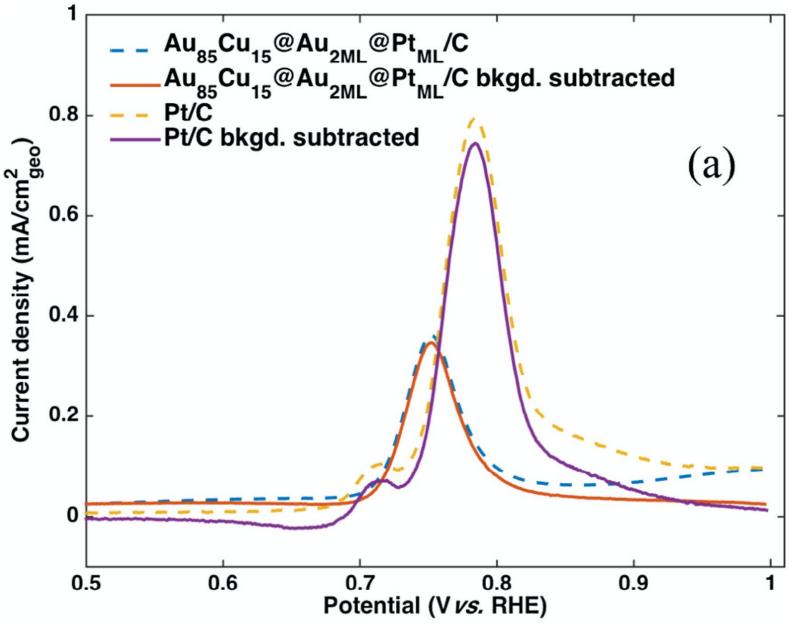


Figure 3.4 CO stripping voltammogram (scan rate: 10 mV/s) for Pt/C and Pt-monolayer electrocatalyst in Ar saturated 0.1 M $HClO_4$ electrolyte under no rotation. Raw currents are shown as dashed lines while the background subtracted currents are shown as solid lines.

3.4.3 Baseline-Corrected H_{UPD} Measurements

The two techniques, H_{UPD} desorption and CO-stripping, can be combined to give us more certainty in removing the background current in the H_{UPD} ECSA measurements for Pt electrocatalysts. The process entails saturating the Pt electrocatalyst surface with a layer of CO (holding potential at 0.05 V vs. RHE). On this CO-poisoned Pt surface the adsorption of H_{UPD} is prevented by the CO molecules. As the potential is increased from 0.05 V to 0.4 V, the background current in the H_{UPD} region, associated with the CO-poisoned Pt surface, is recorded. CO is then removed from the surface via CO oxidation and H can adsorb on the clean surface in subsequent scans. If we assume

that CO is exclusively adsorbed on the Pt surface sites and that it blocks these sites against the H_{UPD} adsorption, then subtracting the CO poisoned scan from the CO-free scan in the H_{UPD} region yields the net current of the electro-oxidation of H_{UPD} free of background currents (potential dependent and independent) giving us a measure of the ECSA.

Figure 3.5 shows the specific activity of the commercial Pt standard and the Pt monolayer core-shell catalyst at 0.9 V vs RHE that we obtained using H_{UPD} (protocol 1 & 2), CO stripping (protocol 3 & 4), and the joint CO-stripping/H_{UPD} approach (protocol 5) to characterize ECSA. We note that for these samples the H_{UPD} protocols lead to specific activities 2.5 to 3 times higher than the CO-stripping protocols while the combined approach provides a specific activity in the middle between H_{UPD} and CO stripping. We find the combined technique (protocol 5) to be a good balance in the overestimation of ECSA from CO-stripping and the underestimation of ECSA from the H_{UPD} method[29] as seen in Figure 3.5. Ideally, a combination of methods would be reported to establish a range of electrocatalyst activities and assess the error.

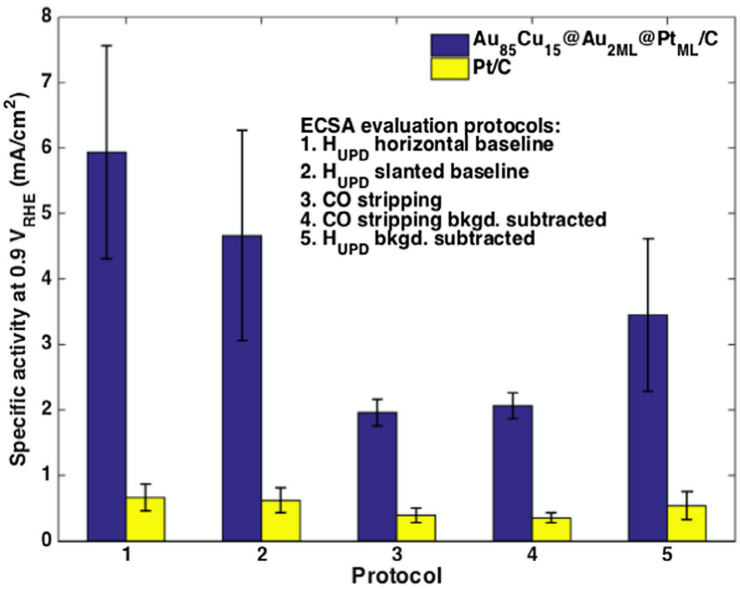


Figure 3.5 ORR specific activities for the different ECSA measuring protocols. Results for both the novel and standard Pt electrocatalyst are shown in blue and yellow respectively. Error bars represent the standard deviation of the ECSA measurements.

Once the ECSA has been calculated, the specific activity can be produced simply by dividing the kinetic current by the ECSA at a particular overpotential. Typically, for Pt surface a working electrode potential of 0.9 V vs. RHE is chosen. Mass and volumetric activities can then be calculated using the electrocatalyst loading and density. Half-wave potentials can be measured by regenerating the IV curve using the ECSA-normalized kinetic current density and the RDE area-normalized limiting current as shown in equation 6. The resulting IV curve will be the properly normalized current density vs. applied potential and the accurate half-wave potential can be found.

$$j = \left(\frac{A_{ECSA}}{i_k} + \frac{A_{RDE}}{i_l}\right)^{-1} \tag{6}$$

The data in Figure 3.6 shows the impact of over- or under-estimated ECSA on the normalized IV curves. As can be seen, the inaccuracies in the measurements of ECSA manifest itself in shifting of the typical IV S-curve with respect to the potential.

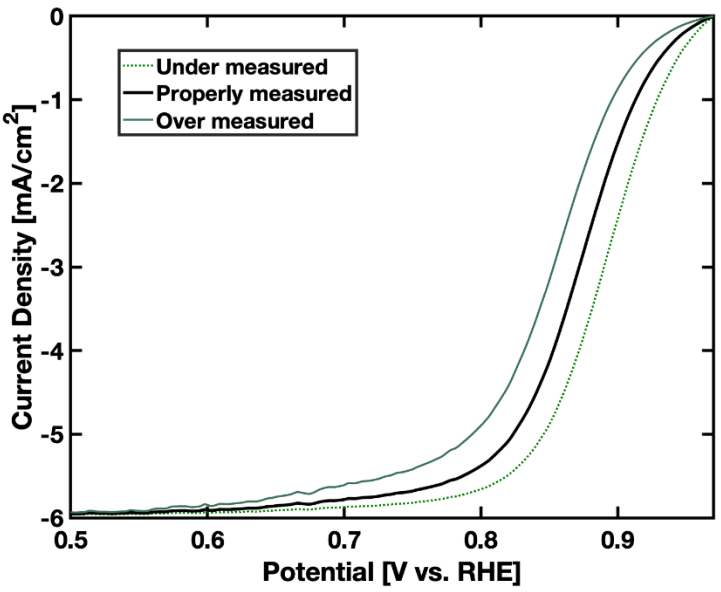


Figure 3.6 RDE linear sweep voltammograms for a Pt-poly electrode in oxygen saturated 0.1 M NaOH at 1600 RPM. In black is the properly normalized IV curve using equation 6 (in the case of Pt-poly electrode $A_{ECSA} = A_{RDE}$).

The dotted green line represents a normalized IV curve derived if the magnitude of A_{ECSA} is underestimated to 50 % of the real value and the full green line represents a normalized IV curve assuming a two-fold overestimated A_{ESCA}.

3.5 Conclusion

Rigorous evaluation of activity of electrocatalysts is critical for the quantification of their absolute and relative performance. Unfortunately, literature is full of examples of inaccurate assessment of electrocatalyst activity. These inaccuracies are amplified when very different materials are compared to each other (i.e., Pt versus carbon-based materials) or when different nanostructure form factors are used (i.e., solid nanoparticles versus nanocages, etc). In this chapter, critical figures of merit for electrocatalyst activity were discussed, focusing on potential sources of error associated with quantifying the activity of nanostructured electrocatalysts. We show that internal diffusion limitations within a porous electrocatalyst's support can impact the measurements. These diffusion limitations can be quantified by electrochemical effectiveness factor and Thiele modulus. Additionally, we discuss the importance of proper ECSA measurements on activity metrics. We present several techniques (*i.e.* H_{UPD}, CO stripping and various combinations of the two techniques) to characterize the ECSA for monometallic Pt and Pt alloys.

3.6 References

(1) Huang, X.; Zhao, Z.; Cao, L.; Chen, Y.; Zhu, E.; Lin, Z.; Li, M.; Yan, A.; Zettl, A.; Wang, Y. M.; Duan, X.; Mueller, T.; Huang, Y. High-Performance Transition Metal–Doped Pt3Ni Octahedra for Oxygen Reduction Reaction. *Science* **2015**, *348* (6240), 1230–1234. https://doi.org/10.1126/science.aaa8765.

(2) Wang, D.; Xin, H. L.; Hovden, R.; Wang, H.; Yu, Y.; Muller, D. A.; DiSalvo, F. J.; Abruña, H. D. Structurally Ordered Intermetallic Platinum–Cobalt Core–Shell Nanoparticles with Enhanced Activity and Stability as Oxygen Reduction Electrocatalysts. *Nature Materials* **2013**, *12* (1), 81–87. https://doi.org/10.1038/nmat3458.

(3) Cleve, T. V.; Moniri, S.; Belok, G.; More, K. L.; Linic, S. Nanoscale Engineering of Efficient Oxygen Reduction Electrocatalysts by Tailoring the Local Chemical Environment of Pt Surface Sites. *ACS Catal.* **2017**, *7* (1), 17–24. https://doi.org/10.1021/acscatal.6b01565.

(4) Watzele, S.; Hauenstein, P.; Liang, Y.; Xue, S.; Fichtner, J.; Garlyyev, B.; Scieszka, D.; Claudel, F.; Maillard, F.; Bandarenka, A. S. Determination of Electroactive Surface Area of Ni-, Co-, Fe-, and Ir-Based Oxide Electrocatalysts. *ACS Catal.* **2019**, *9* (10), 9222–9230. https://doi.org/10.1021/acscatal.9b02006.

(5) Wei, C.; Rao, R. R.; Peng, J.; Huang, B.; Stephens, I. E. L.; Risch, M.; Xu, Z. J.; Shao-Horn, Y. Recommended Practices and Benchmark Activity for Hydrogen and Oxygen Electrocatalysis in Water Splitting and Fuel Cells. *Advanced Materials* **2019**, *31* (31), 1806296. https://doi.org/10.1002/adma.201806296.

(6) Gasteiger, H. A.; Kocha, S. S.; Sompalli, B.; Wagner, F. T. Activity Benchmarks and Requirements for Pt, Pt-Alloy, and Non-Pt Oxygen Reduction Catalysts for PEMFCs. *Applied Catalysis B: Environmental* **2005**, *56* (1), 9–35. https://doi.org/10.1016/j.apcatb.2004.06.021.

(7) Shih, Y.-H.; Sagar, G. V.; Lin, S. D. Effect of Electrode Pt Loading on the Oxygen Reduction Reaction Evaluated by Rotating Disk Electrode and Its Implication on the Reaction Kinetics. *J. Phys. Chem. C* **2008**, *112* (1), 123–130. https://doi.org/10.1021/jp071807h.

(8) Gloaguen, F.; Convert, P.; Gamburzev, S.; Velev, O. A.; Srinivasan, S. An Evaluation of the Macro-Homogeneous and Agglomerate Model for Oxygen Reduction in PEMFCs. *Electrochimica Acta* **1998**, *43* (24), 3767–3772. https://doi.org/10.1016/S0013-4686(98)00136-4.

(9) Lin, R.-B.; Shih, S.-M. Effects of Mass Transfer on Kinetics of Hydrogen Oxidation Reaction at Nafion/Pt-Black Thin-Film Electrodes. *Journal of the Taiwan Institute of Chemical Engineers* **2013**, *44* (3), 393–401. https://doi.org/10.1016/j.jtice.2012.12.001.

(10) Nam, J. H. Electrochemical Effectiveness Factors for Butler-Volmer Reaction Kinetics in Active Electrode Layers of Solid Oxide Fuel Cells. *J. Electrochem. Sci. Technol* **2017**, *8* (4), 344–355. https://doi.org/10.33961/JECST.2017.8.4.344.

(11) Garsany, Y.; Singer, I. L.; Swider-Lyons, K. E. Impact of Film Drying Procedures on RDE Characterization of Pt/VC Electrocatalysts. *Journal of Electroanalytical Chemistry* **2011**, *662* (2), 396–406. https://doi.org/10.1016/j.jelechem.2011.09.016.

(12) Ke, K.; Hiroshima, K.; Kamitaka, Y.; Hatanaka, T.; Morimoto, Y. An Accurate Evaluation for the Activity of Nano-Sized Electrocatalysts by a Thin-Film Rotating Disk Electrode: Oxygen Reduction on Pt/C. *Electrochimica Acta* **2012**, *72*, 120–128. https://doi.org/10.1016/j.electacta.2012.04.004.

(13) Garsany, Y.; Ge, J.; St-Pierre, J.; Rocheleau, R.; Swider-Lyons, K. E. Analytical Procedure for Accurate Comparison of Rotating Disk Electrode Results for the Oxygen Reduction Activity of Pt/C. *J. Electrochem. Soc.* **2014**, *161* (5), F628. https://doi.org/10.1149/2.036405jes.

(14) Schmidt, T. J.; Gasteiger, H. A.; Stäb, G. D.; Urban, P. M.; Kolb, D. M.; Behm, R. J. Characterization of High-Surface-Area Electrocatalysts Using a Rotating Disk Electrode Configuration. *J. Electrochem. Soc.* **1998**, *145* (7), 2354–2358. https://doi.org/10.1149/1.1838642.

(15) Gloaguen, F.; Durand, R. Simulations of PEFC Cathodes: An Effectiveness Factor Approach. *Journal of Applied Electrochemistry* **1997**, *27* (9), 1029–1035. https://doi.org/10.1023/A:1018478324564.

(16) Herrero, E.; Buller, L. J.; Abruña, H. D. Underpotential Deposition at Single Crystal Surfaces of Au, Pt, Ag and Other Materials. *Chem. Rev.* **2001**, *101* (7), 1897–1930. https://doi.org/10.1021/cr9600363.

(17) Doña Rodríguez, J. M.; Herrera Melián, J. A.; Pérez Peña, J. Determination of the Real Surface Area of Pt Electrodes by Hydrogen Adsorption Using Cyclic Voltammetry. *J. Chem. Educ.* **2000**, *77* (9), 1195. https://doi.org/10.1021/ed077p1195.

(18) Paulus, U. A.; Wokaun, A.; Scherer, G. G.; Schmidt, T. J.; Stamenkovic, V.; Markovic, N. M.; Ross, P. N. Oxygen Reduction on High Surface Area Pt-Based Alloy Catalysts in Comparison to Well Defined Smooth Bulk Alloy Electrodes. *Electrochimica Acta* **2002**, *47* (22), 3787–3798. https://doi.org/10.1016/S0013-4686(02)00349-3.

(19) Zhan, D.; Velmurugan, J.; Mirkin, M. V. Adsorption/Desorption of Hydrogen on Pt Nanoelectrodes: Evidence of Surface Diffusion and Spillover. *J. Am. Chem. Soc.* **2009**, *131* (41), 14756–14760. https://doi.org/10.1021/ja902876v.

(20) Trasatti, S. Development of the Work Function Approach to the Underpotential Deposition of Metals. Application to the Hydrogen Evolution Reaction*. *Zeitschrift für Physikalische Chemie* **1975**, *98* (1–6), 75–94. https://doi.org/10.1524/zpch.1975.98.1-6.075.

(21) Łosiewicz, B.; Martin, M.; Lebouin, C.; Lasia, A. Kinetics of Hydrogen Underpotential Deposition at Ruthenium in Acidic Solutions. *Journal of Electroanalytical Chemistry* **2010**, *649* (1), 198–205. https://doi.org/10.1016/j.jelechem.2010.04.002.

(22) Kirowa-Eisner, E.; Bonfil, Y.; Tzur, D.; Gileadi, E. Thermodynamics and Kinetics of Upd of Lead on Polycrystalline Silver and Gold. *Journal of Electroanalytical Chemistry* **2003**, *552*, 171–183. https://doi.org/10.1016/S0022-0728(03)00181-5.

(23) Holewinski, A.; Idrobo, J.-C.; Linic, S. High-Performance Ag–Co Alloy Catalysts for Electrochemical Oxygen Reduction. *Nat Chem* **2014**, *6* (9), 828–834. https://doi.org/10.1038/nchem.2032.

(24) Van Cleve, T.; Gibara, E.; Linic, S. Electrochemical Oxygen Reduction Reaction on Ag Nanoparticles of Different Shapes. *ChemCatChem* **2016**, *8* (1), 256–261. https://doi.org/10.1002/cctc.201500899.

(25) Green, C. L.; Kucernak, A. Determination of the Platinum and Ruthenium Surface Areas in Platinum−Ruthenium Alloy Electrocatalysts by Underpotential Deposition of Copper. I. Unsupported Catalysts. *J. Phys. Chem. B* **2002**, *106* (5), 1036–1047. https://doi.org/10.1021/jp0131931.

(26) Hachiya, T.; Honbo, H.; Itaya, K. Detailed Underpotential Deposition of Copper on Gold(III) in Aqueous Solutions. *Journal of Electroanalytical Chemistry and Interfacial Electrochemistry* **1991**, *315* (1), 275–291. https://doi.org/10.1016/0022-0728(91)80076-3.

(27) Mayrhofer, K. J. J.; Strmcnik, D.; Blizanac, B. B.; Stamenkovic, V.; Arenz, M.; Markovic, N. M. Measurement of Oxygen Reduction Activities via the Rotating Disc Electrode Method: From Pt Model Surfaces to Carbon-Supported High Surface Area Catalysts. *Electrochimica Acta* **2008**, *53* (7), 3181–3188. https://doi.org/10.1016/j.electacta.2007.11.057.

(28) Rudi, S.; Cui, C.; Gan, L.; Strasser, P. Comparative Study of the Electrocatalytically Active Surface Areas (ECSAs) of Pt Alloy Nanoparticles Evaluated by Hupd and CO-Stripping Voltammetry. *Electrocatalysis* **2014**, *5* (4), 408–418. https://doi.org/10.1007/s12678-014-0205-2.

(29) Moniri, S.; Van Cleve, T.; Linic, S. Pitfalls and Best Practices in Measurements of the Electrochemical Surface Area of Platinum-Based Nanostructured Electro-Catalysts. *Journal of Catalysis* **2017**, *345*, 1–10. https://doi.org/10.1016/j.jcat.2016.11.018.

(30) Binninger, T.; Fabbri, E.; Kötz, R.; Schmidt, T. J. Determination of the Electrochemically Active Surface Area of Metal-Oxide Supported Platinum Catalyst. *J. Electrochem. Soc.* **2014**, *161* (3), H121–H128. https://doi.org/10.1149/2.055403jes.

(31) Shao, M.; Odell, J. H.; Choi, S.-I.; Xia, Y. Electrochemical Surface Area Measurements of Platinum- and Palladium-Based Nanoparticles. *Electrochemistry Communications* **2013**, *31*, 46–48. https://doi.org/10.1016/j.elecom.2013.03.011.

(32) van der Vliet, D. F.; Wang, C.; Li, D.; Paulikas, A. P.; Greeley, J.; Rankin, R. B.; Strmcnik, D.; Tripkovic, D.; Markovic, N. M.; Stamenkovic, V. R. Unique Electrochemical Adsorption Properties of Pt-Skin Surfaces. *Angewandte Chemie International Edition* **2012**, *51* (13), 3139–3142. https://doi.org/10.1002/anie.201107668.

(33) Shao, M.; Chang, Q.; Dodelet, J.-P.; Chenitz, R. Recent Advances in Electrocatalysts for Oxygen Reduction Reaction. *Chem. Rev.* **2016**, *116* (6), 3594–3657. https://doi.org/10.1021/acs.chemrev.5b00462.

(34) Strmcnik, D.; Tripkovic, D.; van der Vliet, D.; Stamenkovic, V.; Marković, N. M. Adsorption of Hydrogen on Pt(111) and Pt(100) Surfaces and Its Role in the HOR. *Electrochemistry Communications* **2008**, *10* (10), 1602–1605. https://doi.org/10.1016/j.elecom.2008.08.019.

(35) Ochal, P.; Gomez de la Fuente, J. L.; Tsypkin, M.; Seland, F.; Sunde, S.; Muthuswamy, N.; Rønning, M.; Chen, D.; Garcia, S.; Alayoglu, S.; Eichhorn, B. CO Stripping as an

Electrochemical Tool for Characterization of Ru@Pt Core-Shell Catalysts. *Journal of Electroanalytical Chemistry* **2011**, *655* (2), 140–146. https://doi.org/10.1016/j.jelechem.2011.02.027.

(36) Vidaković, T.; Christov, M.; Sundmacher, K. The Use of CO Stripping for in Situ Fuel Cell Catalyst Characterization. *Electrochimica Acta* **2007**, *52* (18), 5606–5613. https://doi.org/10.1016/j.electacta.2006.12.057.

(37) Sugimoto, W.; Aoyama, K.; Kawaguchi, T.; Murakami, Y.; Takasu, Y. Kinetics of CH3OH Oxidation on PtRu/C Studied by Impedance and CO Stripping Voltammetry. *Journal of Electroanalytical Chemistry* **2005**, *576* (2), 215–221. https://doi.org/10.1016/j.jelechem.2004.10.018.

(38) Chatenet, M.; Soldo-Olivier, Y.; Chaînet, E.; Faure, R. Understanding CO-Stripping Mechanism from NiUPD/Pt(110) in View of the Measured Nickel Formal Partial Charge Number upon Underpotential Deposition on Platinum Surfaces in Sulphate Media. *Electrochimica Acta* **2007**, *53* (2), 369–376. https://doi.org/10.1016/j.electacta.2007.01.029.

Chapter 4 Microkinetic Modeling in Electrocatalysis

4.1 Introduction

In this chapter the role of microkinetic modeling for mechanistic analyses is presented. Several applications, shortcomings and recommendations are discussed along with a brief discussion on the role of in-situ spectroscopy to aid microkinetic modeling. This example is further expanded in the next chapter.

The critical challenge for fundamental research in heterogeneous catalysis and electrocatalysis is to discover atomistic-scale phenomena (e.g. elementary step mechanisms, adsorption energies, activation barriers for individual elementary steps, coverages of reaction intermediates) and relate them to macroscopic observables such as turnover frequencies (TOFs), reaction orders, product selectivities, and apparent activation energies for a given set of operating conditions (temperature, electrochemical potential, and pressures of reactants and products). An approach that has emerged as critical in connecting the atomic scale phenomena to macroscopic observables relies on microkinetic modeling. Microkinetic modeling in heterogeneous catalysis has its early origins in the works of Boudart[1] and Dumesic[2]. The field has grown in significance since the 1990s with the influential works of Norskov[3], Stoltze[4], Campbell[5,6], Scheffler[7] and many others.

Historically, "top-down" approaches, characterized by fitting empirical kinetic parameters to reactor data, for the purposes of optimizing chemical reactor designs, had been utilized for decades[8]. In these cases, the goal was to fit "kinetic" parameters which could capture the reactor behavior over a range of relevant operating conditions. Microkinetic analysis utilizes a "bottom-

up" approach wherein kinetic parameters are characteristic of elementary processes occurring on the surface of a catalyst. No assumptions are made about the rate-controlling steps, and instead the degree to which various elementary steps control the reaction arises organically out of the kinetic parameters and chemical species balances associated with a proposed set of elementary steps (although some simplified approximations can be used such as assuming a rate-determining step with all others quasi-equilibrated). Kinetic parameters for elementary steps may be estimated based on a combination of transition state theory, quantum chemical calculations, statistical thermodynamics, and experiments such as microcalorimetry or temperature programmed desorption (TPD)[8]. A number of reviews on microkinetic analysis have been written[8–14].

As discussed above, microkinetic (MK) modeling is used to relate assumptions about the elementary steps involved in a reaction to macroscopic experimental observables. Since microkinetic models must completely capture atomistic events on the surface to *exactly* reproduce macroscopic observables, it is reasonable to argue as Medford et al[15] did that microkinetic models are the "central representation of knowledge for catalysis." In this sense, MK modeling is a mathematical description of the aggregate knowledge about a catalytic reaction mechanism. As highlighted in reference[15], MK models are both explanative and predictive in their nature. They can be used to rationalize and explain observed experimental data on a material of interest, which yields knowledge about the mechanism, active sites, and kinetic parameters describing the elementary steps. Additionally, MK models can in principle be used (along with tools such as scaling relations and BEP relations[16–19]) to extrapolate outside of measured materials/catalysts and predict promising materials to be synthesized and tested for their catalytic activity. MK models can range in complexity from mean-field (MF) models, which consider only the average/mean properties of the system, to kinetic Monte Carlo (KMC) simulations, which attempt to explicitly

model every possible event (i.e. adsorption, diffusion, reaction, desorption) that can occur on a lattice representative of the catalyst surface using a stochastic procedure wherein the probability that a given event is executed is weighted by its respective rate constant[20]. MF models may be more reductionist and intuitive, while KMC can capture important atomistic-scale phenomena missed by the MF approximation (discussed in more detail below). The use of MK models has been growing steadily in recent years, which is indicated by the increasing number of open-source software/codes which can perform MK analysis to some degree, including CATMAP, Micki, CATKINAS, and others[21–23]. Similarly, a number of codes centered around KMC have also been developed including kmos, MonteCoffee, Zacros, and others[24–26]. While some codes such as CATMAP contain electrocatalysis implementations, most codes are specifically built around modeling thermochemical reactions.

While the use of microkinetic analysis in heterogenous electrocatalysis has historically been sparse relative to its use in thermocatalytic processes, it is worth noting that early efforts to model electrochemical hydrogen evolution and oxygen evolution reactions on platinum extend back to the 1950s with the pioneering works of Parsons, Bockris, and others[27–31]. Although the estimation of kinetic parameters for elementary electrochemical steps was severely limited, the general framework developed in early works proved useful in qualitatively understanding experimental data.

In recent years, MK modeling has been increasingly applied in studies of electrocatalytic reactions mainly due to advancements in the development of first principles calculations, which have allowed us to estimate the kinetic parameters for elementary electrochemical steps. Furthermore, the introduction of simple approximations such as the Computational Hydrogen Electrode (CHE) helped to make calculation of the potential-dependent energetics of relevant

electrocatalytic intermediates feasible[32,33]. The CHE approach can be used in a purely thermodynamic fashion, wherein a "limiting potential" is identified as the lowest overpotential where all elementary steps become thermodynamically downhill in free energy. While this does not account for activation barriers and other kinetic phenomena, this approach can still yield some predictive power and has allowed researchers to identify qualitative trends across materials (with reasonable agreement with experiment) for the rates of a number of electrocatalytic reactions of interest (such as oxygen reduction (ORR)[32], hydrogen evolution (HER)[34], and CO_2 reduction (CO_2RR)[33]). The CHE approach can also be used in conjunction with full MK models. If one can estimate the energy of a kinetic activation barrier for an elementary, one electron transfer step at a reference potential, then its value can be shifted with potential assuming a constant value of the electrochemical symmetry factor (β in eq. 1, typically assigned values of 0.5). The assumption of a constant symmetry factor is a key feature of the phenomenological Butler-Volmer theory of electrochemical kinetics, wherein each elementary rate constant may be written (according to transition state theory wherein nuclear tunneling effects are assumed to be negligible) as the following:

$$k = \frac{k_B T}{h} \exp\left[-\left(\Delta G_0^{\ddagger} - \beta F(E - E^0)\right)/RT\right] \quad (1)$$

where $\Delta G_0^{\ddagger}$ is the barrier at reference potential E^0 (generally the equilibrium potential of the reaction), F is Faraday's constant, β is the symmetry factor, and the other variables have their usual meaning. Marcus theory provides an alternative model of the potential dependence of the activation barrier, wherein a parabolic approximation to the free energy landscape of reactant and product gives a potential-dependent symmetry factor[35]:

$$\beta = \frac{1}{2} + \frac{F\eta}{2\lambda} \quad (2)$$

where η is the overpotential ($E - E^0$) and λ is the solvent reorganization energy. More recently, grand-canonical density functional theory (DFT) approaches have been developed, which allow for the calculation of potential-dependent energies of intermediates and transition-states from first-principles (i.e. no assumption of electrochemical symmetry factors and no assumption that the potential only affects the energy of proton/electron pairs, as in the CHE scheme)[36].

4.2 Developing MK Models in Thermal vs. Electrochemical Systems

The formalism of microkinetic modeling in electrocatalysis is similar to that in thermal catalysis. Rate constants for elementary reactions are estimated using transition-state theory and the framework of: (i) proposing elementary steps, (ii) applying species balances, and (iii) solving the model to steady-state (most often in the mean-field approximation). Kinetic Monte Carlo (KMC) simulations, which in principle can provide us with an atomistic resolution of elementary surface events, can also be similarly applied in both thermal- and electro-catalysis. While in thermal catalysis the apparent activation barrier captures the response of the overall reaction rate to the change in the driving force for the reaction (i.e., a temperature change), a similar kinetic signature for an electro-catalytic process is the Tafel slope. The Tafel slope (b), which is derived from the Butler-Volmer equation assuming a large enough overpotential that the reverse reaction rate is negligible, describes the sensitivity of the electrochemical reaction rate (current, i) to the applied electric potential, ΔE:

$$\Delta E = a + b \log i \tag{3}$$

Specifically, Tafel slopes tell us how much the applied potential needs to change to increase the reaction rate (current) by an order of magnitude. Tafel slopes are typically used to distinguish between various possible mechanisms, as different sets of elementary steps will often result in different Tafel slopes. It is worth noting that for non-adsorbing systems (molecular electro-

catalysis), in most situations the quantitative values of Tafel slopes are exclusively related to the symmetry factor of the rate controlling elementary step and the number of electrons involved in the formation of the intermediates participating in the rate controlling step[37,38]. It is critical to note, however, that for heterogeneous electrocatalytic reactions (i.e. most reactions of interest related to renewable energy conversion – HER/HOR, CO_2RR, OER/ORR, CO electro-oxidation (COOR) on various solid electrocatalysts) this assumption is not necessarily correct. Specifically, in these reactions the apparent (observed) Tafel slope is also a function of the coverage of the species present on the surface of the electrocatalyst under operating conditions[12,13,39]. The relationships between the value of the Tafel slope and surface coverage of reaction intermediates have been derived for many reactions[13]. Baz & Holewinski recently showed[40] that the apparent Tafel slope, apparent reaction orders and apparent activation energy of a general electrocatalytic mechanism can each be written as simple functions of Campbell's generalized degree of rate control (DRC)[5,41,42]. Since DRCs of stable intermediates are related to their fractional surface coverages[43,44], this formalism generally connects adsorbate coverages to Tafel slopes, reaction orders, and apparent activation energies.

Due to these inherent relationships between Tafel slope and the coverage of surface intermediates, different proposed mechanisms or rate determining steps may predict the same Tafel slope. One example is the oxygen reduction reaction on a Pt electrocatalyst, where the reaction mechanism that is commonly considered involves the following elementary steps (mechanism 1):

$$O_2 + H^+ + e^- + * \rightarrow OOH^* \quad (1)$$

$$OOH^* + * \rightarrow O^* + OH^* \quad (2)$$

$$O^* + H^+ + e^- \rightarrow OH^* \quad (3)$$

$$2(OH^* + H^+ + e^- \rightarrow H_2O + *) \quad (4)$$

As demonstrated by Holewinski & Linic[39] and adapted in Figure 4.1, calculated Tafel slopes for this mechanism are a function of the coverages of OH^* (and other species) on the surface of Pt.

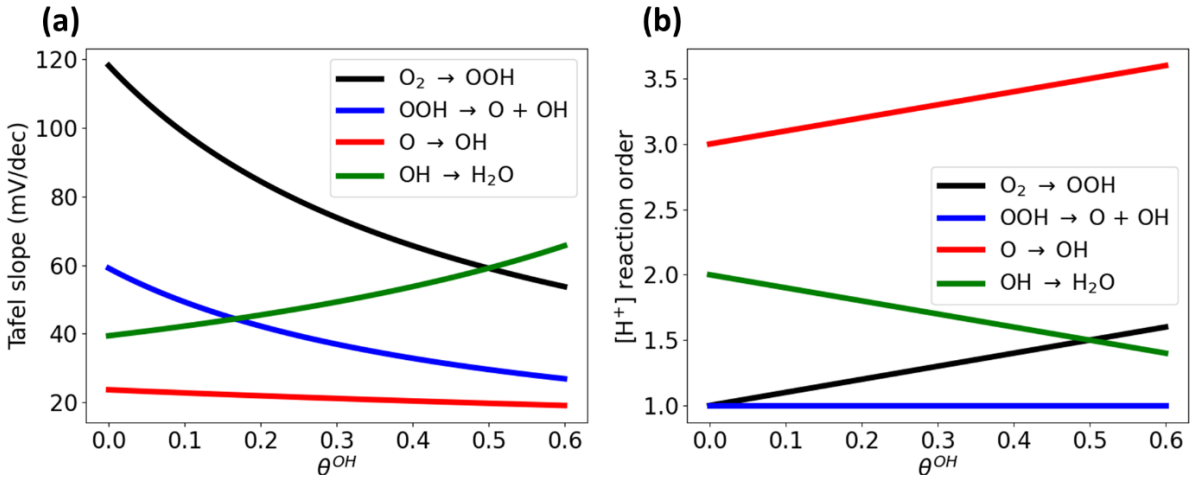


Figure 4.1(a) Calculated Tafel slopes and (b) reaction orders with respect to the concentration of $[H^+]$ for the ORR on Pt as a function of the OH^* coverage. Different lines correspond to the assumptions of different rate determining steps.

Therefore, without having some information about the surface coverage of intermediates under reaction conditions, it is difficult to use only the value of the Tafel slope to affirm or rule out a proposed mechanism for a heterogeneous electrocatalytic reaction. To be able to reliably deconvolute these coverage effects and point towards a most probable mechanism, knowledge of the character of the adsorption isotherm (e.g Langmiur, Frumkin, Temkin) for relevant adsorbates as well as the thermodynamic parameters associated with the adsorption equilibrium constants (i.e standard Gibbs free energies of adsorption) are also required. In the cases where there is a high degree of uncertainty about the surface coverage of intermediates and adsorption isotherms are not available, one can also use additional kinetic signatures to narrow down proposed mechanisms. For example, the apparent reaction orders (with respect to reactants) and the apparent activation energies contain complimentary information to the Tafel slope that can be used to identify mechanisms that are most consistent with experimental data[40].

In both thermal- and electro-catalysis, quantum chemical DFT calculations are commonly used to calculate electronic energies of intermediates/transition states in a vacuum environment. Corrections must be applied to convert these energies to Gibbs free energies. We note that Gibbs free energies of the intermediates and transition states are required to parametrize the elementary rate constants that are input to the MK model. For gas-phase species, the free energy corrections, mostly due to the entropic contributions to free energy, can be captured well by either tabulated values or they can be derived using statistical thermodynamics. Please see these excellent reviews and tutorials on estimating free energy corrections for thermochemical microkinetic models[8,10,21]. In electrocatalysis, the following major phenomena may additionally affect free energy corrections for elementary electrochemical reactions: (i) the effect of electric potential on the values of adsorption/activation energies (ii) solvent effects and their relationship to potential (iii) electric field effects and (iv) ion/electrolyte effects.

The effect of potential has been implemented within quantum chemical calculations (mainly within DFT) in recent years through the development of approaches to either approximate constant electrode potential within systems of fixed particle (electron) number (e.g. double-reference scheme[45], unit cell extrapolation[46], capacitive energy compensation[47], self-consistent charge injection[48,49]) or using true grand canonical codes that adjust the electron number to the given potential[36,50,51]. Solvent effects have also been dealt with to varying degrees. In order of increasing accuracy/decreasing computational efficiency these involve continuum implicit solvation models, static explicit solvation models, micro-solvation models combining both explicit/implicit approximations, and *ab initio* molecular dynamics simulations which allow for robust sampling and statistical averaging of solvent fluctuations over longer time scales[51,52]. The balancing of computational accuracy with efficiency of solvation models is currently an active field of research.

It is also worth noting that the electrode/electrolyte interface inherently produces strong electric fields when operating under conditions far away from the potential of zero charge (PZC) on a material/electrolyte interface of interest[53]. The surface charge also frequently has a strong pH dependence, as the establishment of a given potential on the reversible hydrogen electrode (RHE) scale can correspond to very different potentials vs. PZC for different pH conditions[54,55]. This variation of the electric field can alter the binding energies of chemical intermediates and transition states and can be roughly captured with simple models involving the dipole moments and polarizabilities of the relevant species[56]. Less understood, but also likely very significant, is the effect of electric fields on the solvent molecules (particularly polar solvent molecules such as water) at the electrode/electrolyte interface. Fields may impose preferential orientation of solvent molecules which can affect the reorganization energies associated with charge transfer as well as the solvation energies of relevant adsorbates[57,58]. For example, solvent dynamics and potential dependent interfacial interactions and ordering between H_2O and its derivatives (H, O, OH) have been identified by ab-initio thermodynamics, molecular dynamics, and in-operando spectroscopy [59–61] and have been hypothesized to play a significant role in electrocatalyst activity. Specifically adsorbed ions present in the electrolyte can also affect the local electric fields at the interface, as has been studied for cations during the CO_2 reduction reaction[62]. Some electrocatalytic reactions further exhibit dramatic pH dependences (beyond what can be expected from proton or hydroxyl reaction orders) – for example the specific activity of the hydrogen evolution/oxidation reaction (HER/HOR) on Pt decreases by two orders of magnitude from pH = 1 to pH = 13 – the origins of this pH effect are still debated[63]. A comprehensive formulation of free energy corrections which can capture each of these complexities and non-idealities inherent to the electrode/electrolyte interface will be necessary in order for MK models to be accurately parametrized.

Finally, electrochemical symmetry factors for elementary reactions, which are critical in the parameterization of the rate equations, may also change as a function of potential (e.g. as predicted by Marcus theory[35]). This can have dramatic impacts on the calculated values of the kinetic signatures of the reaction (i.e., the Tafel slopes, apparent reaction orders, etc.) as the potential is varied[64]. MK models of electrocatalytic reactions will need to incorporate each of these non-idealities to provide useful information about reaction mechanisms and ultimately lead to the prediction and discovery of improved electrocatalytic materials.

4.3 Predictive Power and Uncertainties Associated with MK Modeling

A cursory literature review suggests that a majority of MK modeling studies of catalytic reactions employ kinetic parameters for elementary steps estimated based on ab-initio (most often DFT) calculations. Due in part to the inherent uncertainty associated with the ab-initio methods used to estimate the key energetic parameters, such as adsorption enthalpies and activation barriers of elementary steps, the ab-initio microkinetic models usually do not quantitatively "fit" experimental measurements of TOFs and apparent activation energies without some parameter adjustment[52,65]. Even a "small" error in an activation barrier of a kinetically relevant elementary step can correspond to large differences in predicted rate constants—a typical 0.2 eV error for an elementary step DFT barrier calculation would correspond to a roughly three orders of magnitude difference in the rate constant at room temperature due to the exponential impact of the barrier. There have been attempts to rigorously capture uncertainties in DFT-calculated energetics and propagate them through microkinetic models—for example in the ammonia synthesis reaction[66] — in order to better understand the uncertainties in the predicted rates/TOFs. In Ref [[66]] it was found that due to correlation (and the resulting cancellation) of errors in DFT calculations across different transition metal surfaces, activity trends among materials were predicted with greater

certainty than absolute rates. In a similar vein, some recent works have applied Bayesian Parameter Estimation (BPE) as a means to incorporate the prior uncertainties in adsorption energies and activation barriers across several DFT functionals to aid in selecting the most probable active site for the water-gas-shift reaction on Pt/TiO_2[67]. It was found that the CO-promoted redox mechanism on the edge-interface site was the most likely model to explain the experimental data given the prior first-principles estimates of the parameters. Uncertainty quantification, specifically the propagation of uncertainties inherent to DFT functionals through MK models, has grown in popularity in recent years and is expected to continue to grow as microkinetic modeling becomes increasingly utilized[68].

In addition to the uncertainty related to computational accuracy, another source of error arises from the assumptions of the microkinetic model itself. Mean-field (MF) models are the most used in MK modeling. The MF approximation assumes that adsorbed species have randomized locations (for example, due to rapid surface diffusion) and thus no spatial correlations or long-range order exist among the species on the surface; the rates are proportional only to the total coverages of respective species. In other words, MF models are based entirely on the average/mean properties of the system. MF models can be adapted to also account for effective adsorbate-adsorbate interactions wherein the energetics of intermediates are modeled as a function of the total coverages of the relevant adsorbates. Recent works have stressed the importance of developing coverage self-consistent MK models wherein the DFT energetics used to parametrize the model correspond to the same coverages that are predicted by the MK model (sometimes requiring an iterative procedure to achieve consistency)[52]. MF models can also account for multiple site types, albeit with a modest degree of resolution. For example, nanoparticles can be modeled as a combination of terrace sites and edge/step sites. Typically, (111) and (100) facets are used to

capture the terrace sites while (211) steps are used as an approximation of the steps/edge sites[69,70]. The total rate will then be the sum of the (site-normalized) rates on each of the respective sites. If one site type is significantly more active than another, then the observed rate will be dominated by the rate on that site type. Interactions between the site types (e.g. bifunctional coupling) can also be approximated in MF models, although this approaches the limit of resolution granted by the MF approximations[71–73]. Since MF models are limited in their accuracy, they should be used with caution. Results should be interpreted only qualitatively—i.e., quantitative agreement with experiment is unlikely given the model assumptions, unless some degree of parameter adjustment is applied and/or key aspects of the mechanism are well-established by other methods such as spectroscopy.

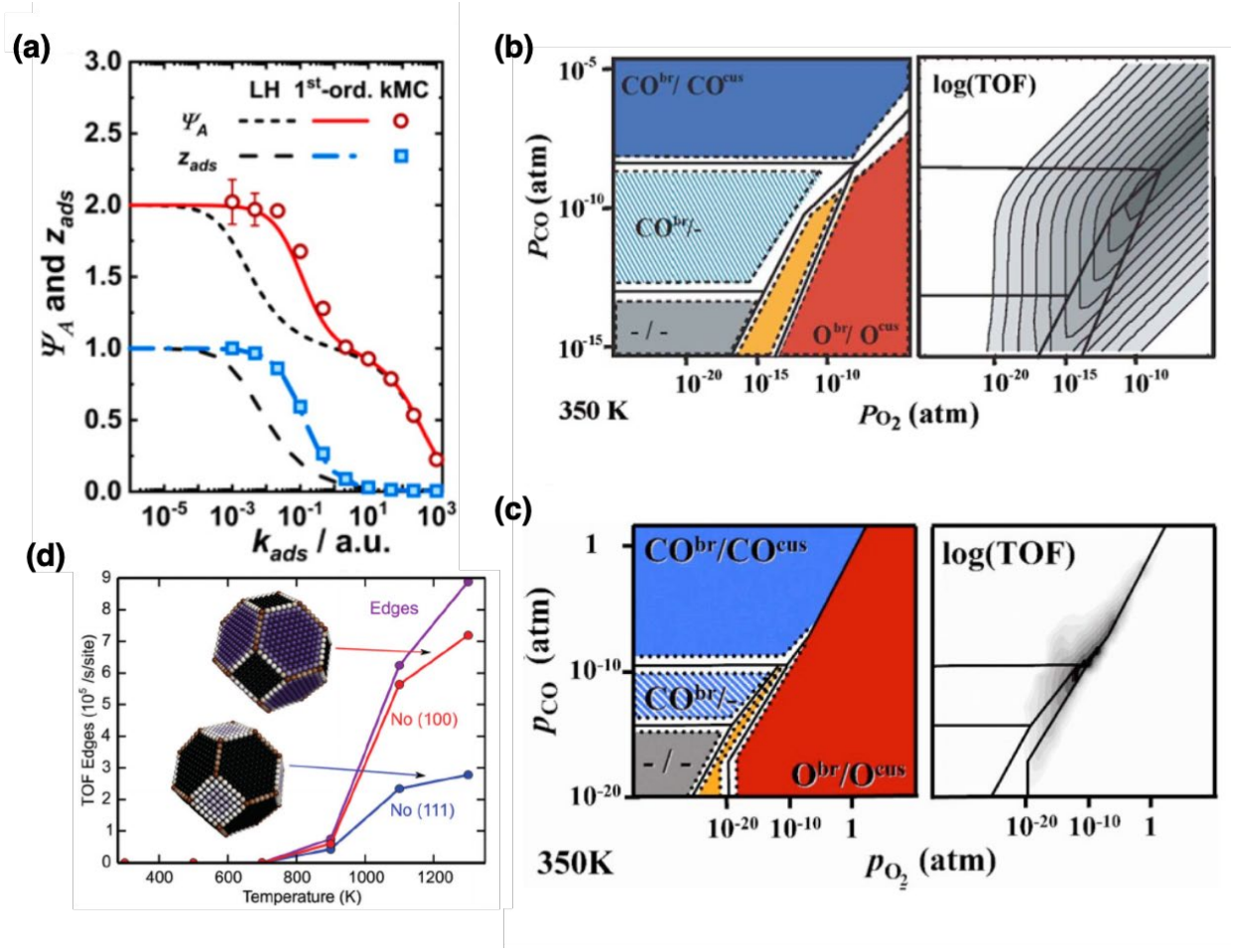


Figure 4.2 (a) Reaction order (Ψ_A) and reversibility (z_{ads} defined as: $\left(\frac{r_{-i,[j]}}{r_{i,[j]}}\right)$) of a simple $A + A \leftrightarrow A_2$ reaction with respect to the rate constant (k_{ads}) for the adsorption of A calculated with Langmuir Hinshelwood (0^{th}-order), 1^{st}-order and KMC models. (b) Comparison of steady-state surface coverages and TOFs for CO-oxidation on RuO_2(110) calculated with phenomenological kinetics and (c) with KMC. (d) Steady-state TOFs at the edges of a 5.2 nm truncated octahedron calculated with KMC for CO-oxidation with and without neighboring (100) and (111) facets.

Another set of uncertainties associated with conventional MK modelling was discussed recently by Razdan and Bhan who showed that simple approximations typically used in MF models such as the random distribution of adsorbates on the catalytic surface (i.e. the Hinshelwood approximation) fail to properly account for site ensemble statistics (Figure 4.2a)—for example, in the simple case of two adsorbates coupling, adjacent pairs may react and desorb more rapidly than diffusion can randomize the locations, meaning that the MF approximation will overestimate the number of pairs in position to react. This would preclude quantitative agreement between the

model and experiment even if the estimates of the energetic parameters were exact. This finding is in line with past work from Reuter and co-workers (Figure 4.2b-c) who also showed that phenomenological (i.e. mean field without statistical corrective factors) MK models cannot reproduce the same results from KMC simulations given the same energetic parameter inputs, even for the case of zero adsorbate-adsorbate interactions[74]. They proposed that the discrepancy was due to errors in the site statistics inherent to MF models. This has implications for parameter estimation of standard mean-field MK models – while the "fitted" parameters may possess explanatory power and thus may be useful for predictive purposes, they will not be accurate representations of the true physical phenomena at the atomistic level if the model is wrong (i.e., in site counting) to some degree.

In some cases, adsorbates can adopt long range ordering which is also related to the distribution of site types on a real surface as well as the interactions between adsorbates. MF models fail to describe these phenomena and capturing them requires the use of kinetic Monte Carlo (KMC) simulations. KMC simulations have been used to study the qualitative features of many electrocatalytic reactions such as the CO electro-oxidation reaction on Pt and PtRu[75–77]. In KMC, the rate constants may be similarly sourced from DFT calculations, but typically more calculations are required to estimate the parameters since adsorbate-adsorbate interactions need to be taken into account[26]. While the KMC approach is significantly more computationally expensive than the MF approach, it has been shown that it can capture important phenomena that is missed by MF models. For example, Gronbeck et al showed through KMC modeling of nanoparticles that the site assembly, i.e. the specific spatial and energetic distribution of sites on a nanoparticle (Figure 4.2d), produces activities that cannot be predicted by just a linear combination of the separate sites[78]. In other words, the connections/interplay between the different sites yield emergent phenomena

relevant to catalytic activity that cannot be captured without the full KMC simulation. As the accuracy of first-principles parameter estimation in electrocatalysis increases, we expect the use of KMC to increase as well, which will undoubtedly result in improved mechanistic understanding of many important electrocatalytic processes. For electrochemical reactions specifically, comparison to single-crystal voltammetric experiments can serve as a powerful tool for testing the veracity of the mean-field approximation (as opposed to full KMC simulation), since these experiments reduce the complexity of the system down to a single site type[79]. For example, Garcia-Araez et al found that the mean-field approximation cannot reproduce the voltammetric features of bromide adsorption on Pt(100) due to its inability to capture the effects of short-range adsorbate interactions/local adsorbate ordering[80]. For other electrochemical reactions, such as CO electro-oxidation, chronoamperometric stripping transients on Pt(111) are well-captured by a mean-field model[81], highlighting that the utility of the mean-field approximation is highly reaction-specific.

Given the various limitations in MK modeling, Mavrikakis and co-workers recently proposed a procedure to test whether a MK model possesses quantitative explanatory power for a reaction on a material of interest[82]. This procedure involves meeting three criteria: (i) Are experimental observables such as reaction orders and apparent barriers reproduced by the MK model? (ii) Can adjustments in the DFT-estimated energetic parameters reproduce observables within the expected error/uncertainty of DFT (0.1-0.2 eV)? (iii) Are the coverages predicted by the MK model under the operating conditions consistent with the coverages utilized in the DFT calculations? If all three of these criteria are met, then the model (i.e. the elementary steps, energetic parameters, and active site designation) is considered sufficiently explanatory of the reaction on the material being studied. If these criteria are not met, then the model must be adjusted (either in the elementary step mechanism or designation of the active site) or the coverages must be adjusted to achieve self-

consistency. In addition to these kinds of parameter adjustments, others have also proposed utilizing BPE to estimate parameters of MK models, which can account for the prior knowledge of energetic parameters from other experiments or first-principles calculations[83]. Both of these approaches are promising, but they have been under-utilized in electrocatalysis except for some select cases[84].

4.4 Spectroscopy as Complementary Tool

Outlined above are some of the critical issues that need to be considered when using MK modeling to unearth elementary step mechanisms of electrochemical reactions. Due to the above-mentioned complexities and uncertainties, it is often not possible to use exclusively MK modeling to affirm a particular mechanism or to uncover all molecular features of the mechanism. If possible, it is desirable to use in-situ spectroscopy as a powerful complimentary tool to MK modeling.

To illustrate this point, we turn to the example of the oxygen reduction reaction on Pt surfaces, for which the proposed mechanistic steps were shown in mechanism 1 above. MK modeling studies that included assumptions of different rate limiting steps, as well as the surface intermediate coverages derived from DFT ab-initio thermodynamic studies and experimentally measured adsorption/desorption isotherms, have shown that this reaction operates in two different kinetic regimes as a function of the Pt electrode potential[39,85]. At high voltage, the reaction rate is controlled by the presence of a network of water and OH on the surface of the Pt electrocatalyst that covers the active sites (step 4 in the mechanism 1), and by the slow rates of O_2 activation with a proton/electron pair to form OH* and O* (steps 1 and 2). It was also suggested based on MK modeling that at lower voltages (far from equilibrium) the Pt surface is relatively clean, and the rate is controlled by the addition of a proton/electron pair to O_2 and its subsequent conversion to OH* and O* (steps 1 or 2). The information that could not be obtained by comparing the results

of MK modeling to the experimentally measured kinetic signatures of ORR on Pt (Tafel slope, reaction orders, etc) is which of steps 1 or 2 is kinetically relevant under a given electrode potential. To answer this question and provide more evidence for the above proposed reaction mechanism (steps 1 to 4), Chapter 5 details an in-operando Raman spectroscopic study, attempting to identify the intermediates present on the surface of a working Pt electrode as a function of electric potential[61]. It should be noted, that obtaining direct spectroscopic evidence, in the form of electronic or vibrational spectra of surface intermediates at electrified interfaces is rather challenging. The experimental difficulties are the consequence of (i) the presence of the interfacial electric field effects which change as the electrode potential changes (ii) the presence of water molecules whose interfacial surface orientation changes as a function of potential, (iii) the existence of electrolyte ions which further complicate the mechanism[50,86–90] and (iv) a general lack of surface sensitivity of many spectroscopic techniques, making it challenging to separate the spectroscopic signals associated with surface reaction intermediates from those associated with the water-based electrolyte[91].

In addition to Raman, several different in-situ spectroscopic techniques have been developed to probe the adsorbed species occurring on electrified electrocatalyst surfaces. These include in-situ attenuated total reflectance surface enhanced infrared absorption spectroscopy (ATR-SEIRAS) which has been used to probe intermediates at electrocatalyst surfaces for electrochemical reactions such as ORR/OER and HOR/HER[92–96]. Another technique that shows promise is shell-isolated nanoparticle-enhanced Raman spectroscopy or SHINERS[97] which utilizes Au nanoparticles wrapped in an inert silica shell which separates the Au from the electrolyte. As these core-shell nanoparticles approach the electrocatalyst of interest, the Raman signal at the electrocatalyst surface is greatly enhanced due to the increased electric fields around the Au@SiO_2

nanoparticles. This technique has been used to probe several electrochemical reactions such as ORR and CO reduction[98–100].

4.5 Conclusions

As a tool, MK modeling can aid in the analysis of electrochemical reaction mechanisms explaining observed Tafel slopes, reaction orders, and activation energies. This analysis sheds light on the reaction mechanism, which enables the rational design of electrocatalysts for optimal catalytic activity. MK modeling formalism was presented with a focus on the role of advanced methods and complimentary tools to overcome the limitations and inaccuracies of MK modeling. It was demonstrated that to be reliable, MK modeling on electrocatalysts must address several non-idealities such as the electrochemical potential, solvent dynamics, and interfacial structures. Additionally, commonly used approximations such as the mean-field approximation have been shown to break down even for simple systems and should only be used for qualitative analysis. Methods such as KMC, grand canonical DFT, and Bayesian inference allow us to address some of these limitations. Finally, in-situ/in-operando spectroscopy is recommended as a powerful complimentary tool to reveal vibrational fingerprints of abundant reaction intermediates and equilibrium structures to boost accuracy and confidence in the model by eliminating or uncovering reaction pathways.

4.6 References

(1) White, R. R.; Fink, C. G.; Boudart, M. Kinetics on Ideal and Real Surfaces. **1956**, *553* (1948), 1–3.

(2) Dumesic, J. A.; Rudd, D. F.; Aparicio, L. M.; Rekoske, J. E.; Trevino, A. A. *The Microkinetics of Heterogeneous Catalysis*; Wiley, 1993.

(3) Honkala, K.; Hellman, A.; Remediakis, I. N.; Logadottir, A.; Carlsson, A.; Dahl, S.; Christensen, C. H.; Norskov, J. K. Ammonia Synthesis from First-Principles Calculations. *Science* **2005**, *307* (January), 555–558.

(4) Lynggaard, H.; Andreasen, A.; Stegelmann, C.; Stoltze, P. Analysis of Simple Kinetic Models in Heterogeneous Catalysis. *Progress in Surface Science* **2004**, *77* (3–4), 71–137. https://doi.org/10.1016/j.progsurf.2004.09.001.

(5) Campbell, C. T. Finding the Rate-Determining Step in a Mechanism: Comparing DeDonder Relations with The "Degree of Rate Control." *Journal of Catalysis* **2001**, *204* (2), 520–524. https://doi.org/10.1006/jcat.2001.3396.

(6) Campbell, C. T. Micro- and Macro-Kinteitcs: Their Relationship in Heterogeneous Catalysis. *Topics in Catalysis (Proc. of Topsoe/Nielsen Symp., 1993)* **1994**, *1*, 353–366.

(7) Reuter, K.; Scheffler, M. First-Principles Kinetic Monte Carlo Simulations for Heterogeneous Catalysis: Application to the CO Oxidation at RuO2 (110). *Physical Review B - Condensed Matter and Materials Physics* **2006**, *73* (4), 1–17. https://doi.org/10.1103/PhysRevB.73.045433.

(8) Motagamwala, A. H.; Dumesic, J. A. Microkinetic Modeling: A Tool for Rational Catalyst Design. *Chem. Rev.* **2021**, *121* (2), 1049–1076. https://doi.org/10.1021/acs.chemrev.0c00394.

(9) Wittreich, G. R.; Alexopoulos, K.; Vlachos, D. G. Microkinetic Modeling of Surface Catalysis. *Handbook of Materials Modeling* **2018**, 1–28. https://doi.org/10.1007/978-3-319-50257-1_5-1.

(10) Motagamwala, A. H.; Ball, M. R.; Dumesic, J. A. Microkinetic Analysis and Scaling Relations for Catalyst Design. **2018**, No. April, 1–38. https://doi.org/10.1146/annurev-chembioeng-060817-084103.

(11) Salciccioli, M.; Stamatakis, M.; Caratzoulas, S.; Vlachos, D. G. A Review of Multiscale Modeling of Metal-Catalyzed Reactions: Mechanism Development for Complexity and Emergent Behavior. *Chemical Engineering Science* **2011**, *66* (19), 4319–4355. https://doi.org/10.1016/j.ces.2011.05.050.

(12) Marshall, A. T. Using Microkinetic Models to Understand Electrocatalytic Reactions. *Current Opinion in Electrochemistry* **2018**, *7* (5), 75–80. https://doi.org/10.1016/j.coelec.2017.10.024.

(13) Shinagawa, T.; Garcia-Esparza, A. T.; Takanabe, K. Insight on Tafel Slopes from a Microkinetic Analysis of Aqueous Electrocatalysis for Energy Conversion. *Scientific Reports* **2015**, *5* (1), 13801. https://doi.org/10.1038/srep13801.

(14) Fang, Y.; Liu, Z. Tafel Kinetics of Electrocatalytic Reactions: From Experiment to First-Principles. *ACS Catalysis* **2014**, *4*, 4364–4376. https://doi.org/10.1021/cs501312v.

(15) Medford, A. J.; Kunz, M. R.; Ewing, S. M.; Borders, T.; Fushimi, R. Extracting Knowledge from Data through Catalysis Informatics. *ACS Catalysis* **2018**, *8* (8), 7403–7429. https://doi.org/10.1021/acscatal.8b01708.

(16) Nørskov, J. K.; Bligaard, T.; Logadottir, A.; Bahn, S.; Hansen, L. B.; Bollinger, M.; Bengaard, H.; Hammer, B.; Sljivancanin, Z.; Mavrikakis, M.; Xu, Y.; Dahl, S.; Jacobsen, C. J. H. Universality in Heterogeneous Catalysis. *Journal of Catalysis* **2002**, *209* (2), 275–278. https://doi.org/10.1006/jcat.2002.3615.

(17) S.Wang, V. P., V. Tripkovic, J. Kleis, J. G. Howalt, E. Skulason, E. M. Fernandez, B. Hvolbaek, G. Jones, A. Toftelund, H. Falsig, M. Bjorketun, F. Studt, F. Abild-Pederson, J. Rossmeisl, J. K. Norskov, T. Bligaard. Universal Transition State Scaling Relations for (de)Hydrogenation over Transition Metals. *Phys. Chem. Chem. Phys.* **2011**, *13*, 20760–20765. https://doi.org/10.1039/c1cp20547a.

(18) Vojvodic, A.; Calle-Vallejo, F.; Guo, W.; Wang, S.; Toftelund, A.; Studt, F.; Martínez, J. I.; Shen, J.; Man, I. C.; Rossmeisl, J.; Bligaard, T.; Nrskov, J. K.; Abild-Pedersen, F. On the Behavior of Brønsted-Evans-Polanyi Relations for Transition Metal Oxides. *Journal of Chemical Physics* **2011**, *134* (24). https://doi.org/10.1063/1.3602323.

(19) Montemore, M. M.; Medlin, J. W. Scaling Relations between Adsorption Energies for Computational Screening and Design of Catalysts. *Catal. Sci. Technol.* **2014**, *4* (11), 3748–3761. https://doi.org/10.1039/C4CY00335G.

(20) Andersen, M.; Panosetti, C.; Reuter, K. A Practical Guide to Surface Kinetic Monte Carlo Simulations. *Frontiers in Chemistry* **2019**, *7* (APR), 1–24. https://doi.org/10.3389/fchem.2019.00202.

(21) Medford, A. J.; Shi, C.; Hoffmann, M. J.; Lausche, A. C.; Fitzgibbon, S. R.; Bligaard, T.; Nørskov, J. K. CatMAP: A Software Package for Descriptor-Based Microkinetic Mapping of Catalytic Trends. *Catalysis Letters* **2015**, *145* (3), 794–807. https://doi.org/10.1007/s10562-015-1495-6.

(22) Chen, J.; Jia, M.; Hu, P.; Wang, H. CATKINAS: A Large-Scale Catalytic Microkinetic Analysis Software for Mechanism Auto-Analysis and Catalyst Screening. *Journal of Computational Chemistry* **2021**, *42* (5), 379–391. https://doi.org/10.1002/jcc.26464.

(23) Hermes, E. D.; Janes, A. N.; Schmidt, J. R. Micki: A Python-Based Object-Oriented Microkinetic Modeling Code. *Journal of Chemical Physics* **2019**, *151* (1). https://doi.org/10.1063/1.5109116.

(24) Hoffmann, M. J.; Matera, S.; Reuter, K. Kmos: A Lattice Kinetic Monte Carlo Framework. *Computer Physics Communications* **2014**, *185* (7), 2138–2150. https://doi.org/10.1016/j.cpc.2014.04.003.

(25) Jørgensen, M.; Grönbeck, H. MonteCoffee: A Programmable Kinetic Monte Carlo Framework. *Journal of Chemical Physics* **2018**, *149* (11). https://doi.org/10.1063/1.5046635.

(26) Stamatakis, M.; Vlachos, D. G. A Graph-Theoretical Kinetic Monte Carlo Framework for on-Lattice Chemical Kinetics. *Journal of Chemical Physics* **2011**, *134* (21). https://doi.org/10.1063/1.3596751.

(27) Parsons, R. The Rate of Electrolytic Hydrogen Evolution and the Heat of Adsorption of Hydrogen. *Transactions of the Faraday Society* **1958**, *54*, 1053–1063.

(28) Parsons, R. Hydrogen Evolution on Platinum Electrodes: The Heats of Activation for the Component Reactions. *Transactions of the Faraday Society* **1960**, *56*, 1340–1350.

(29) Bockris, J. O. M. Kinetics of Activation Controlled Consecutive Electrochemical Reactions: Anodic Evolution of Oxygen. *The Journal of Chemical Physics* **1956**, *24* (4), 817–827. https://doi.org/10.1063/1.1742616.

(30) Bockris, J. O.; Potter, E. C. The Mechanism of the Cathodic Hydrogen Evolution Reaction. *Journal of The Electrochemical Society* **1952**, *99* (4), 169–169. https://doi.org/10.1149/1.2779692.

(31) Conway, B. E.; Bockris, J. O. Electrolytic Hydrogen Evolution Kinetics and Its Relation to the Electronic and Adsorptive Properties of the Metal. *The Journal of Chemical Physics* **1957**, *26* (3), 532–541.

(32) Nørskov, J. K.; Rossmeisl, J.; Logadottir, A.; Lindqvist, L.; Kitchin, J. R.; Bligaard, T.; Jonsson, H. Origin of the Overpotential for Oxygen Reduction at a Fuel Cell Cathode. *J. Phys. Chem. B* **2004**, *108*, 17886–17892. https://doi.org/10.1021/jp047349j.

(33) Peterson, A. A.; Abild-Pedersen, F.; Studt, F.; Rossmeisl, J.; Nørskov, J. K. How Copper Catalyzes the Electroreduction of Carbon Dioxide into Hydrocarbon Fuels. *Energy & Environmental Science* **2010**, *3* (9), 1311–1315. https://doi.org/10.1039/c0ee00071j.

(34) Nørskov, J. K.; Bligaard, T.; Logadottir, A.; Kitchin, J. R.; Chen, J. G.; Pandelov, S.; Stimming, U. Trends in the Exchange Current for Hydrogen Evolution. *Journal of The Electrochemical Society* **2005**, *152* (3), J23–J23. https://doi.org/10.1149/1.1856988.

(35) Marcus, R. A. On the Theory of Oxidation-Reduction Reactions Involving Electron Transfer. I. *The Journal of Chemical Physics* **1956**, *24* (5), 966–978. https://doi.org/10.1063/1.1742723.

(36) Sundararaman, R.; Letchworth-Weaver, K.; Schwarz, K. A.; Gunceler, D.; Ozhabes, Y.; Arias, T. A. JDFTx: Software for Joint Density-Functional Theory. *SoftwareX* **2017**, *6*, 278–284. https://doi.org/10.1016/j.softx.2017.10.006.

(37) Bard, A. J.; Faulkner, L. R. *Electrochemical Methods: Fundamentals and Applications*, Second.; John Wiley & Sons, Inc., 2001.

(38) Guidelli, R.; Compton, R. G.; Feliu, J. M.; Gileadi, E.; Lipkowski, J.; Schmickler, W.; Trasatti, S. Defining the Transfer Coefficient in Electrochemistry: An Assessment

(IUPAC Technical Report). *Pure and Applied Chemistry* **2014**, *86* (2), 245–258. https://doi.org/10.1515/pac-2014-5026.

(39) Holewinski, A.; Linic, S. Elementary Mechanisms in Electrocatalysis: Revisiting the ORR Tafel Slope. *J. Electrochem. Soc.* **2012**, *159* (11), H864–H870. https://doi.org/10.1149/2.022211jes.

(40) Baz, A.; Holewinski, A. Predicting Macro-Kinetic Observables with the Generalized Degree of Rate Control in Electrocatalysis. *Journal of Catalysis* **2021**. https://doi.org/10.1016/j.jcat.2021.03.014.

(41) Campbell, C. T. The Degree of Rate Control : A Powerful Tool for Catalysis Research. *ACS Catalysis* **2017**, *7*, 2770–2779. https://doi.org/10.1021/acscatal.7b00115.

(42) Stegelmann, C.; Andreasen, A.; Campbell, C. T. Degree of Rate Control: How Much the Energies of Intermediates and Transition States Control Rates (Journal of the American Chemical Society (2009), 131, (8077-8082)). *Journal of the American Chemical Society* **2009**, *131* (37), 13563–13563. https://doi.org/10.1021/ja9065199.

(43) Mao, Z.; Campbell, C. T. The Degree of Rate Control of Catalyst-Bound Intermediates in Catalytic Reaction Mechanisms: Relationship to Site Coverage. *Journal of Catalysis* **2020**, *381*, 53–62. https://doi.org/10.1016/j.jcat.2019.09.044.

(44) Foley, B. L.; Bhan, A. Degree of Rate Control and De Donder Relations – An Interpretation Based on Transition State Theory. *Journal of Catalysis* **2020**, *384*, 231–251. https://doi.org/10.1016/j.jcat.2020.02.008.

(45) Taylor, C. D.; Wasileski, S. A.; Filhol, J. S.; Neurock, M. First Principles Reaction Modeling of the Electrochemical Interface: Consideration and Calculation of a Tunable Surface Potential from Atomic and Electronic Structure. *Physical Review B - Condensed Matter and Materials Physics* **2006**, *73* (16), 1–16. https://doi.org/10.1103/PhysRevB.73.165402.

(46) Skulason, E.; Tripkovic, V.; Bjorketun, M. E.; Gudmundsdottir, S.; Karlberg, G.; Rossmeisl, J.; Bligaard, T.; Jonsson, H.; Norskov, J. K. Modeling the Electrochemical Hydrogen Oxidation and Evolution Reactions on the Basis of Density Functional Theory Calculations (Vol 114, Pg 18182, 2010). *Journal of Physical Chemistry C* **2010**, *114*, 18182–18197. https://doi.org/10.1021/jp110913n.

(47) Chan, K.; Nørskov, J. K. Electrochemical Barriers Made Simple. *Journal of Physical Chemistry Letters* **2015**, *6* (14), 2663–2668. https://doi.org/10.1021/acs.jpclett.5b01043.

(48) Goodpaster, J. D.; Bell, A. T.; Head-Gordon, M. Identification of Possible Pathways for C–C Bond Formation during Electrochemical Reduction of CO2 : New Theoretical Insights from an Improved Electrochemical Model. *The Journal of Physical Chemistry Letters* **2016**, *7* (100), 1471–1477. https://doi.org/10.1021/acs.jpclett.6b00358.

(49) Lindgren, P.; Kastlunger, G.; Peterson, A. A. A Challenge to the G ∼0 Interpretation of Hydrogen Evolution. *ACS Catalysis* **2020**, *10* (1), 121–128. https://doi.org/10.1021/acscatal.9b02799.

(50) Sundararaman, R.; Goddard, W. A.; Arias, T. A. Grand Canonical Electronic Density-Functional Theory: Algorithms and Applications to Electrochemistry. *The Journal of Chemical Physics* **2017**, *146* (11), 114104. https://doi.org/10.1063/1.4978411.

(51) Schwarz, K.; Sundararaman, R. The Electrochemical Interface in First-Principles Calculations. *Surface Science Reports* **2020**, *75* (2), 100492–100492. https://doi.org/10.1016/j.surfrep.2020.100492.

(52) Chen, B. W. J.; Xu, L.; Mavrikakis, M. Computational Methods in Heterogeneous Catalysis. *Chemical Reviews* **2021**, *121* (2), 1007–1048. https://doi.org/10.1021/acs.chemrev.0c01060.

(53) Zeradjanin, A. R.; Polymeros, G.; Toparli, C.; Ledendecker, M.; Hodnik, N.; Erbe, A.; Rohwerder, M.; La Mantia, F. What Is the Trigger for the Hydrogen Evolution Reaction? - Towards Electrocatalysis beyond the Sabatier Principle. *Physical Chemistry Chemical Physics* **2020**, *22* (16), 8768–8780. https://doi.org/10.1039/d0cp01108h.

(54) Gileadi, E.; Argade, S. D.; Bockris, J. O. The Potential of Zero Charge of Platinum and Its PH Dependence. *J. Phys. Chem.* **1966**, *70* (6), 2044–2046. https://doi.org/10.1021/j100878a501.

(55) Rizo, R.; Sitta, E.; Herrero, E.; Climent, V.; Feliu, J. M. Towards the Understanding of the Interfacial PH Scale at Pt(111) Electrodes. *Electrochimica Acta* **2015**, *162*, 138–145. https://doi.org/10.1016/j.electacta.2015.01.069.

(56) Dauenhauer, P. J.; Shetty, M.; Ardagh, M. A.; Pang, Y.; Abdelrahman, O. A. Electric-Field-Assisted Modulation of Surface Thermochemistry. *ACS Catalysis* **2020**, *10* (21), 12867–12880. https://doi.org/10.1021/acscatal.0c02124.

(57) Ledezma-Yanez, I.; Wallace, W. D. Z.; Sebastián-Pascual, P.; Climent, V.; Feliu, J. M.; Koper, M. T. M. Interfacial Water Reorganization as a PH-Dependent Descriptor of the Hydrogen Evolution Rate on Platinum Electrodes. *Nature Energy* **2017**, *2* (4), 1–7. https://doi.org/10.1038/nenergy.2017.31.

(58) Sarabia, F. J.; Sebastián-Pascual, P.; Koper, M. T. M.; Climent, V.; Feliu, J. M. Effect of the Interfacial Water Structure on the Hydrogen Evolution Reaction on Pt(111) Modified with Different Nickel Hydroxide Coverages in Alkaline Media. *ACS Applied Materials and Interfaces* **2019**, *11* (1), 613–623. https://doi.org/10.1021/acsami.8b15003.

(59) Tripkovic, V.; Vegge, T. Potential- and Rate-Determining Step for Oxygen Reduction on Pt(111). *Journal of Physical Chemistry C* **2017**, *121* (48), 26785–26793. https://doi.org/10.1021/acs.jpcc.7b07472.

(60) Hansen, M. H.; Nilsson, A.; Rossmeisl, J. Modelling PH and Potential in Dynamic Structures of the Water/Pt(111) Interface on the Atomic Scale. *Physical Chemistry Chemical Physics* **2017**, *19* (34), 23505–23514. https://doi.org/10.1039/c7cp03576d.

(61) Dix, S. T.; Linic, S. In-Operando Surface-Sensitive Probing of Electrochemical Reactions on Nanoparticle Electrocatalysts: Spectroscopic Characterization of Reaction Intermediates and Elementary Steps of Oxygen Reduction Reaction on Pt. *Journal of Catalysis* **2021**, *396*, 32–39. https://doi.org/10.1016/j.jcat.2021.02.009.

(62) Chen, L. D.; Urushihara, M.; Chan, K.; Nørskov, J. K. Electric Field Effects in Electrochemical CO2 Reduction. *ACS Catalysis* **2016**, *6* (10), 7133–7139. https://doi.org/10.1021/acscatal.6b02299.

(63) Rebollar, L.; Intikhab, S.; Oliveira, N. J.; Yan, Y.; Xu, B.; McCrum, I. T.; Snyder, J. D.; Tang, M. H. "Beyond Adsorption" Descriptors in Hydrogen Electrocatalysis. *ACS Catal.* **2020**, 14747–14762. https://doi.org/10.1021/acscatal.0c03801.

(64) Roman, A. M.; Dudoff, J.; Baz, A.; Holewinski, A. Identifying " Optimal " Electrocatalysts: Impact of Operating Potential and Charge Transfer Model. *ACS Catalysis* **2017**, *7*, 8641–8652. https://doi.org/10.1021/acscatal.7b03235.

(65) Bhandari, S.; Rangarajan, S.; Maravelias, C. T.; Dumesic, J. A.; Mavrikakis, M. Reaction Mechanism of Vapor-Phase Formic Acid Decomposition over Platinum Catalysts: DFT, Reaction Kinetics Experiments, and Microkinetic Modeling. *ACS Catalysis* **2020**, *10* (7), 4112–4126. https://doi.org/10.1021/acscatal.9b05424.

(66) Medford, A. J.; Wellendorff, J.; Vojvodic, A.; Studt, F.; Abild-Pedersen, F.; Jacobsen, K. W.; Bligaard, T.; Nørskov, J. K. Assessing the Reliability of Calculated Catalytic Ammonia Synthesis Rates. *Science* **2014**, *345* (6193), 197–200. https://doi.org/10.1126/science.1253486.

(67) Walker, E. A.; Mitchell, D.; Terejanu, G. A.; Heyden, A. Identifying Active Sites of the Water-Gas Shift Reaction over Titania Supported Platinum Catalysts under Uncertainty. *ACS Catalysis* **2018**, *8* (5), 3990–3998. https://doi.org/10.1021/acscatal.7b03531.

(68) Sutton, J. E.; Guo, W.; Katsoulakis, M. A.; Vlachos, D. G. Effects of Correlated Parameters and Uncertainty in Electronic-Structure-Based Chemical Kinetic Modelling. *Nature Chemistry* **2016**, *8* (4), 331–337. https://doi.org/10.1038/nchem.2454.

(69) Falsig, H.; Hvolbæk, B.; Kristensen, I. S.; Jiang, T.; Bligaard, T.; Christensen, C. H.; Nørskov, J. K. Trends in the Catalytic CO Oxidation Activity of Nanoparticles. *Angewandte Chemie* **2008**, *47*, 4835–4839. https://doi.org/10.1002/anie.200801479.

(70) Yoo, J. S.; Abild-Pedersen, F.; Nørskov, J. K.; Studt, F. Theoretical Analysis of Transition-Metal Catalysts for Formic Acid Decomposition. *ACS Catalysis* **2014**, *4* (4), 1226–1233. https://doi.org/10.1021/cs400664z.

(71) Baz, A.; Holewinski, A. Understanding the Interplay of Bifunctional and Electronic Effects: Microkinetic Modeling of the CO Electro-Oxidation Reaction. *Journal of Catalysis* **2020**, *384*, 1–13. https://doi.org/10.1016/j.jcat.2020.02.003.

(72) Andersen, M.; Medford, A. J.; Nørskov, J. K.; Reuter, K. Analyzing the Case for Bifunctional Catalysis. *Angewandte Chemie - International Edition* **2016**, *55* (17), 5210–5214. https://doi.org/10.1002/anie.201601049.

(73) Andersen, M.; Medford, A. J.; Norskov, J. K.; Reuter, K. Scaling-Relation Based Analysis of Bifunctional Catalysis: The Case for Homogeneous Bimetallic Alloys. *ACS Catalysis* **2017**, acscatal.7b00482-acscatal.7b00482. https://doi.org/10.1021/acscatal.7b00482.

(74) Temel, B.; Meskine, H.; Reuter, K.; Scheffler, M.; Metiu, H. Does Phenomenological Kinetics Provide an Adequate Description of Heterogeneous Catalytic Reactions? *Journal of Chemical Physics* **2007**, *126* (20). https://doi.org/10.1063/1.2741556.

(75) Koper, M. T. M.; Jansen, A. P. J.; Van Santen, R. A.; Lukkien, J. J.; Hilbers, P. A. J. Monte Carlo Simulations of a Simple Model for the Electrocatalytic CO Oxidation on Platinum. *Journal of Chemical Physics* **1998**, *109* (14), 6051–6062. https://doi.org/10.1063/1.477230.

(76) Koper, M. T. M.; Jansen, A. P. J.; Lukkien, J. J. Lattice – Gas Modeling of Electrochemical Langmuir – Hinshelwood Surface Reactions. **1999**, *45*, 645–651.

(77) Koper, M. T. M.; Lukkien, J. J.; Jansen, A. P. J.; van Santen, R. A. Lattice Gas Model for CO Electrooxidation on Pt−Ru Bimetallic Surfaces. *The Journal of Physical Chemistry B* **1999**, *103* (26), 5522–5529. https://doi.org/10.1021/jp990520k.

(78) Jørgensen, M.; Grönbeck, H. The Site-Assembly Determines Catalytic Activity of Nanoparticles. *Angewandte Chemie - International Edition* **2018**, *57* (18), 5086–5089. https://doi.org/10.1002/anie.201802113.

(79) Koper, M. T. M. Statistical Mechanics and Kinetic Modeling of Electrochemical Reactions on Single-Crystal Electrodes Using the Lattice-Gas Approximation. *Advances in Electrochemical Science and Engineering* **2014**, *14*, 75–98. https://doi.org/10.1002/9783527680436.ch2.

(80) Garcia-Araez, N.; Lukkien, J. J.; Koper, M. T. M.; Feliu, J. M. Competitive Adsorption of Hydrogen and Bromide on Pt(1 0 0): Mean-Field Approximation vs. Monte Carlo Simulations. *Journal of Electroanalytical Chemistry* **2006**, *588* (1), 1–14. https://doi.org/10.1016/j.jelechem.2005.11.034.

(81) Lebedeva, N. P.; Koper, M. T. M.; Feliu, J. M.; van Santen, R. A. Mechanism and Kinetics of the Electrochemical CO Adlayer Oxidation on Pt(111). *Journal of Electroanalytical Chemistry* **2002**, *524* (525), 242–251. https://doi.org/10.1016/S0022-0728(02)00669-1.

(82) Bhandari, S.; Rangarajan, S.; Mavrikakis, M. Combining Computational Modeling with Reaction Kinetics Experiments for Elucidating the in Situ Nature of the Active Site in Catalysis. *Accounts of Chemical Research* **2020**, *53* (9), 1893–1904. https://doi.org/10.1021/acs.accounts.0c00340.

(83) Savara, A.; Walker, E. A. CheKiPEUQ Intro 1: Bayesian Parameter Estimation Considering Uncertainty or Error from Both Experiments and Theory**. *ChemCatChem* **2020**, *12* (21), 5385–5400. https://doi.org/10.1002/cctc.202000953.

(84) Mefford, J. T.; Zhao, Z.; Bajdich, M.; Chueh, W. C. Interpreting Tafel Behavior of Consecutive Electrochemical Reactions through Combined Thermodynamic and Steady State Microkinetic Approaches. *Energy and Environmental Science* **2020**, *13* (2), 622–634. https://doi.org/10.1039/c9ee02697e.

(85) Eberle, D.; Horstmann, B. Oxygen Reduction on Pt(111) in Aqueous Electrolyte: Elementary Kinetic Modeling. *Electrochimica Acta* **2014**, *137*, 714–720. https://doi.org/10.1016/j.electacta.2014.05.144.

(86) Gauthier, J. A.; Ringe, S.; Dickens, C. F.; Garza, A. J.; Bell, A. T.; Head-Gordon, M.; Nørskov, J. K.; Chan, K. Challenges in Modeling Electrochemical Reaction Energetics with Polarizable Continuum Models. *ACS Catalysis* **2019**, *9* (2), 920–931. https://doi.org/10.1021/acscatal.8b02793.

(87) Sandoval-Rojas, A. P.; Gómez-Marín, A. M.; Suárez-Herrera, M. F.; Climent, V.; Feliu, J. M. Role of the Interfacial Water Structure on Electrocatalysis: Oxygen Reduction on Pt(1 1 1) in Methanesulfonic Acid. *Catalysis Today* **2016**, *262*, 95–99. https://doi.org/10.1016/j.cattod.2015.08.046.

(88) Che, F.; Gray, J. T.; Ha, S.; Kruse, N.; Scott, S. L.; McEwen, J. S. Elucidating the Roles of Electric Fields in Catalysis: A Perspective. *ACS Catalysis* **2018**, *8* (6), 5153–5174. https://doi.org/10.1021/acscatal.7b02899.

(89) Eslamibidgoli, M. J.; Eikerling, M. H. Approaching the Self-Consistency Challenge of Electrocatalysis with Theory and Computation. *Current Opinion in Electrochemistry* **2018**. https://doi.org/10.1016/j.coelec.2018.03.038.

(90) Stamenkovic, V. R.; Strmcnik, D.; Lopes, P. P.; Markovic, N. M. Energy and Fuels from Electrochemical Interfaces. *Nature Materials* **2017**, *16* (1), 57. https://doi.org/10.1038/nmat4738.

(91) Sui, S.; Wang, X.; Zhou, X.; Su, Y.; Riffat, S.; Liu, C. A Comprehensive Review of Pt Electrocatalysts for the Oxygen Reduction Reaction: Nanostructure, Activity, Mechanism and Carbon Support in PEM Fuel Cells. *Journal of Materials Chemistry A* **2017**, *5* (5), 1808–1825. https://doi.org/10.1039/C6TA08580F.

(92) Osawa, M. Dynamic Processes in Electrochemical Reactions Studied by Surface-Enhanced Infrared Absorption Spectroscopy (SEIRAS). *Bulletin of the Chemical Society of Japan* **1997**, *70* (12), 2861–2880. https://doi.org/10.1246/bcsj.70.2861.

(93) Shao, M.; Liu, P.; Adzic, R. R. Superoxide Anion Is the Intermediate in the Oxygen Reduction Reaction on Platinum Electrodes. *J. Am. Chem. Soc.* **2006**, *128* (23), 7408–7409. https://doi.org/10.1021/ja061246s.

(94) Kukunuri, S.; Noguchi, H. In-Situ Spectroscopy Study of Oxygen Reduction Reaction Intermediates at Pt/Acid Interface: Surface Enhanced Infrared Absorbance Spectroscopy. *J. Phys. Chem. C* **2020**. https://doi.org/10.1021/acs.jpcc.9b11950.

(95) Zhu, S.; Qin, X.; Yao, Y.; Shao, M. PH-Dependent Hydrogen and Water Binding Energies on Platinum Surfaces as Directly Probed through Surface-Enhanced Infrared Absorption Spectroscopy. *J. Am. Chem. Soc.* **2020**, *142* (19), 8748–8754. https://doi.org/10.1021/jacs.0c01104.

(96) Rao, R. R.; Kolb, M. J.; Giordano, L.; Pedersen, A. F.; Katayama, Y.; Hwang, J.; Mehta, A.; You, H.; Lunger, J. R.; Zhou, H.; Halck, N. B.; Vegge, T.; Chorkendorff, I.; Stephens, I. E. L.; Shao-Horn, Y. Operando Identification of Site-Dependent Water Oxidation Activity on Ruthenium Dioxide Single-Crystal Surfaces. *Nature Catalysis* **2020**, *3* (6), 516–525. https://doi.org/10.1038/s41929-020-0457-6.

(97) Li, J.-F.; Zhang, Y.-J.; Ding, S.-Y.; Panneerselvam, R.; Tian, Z.-Q. Core–Shell Nanoparticle-Enhanced Raman Spectroscopy. *Chem. Rev.* **2017**, *117* (7), 5002–5069. https://doi.org/10.1021/acs.chemrev.6b00596.

(98) Dong, J.-C.; Zhang, X.-G.; Briega-Martos, V.; Jin, X.; Yang, J.; Chen, S.; Yang, Z.-L.; Wu, D.-Y.; Feliu, J. M.; Williams, C. T.; Tian, Z.-Q.; Li, J.-F. In Situ Raman Spectroscopic Evidence for Oxygen Reduction Reaction Intermediates at Platinum Single-Crystal Surfaces. *Nature Energy* **2019**, *4* (1), 60–67. https://doi.org/10.1038/s41560-018-0292-z.

(99) Zhao, Y.; Chang, X.; Malkani, A. S.; Yang, X.; Thompson, L.; Jiao, F.; Xu, B. Speciation of Cu Surfaces During the Electrochemical CO Reduction Reaction. *J. Am. Chem. Soc.* **2020**, *142* (21), 9735–9743. https://doi.org/10.1021/jacs.0c02354.

(100) Wen, B.-Y.; Chen, Q.-Q.; Radjenovic, P. M.; Dong, J.-C.; Tian, Z.-Q.; Li, J.-F. In Situ Surface-Enhanced Raman Spectroscopy Characterization of Electrocatalysis with Different Nanostructures. *Annu. Rev. Phys. Chem.* **2021**, *72* (1), 331–351. https://doi.org/10.1146/annurev-physchem-090519-034645.

Chapter 5 In-operando Probing of the ORR Mechanism on Pt Nanoparticles

5.1 Introduction

In this chapter, a mechanistic study of the oxygen reduction reaction (ORR) is presented. Chapter 1 provides a more in-depth discussion on the background and challenges of hydrogen fuel cell electrocatalysts, but a summary is provided below.

To combat the issue of expensive ORR electrocatalysts, there have been many attempts to improve the electrocatalyst efficiency by combining Pt with other metals to form Pt-metal alloys that exhibit higher reaction rates compared to pure Pt materials[1–4]. These studies have yielded a number of promising ORR electrocatalysts, among which Pt/3d (Ni, Co, Cu) metal alloy nanoparticles show the most promise[5–10].

Parallel to these efforts to identify better performing ORR electrocatalysts, there has also been a significant interest to unearth the reaction mechanism at the elementary step and critical surface intermediates levels[11–17]. Obtaining direct experimental spectroscopic evidence, in the form of vibrational or electronic spectra of relevant ORR surface intermediates at the electrified interfaces between an electrolyte and Pt nanoparticle electrocatalysts, however, has proven challenging. The experimental difficulties are associated with (i) the lack of surface sensitivity of many spectroscopic techniques, making it difficult to separate the spectroscopic signals associated with surface reaction intermediates from those associated with the species in the water-based electrolyte[18], (ii) the presence of the interfacial electric field effects which change as the electrode

potential changes, (iii) the presence of water molecules whose interfacial surface orientation changes as a function of potential, and (iv) the existence of electrolyte ions which further complicate the mechanism[19–24]. Due to these difficulties, spectroscopic studies of ORR have been rather limited and mainly focused on highly idealized model electrocatalysts or on idealized electrochemical environments that are not consistent with the above described electrocatalyst/electrolyte interface complexities[25]. For example, Adzic and coworkers used surface enhanced infrared reflection absorption spectroscopy (SEIRAS) whereas Dong et. al used shell-isolated nanoparticle-enhanced Raman spectroscopy (SHINERS) to investigate the reaction on the model single crystals of extended Au[26] and Pt[27,28] surfaces. Casalongue et. al conducted an in-situ x-ray photoelectron spectroscopy (XPS) at relatively low pressure (<100 Torr)[29] where humidified gas was used to simulate an aqueous electrolyte environment, while Nayak et. al used non-surface specific infrared spectroscopy to study Pt/C electrocatalysts in a limited vibrational mode range between 950-1500 cm^{-1}.[30] Due to these challenges in the spectroscopic characterization of electrochemical transformations, mechanistic understanding of ORR is largely based on either quantum chemical calculations (mainly employing Density Functional Theory (DFT)) of the energetics of various proposed reaction intermediates on idealized model Pt surfaces and on the experimental studies of reaction kinetics which are coupled to the mechanism using variations of microkinetic modelling[11].

Spectroscopic studies on non-model Pt nanoparticle electrocatalysts represent a missing link that is very valuable, since it serves to validate or dispute the mechanisms proposed based on the studies of model systems. In this chapter an in-operando spectroscopic study of the reaction intermediates involved in ORR on electrified Pt nanoparticle electrocatalysts is presented. To accomplish this,

we have designed and synthesized Ag-Pt core-shell nanoparticles, that contain a thin shell of Pt (approximately 1 nm) deposited on Ag nanoparticle cores (~ 60 nm diameter). We show that these nanostructures are ideal platforms for in-operando Plasmon Enhanced Raman Spectroscopy (PERS) of ORR on the Pt surface sites since the electrochemical transformations take place on the Pt surface, while the Ag core plays a role of an antenna which amplifies the Raman signal through the excited localized surface plasmons, giving the required spectroscopic surface sensitivity. These PERS studies are combined with DFT calculations to assign the measured surface-specific Raman vibrational spectra to relevant surface intermediates as a function of electrocatalyst potential. This is done by using DFT calculations to compute vibrational fingerprints of likely surface intermediates at various potential-dependent Pt/electrolyte surface environments and identify the reaction intermediates that are consistent with the experimental spectra. These vibrational assignments were further verified and validated by performing PERS measurements in deoxygenated electrolyte and heavy oxygen (O_2-18) saturated electrolyte. These studies allowed us to identity the presence of critical reaction intermediates (OH, O_2, OOH, and H_2O) on the Pt surface as the function of operating voltage and derive voltage-dependent elementary step mechanisms of the reaction.

5.2 Synthesis and Characterization of Ag-Pt Core-Shell Nanoparticles

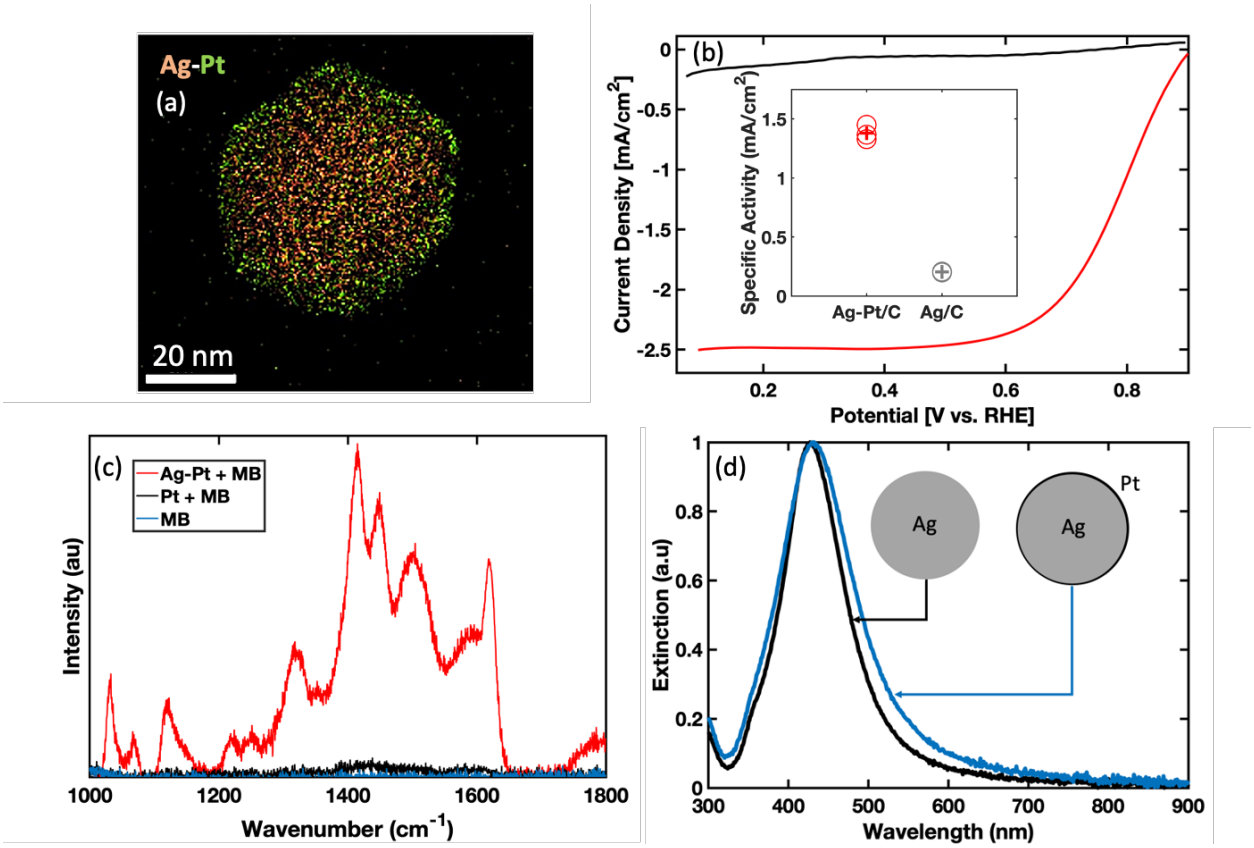


Figure 5.1(a) Energy-dispersive X-ray spectroscopy (EDS) map of the Ag-Pt nanoparticle. Ag is pink while Pt signal is green. (b) ORR current(rate)/voltage curve measured for the Ag-Pt nanoparticles at 50 mV/s in the in-operando flow cell in 0.1 M NaOH with O_2 (red) or He (black) saturating the electrolyte. (Inset) Electrochemical surface area normalized ORR current measured in a rotating disk electrode (RDE) setup of the Ag-Pt on carbon and monometallic Ag spheres on carbon. The kinetic current was measured at 0.9 V vs. RHE in O_2 saturated 0.1 M NaOH. (c) Raman spectra of methylene blue (MB) on a silica chip with and without the Ag-Pt nanoparticles or Pt nanoparticles (~ 20 nm diameter). The MB was deposited on the three substrates at identical concentration. The Raman laser wavelength was 532 nm. (d) UV-vis extinction spectra of the Ag nanoparticle (60 nm diameter) and the identical Ag particles covered by a thin Pt shell.

We used a colloidal approach to synthesize the Ag-Pt core-shell nanostructures as described in detail in Chapter 2 and previous publications[31,32]. In short, Ag nanoparticles of spherical shape with ~ 60 nm diameter were synthesized first. After washing, the Ag nanospheres were dispersed in a basic solution with a mild reducing agent (glucose). Upon addition of a Pt precursor (K_2PtCl_4), the Pt shell slowly forms on the Ag core. We have characterized these nanostructures, showing the presence of the thin Pt shell on the Ag cores. For example, the elemental mapping data in Figure

5.1a shows a spherical core-shell nanoparticle of ~ 60 nm in diameter with a thin Pt shell surrounding Ag. Since cubical shapes are easier to characterize with scanning transmission electron microscopy, we also synthesized Ag-Pt core-shell nanocubes using a similar approach. Further characterization of these materials is shown in Figure 5.2[31,32], suggesting an approximately 1 nm thick (~ 5 to 6 layers of Pt atoms) shell on Ag.

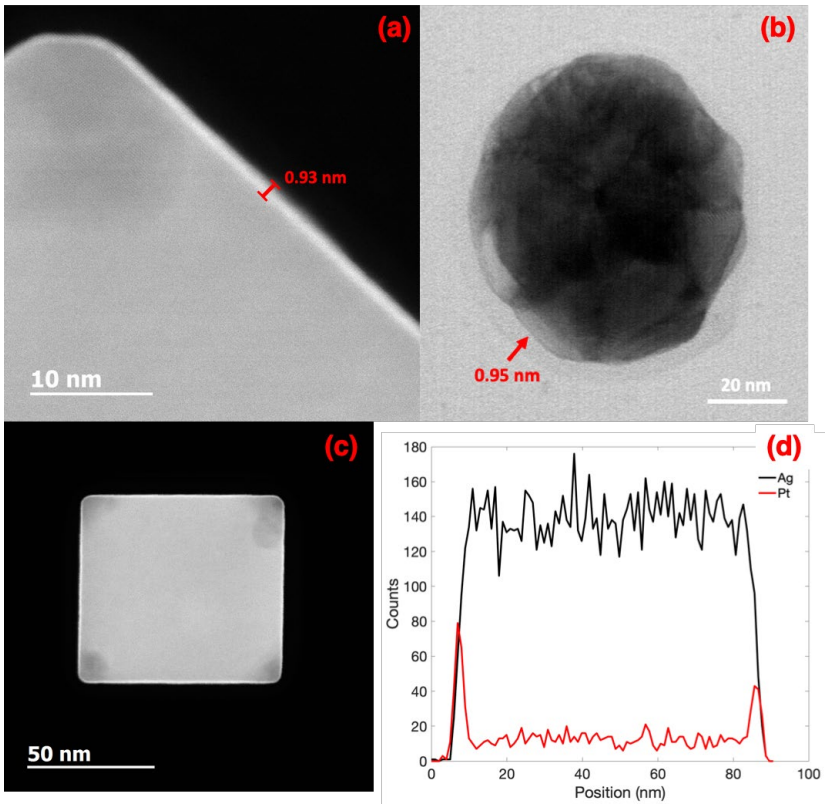


Figure 5.2 (a) Dark-Field STEM image of a Ag-Pt nanocube edge showing a Pt shell of 0.93 nm around a silver core. (b) Bright-Field STEM image of a single Ag-Pt nanosphere where a thin Pt shell of 0.95 nm around the Ag core can be seen. (c) Dark-field STEM image of an 80 nm edge length Ag-Pt nanocube. (d) EDS elemental line scan taken across the center of a Ag-Pt nanocube showing the elemental composition of the core and shell with Pt counts represented in red and black for Ag.

The first question to address was whether these Ag-Pt core-shell nanoparticles show electrochemical ORR activity that is consistent with the activities of Pt electrocatalysts. To address this, we used a three electrode rotating disk (RDE) setup to measure the ORR activity of the Ag-Pt core-shell nanostructures supported on carbon black in an O_2 saturated 0.1 M NaOH solution and compared it to the uncoated 60 nm Ag nanoparticle cores. The kinetic current densities

(reaction rates) for the Ag-Pt and Ag nanoparticle electrocatalysts, measured at the voltage of 0.9 versus a reversible hydrogen electrode (RHE) and normalized to the respective electrochemically active surface area of the Ag and Pt using a RDE, are plotted in the inset in Figure 5.1b[33,34]. The data in Figure 5.3 show the electrochemical surface-area normalized kinetic current density over a range of applied voltages.

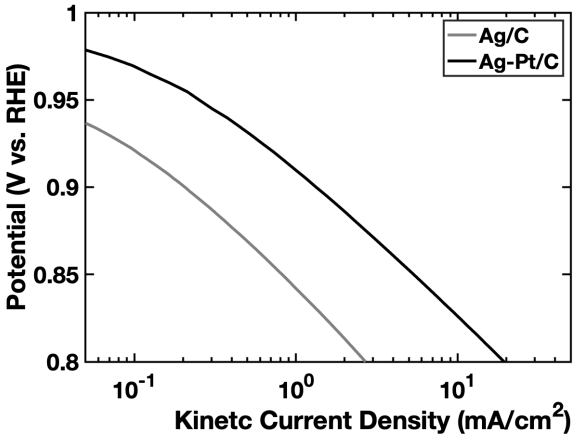


Figure 5.3 Tafel curves for Ag/C, and Ag-Pt/C at 1600 RPM in O_2 saturated 0.1 M NaOH. Each curve is corrected for capacitive currents and solution resistance.

The data in Figure 5.1b inset and Figure 5.3 show that the kinetic current (reaction rate) on Ag-Pt core-shell nanoparticles electrocatalyst is ~ 7 times higher than the rate on the Ag nanoparticle electrocatalyst, suggesting that the Pt surface atoms in the Ag-Pt core-shell nanoparticles are performing the reaction. Furthermore, the data in Figure 5.1b (inset) shows that the kinetic ORR current on the Ag-Pt core-shell nanoparticle electrocatalyst at 0.9 V vs. RHE is ~ 1.4 mA per cm^2 of Pt which is quantitatively consistent with the literature reported values for Pt nanoparticle electrocatalysts[35,36] and a polycrystalline-Pt electrode (Figure 5.4), suggesting that the electrochemical ORR takes place on the surface Pt sites which are engulfing the Ag core atoms.

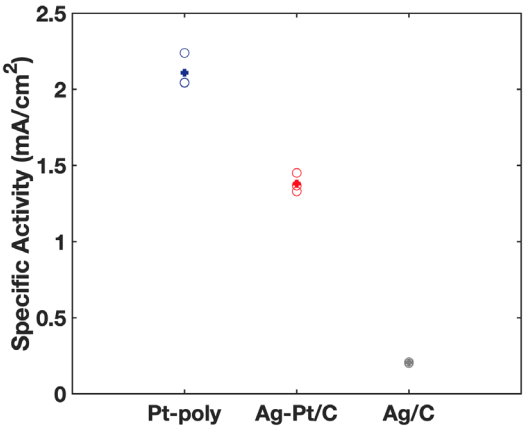


Figure 5.4 Electrochemical surface area normalized current measured on a Pt-poly electrode, 60 nm Ag-Pt/C, and 60 nm Ag spheres at 0.9 V vs. RHE in O_2 saturated 0.1 M NaOH measured using conventional rotating disk electrodes. 3 data points were taken for each catalyst.

We also assessed the ability of these Ag-Pt core-shell nanostructures to support surface enhancements in Raman spectroscopy measurements. The data in Figure 5.1c show measured Raman spectra (obtained using a 532 nm Raman laser) of a probe dye molecule (methylene blue (MB)) deposited on three different substrates. The data show that for MB deposited on a silica chip and on pure Pt nanoparticles covering the Si chip, the MB Raman spectra is hardly detectable. On the other hand, for an identical MB concentration deposited on the Ag-Pt core-shell nanoparticle on the silica chip, the intensity of Raman scattering is larger by several orders of magnitude. The reason for this large Raman intensity enhancement is that the Ag core in the Ag-Pt core-shell nanoparticles interact strongly with the incident 532 nm photons of the Raman laser through the excitation of localized surface plasmon resonance (LSPR). This strong interaction of light with the nanostructure results in an elevated optical extinction of the nanoparticles at resonant frequencies as shown in Figure 5.1d. Under these resonant excitation conditions, strong oscillating electric fields are established at the surface of the nanoparticle, amplifying the rates of Raman surface scattering[37–39]. We used finite difference time domain (FDTD) optical modeling (using COMSOL with a model previously used in the group[32,40]) to show that the oscillating electric field intensity

is ~ 35 times larger around the Pt shell of a Ag-Pt nanoparticle (consistent with our nanoparticle geometry) compared to the electric field of incoming light (Figure 5.5).

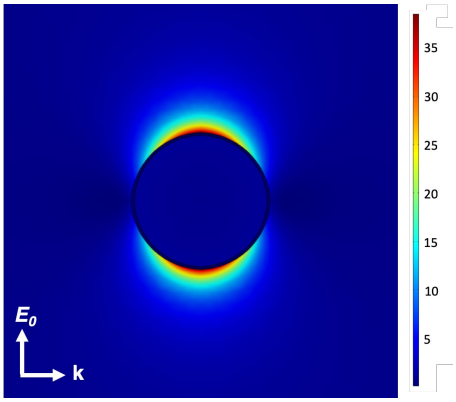


Figure 5.5 FDTD modeling of a 60 nm Ag core, 1 nm Pt shell nanoparticle exposed to incident 532 nm laser in water. The heat map shows up to 35-fold electric field intensity enhancement $(E/E_0)^2$.

This means that the expected surface enhancement in the Raman signal of a surface intermediate residing on the Ag-Pt nanoparticle surface compared to the surface of monometallic Pt nanoparticles is ~ 35^2 (which is ~ 10^3). We note that pure Pt nanoparticles do not support these plasmon induced Raman surface enhancement[39,41]. As a side note, we point out that the LSPR extinction spectra in Figure 5.1d show that the plasmon peak for Ag-Pt nanoparticles is slightly red-shifted and broader compared to pure Ag nanoparticles, which is fully consistent with the engulfment of the Ag core by a thin Pt shell[42–44]. Collectively, the data in Figure 5.1 show that the Ag-Pt core-shell nanoparticles achieve the reaction rates that are consistent with the reaction taking place on Pt nanoparticles, and that these materials are excellent platforms for surface sensitive Raman spectroscopy.

5.3 Spectroscopic Results and Discussion

The PERS measurements were performed in an electrochemical flow cell specifically designed for in-operando Raman spectroscopy (See Chapter 2)[45]. The working electrode contained the Ag-Pt core-shell nanoparticle electrocatalysts uniformly coated on a 100 nm thick Ag film. We used

Hg/HgO as a reference electrode and a clean Pt wire as a counter electrode. The data in Figure 5.1b show that the current (reaction rate) as a function of applied potential measured on the Ag-Pt nanoparticle electrocatalysts in this flow cell system exhibits all the features consistent with the ORR electrochemistry on Pt, including the mass transport, polarization and kinetic limited ORR rate regimes. The Pt-surface normalized kinetic current is also consistent with the currents measured in the rotating disk setup discussed above.

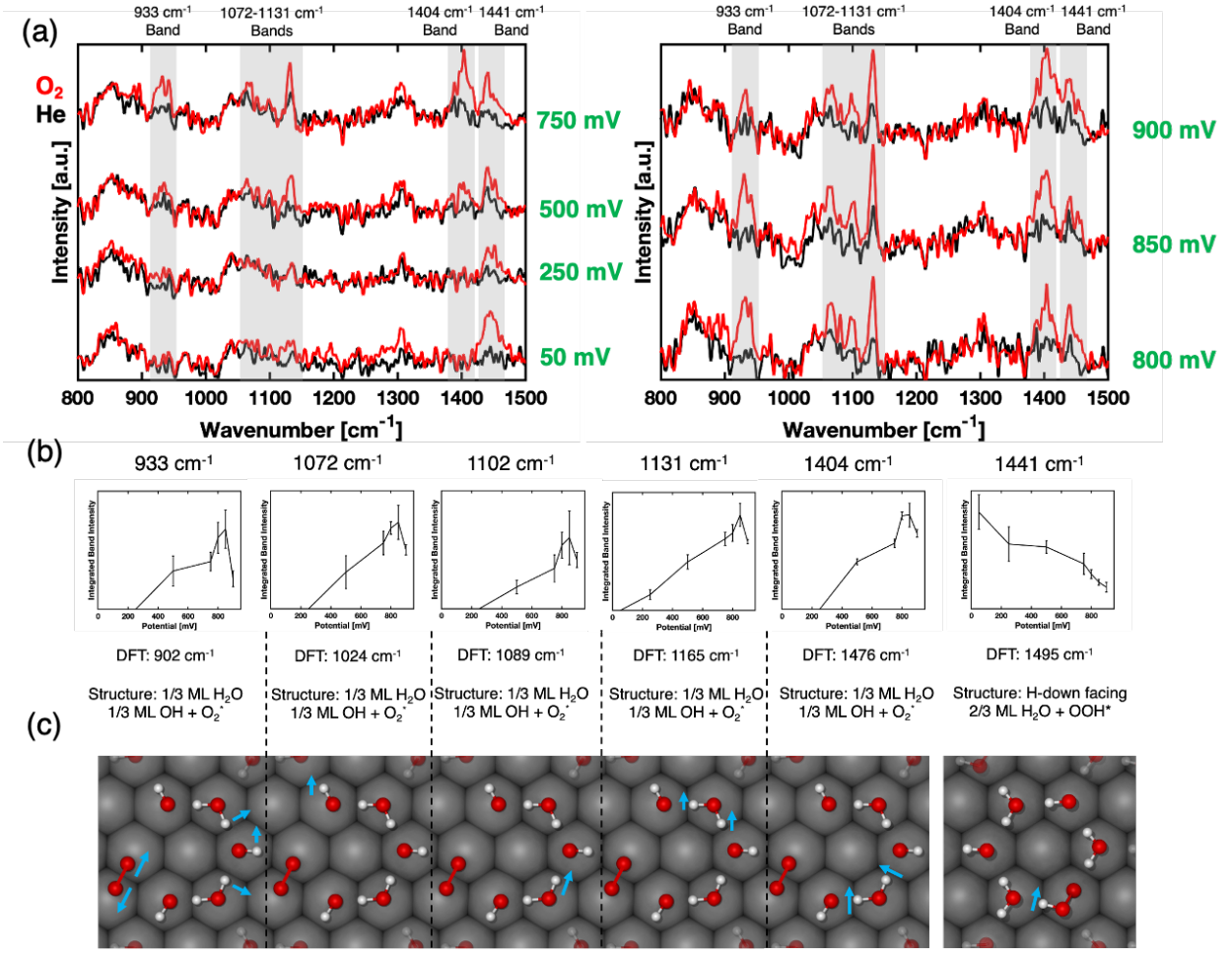


Figure 5.6 (a) Measured in-operando PER spectra of Ag-Pt nanoparticles in O_2 and He saturated 0.1 M NaOH at electrode voltages from 50 to 900 mV vs. RHE. (b) Statistical analysis of potential dependent intensity changes for oxygen sensitive bands of peaks at 933, 1072, 1102, 1131, 1404, and 1441 cm^{-1}. Error bars are ± the standard error of the population mean of n spectra taken for each potential where n is a minimum of 3. (c) The arrows represent the DFT calculated movement of atoms corresponding to different Raman vibrational modes. A 3x3 surface unit cell was employed.

The data in Figure 5.6a show the measured vibrational Raman spectra as the function of voltage obtained for the Ag-Pt core-shell nanoparticles in the O_2–saturated (ORR taking place) and de-oxygenated, He-saturated 0.1 M NaOH electrolyte. To determine whether defects in the Pt shell through "pinholes" impacted the Raman data, PERS measurements were repeated for pure Ag spheres as seen in Figure 5.7. The difference in the Ag and Ag-Pt PER spectra suggest that the electro-chemical transformations mainly take place on the Pt shell of the core-shell system and that the existence of "pinholes", if present, do not significantly contribute to the Raman data.

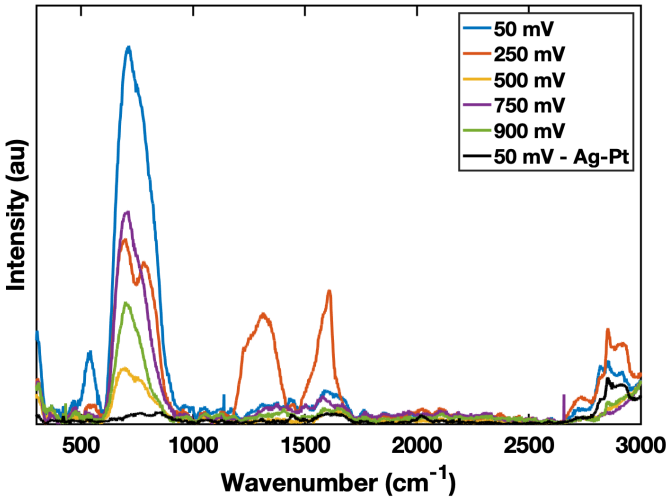


Figure 5.7 In-operando measurements of 60 nm Ag spheres in 0.1 M NaOH. The Ag spheres show large amounts of potential dependence that could be its own study. Most interesting is the strong potential dependence of peaks around 700 cm^{-1} that does not show up for Ag-Pt. In general, the most intense peak is ~10x the intensity of Ag-Pt's which is to be expected as pure Ag spheres have higher electric field enhancements at their surface. The Ag-Pt spectra is shown in black at 50 mV for comparison.

The PERS data on Ag-Pt show three information-rich families of Raman spectra:

(i) The O_2 and the electrode potential-sensitive Raman modes, appearing at 933, 1072, 1102, 1131, 1404 and 1441 cm^{-1} (see Figure 5.6a and Figure 5.6b). These modes do not show up in the He-saturated electrolyte. The data in Figure 5.6a show representative PER spectra, while the data in Figure 5.6b shows the statistical analysis (detailed in Chapter 2) of the intensities of the Raman peaks as the function of voltage. The data

show that as the potential increases, the intensities of the O_2-sensitive bands of peaks at 933, 1072, 1102, 1131 and 1404 cm^{-1} increase. On the other hand, the intensity of the O_2-sensitive 1441 cm^{-1} mode decreases with increasing electrode potentials.

(ii) The Raman modes at 1600, 1664, 2020 cm^{-1} (see Figure 5.11a and b) that appear with identical intensities in both, the O_2- and He-saturated electrolytes, and are sensitive to changes in the electrode potential. The data show that the voltage-dependent and oxygen-insensitive spectral features at 1600 cm^{-1} is maximized at 750 mV while the features at 1664 cm^{-1} and 2020 cm^{-1} decrease with increasing potential.

(iii) The Raman features between 2800 and 3000 cm^{-1} that exhibit a weak electrode potential dependence and that appear in the O_2- and He-saturated electrolytes. The data in Figure 5.11 show that at a given potential the intensity of these modes is larger in the O_2-saturated compared to the He-saturated electrolytes.

To aid in the assignment of the experimentally measured Raman spectra, DFT calculations were used to model the complex, potential-dependent Pt/electrolyte(water) interface. We employed the Pt(111) model surface, which is consistent with the spherical shape of the nanoparticles used in the PERS measurements that are dominated by the (111) surface facet. Our strategy was to focus on the thermodynamically stable, potential-dependent geometric configurations of the Pt/water interface that have been derived previously based on ab-initio thermodynamics and molecular dynamics modeling[12,46]. The vibrational Raman spectra of the likely reaction intermediates (O_2, OH, O, OOH, etc.) were calculated by embedding these intermediates within these potential-dependent, thermodynamically relevant surface/water interfaces and converging the structures to their lowest energy configurations.

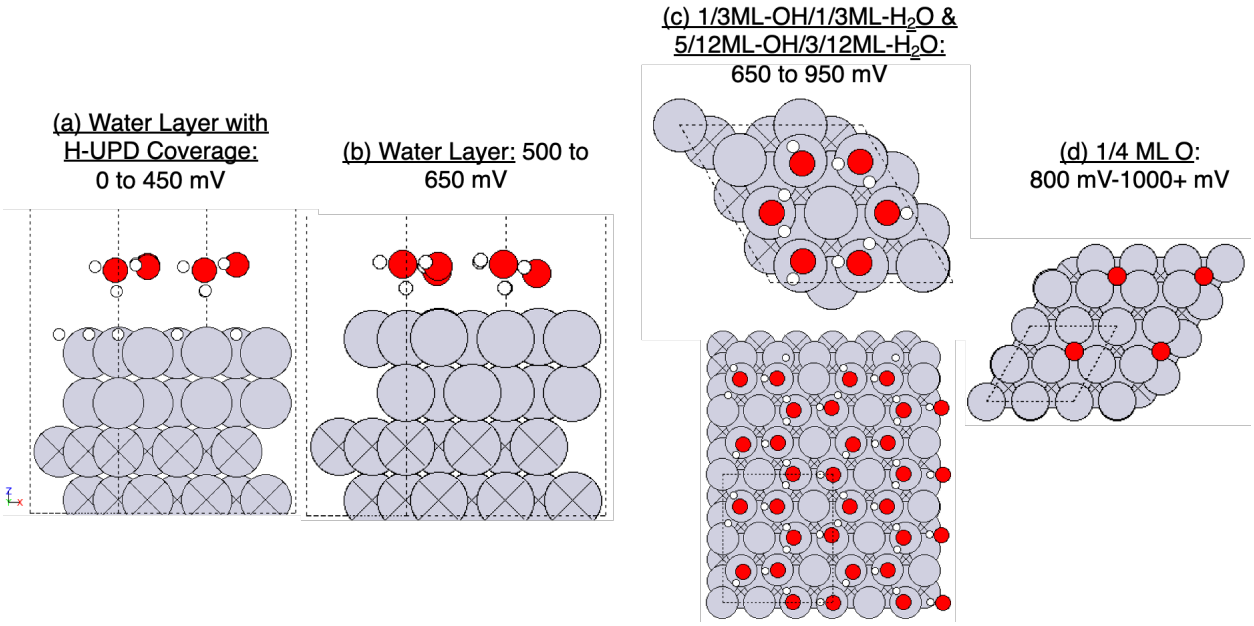


Figure 5.8 Simulated potential dependent electrified Pt(111)/electrolyte interfaces. Specific DFT models are created based on ab-initio thermodynamic calculations found before vibrational analysis is performed to create a database of possible vibrational modes found with experiment. (a) 2/3 ML H_2O + 1ML H-UPD. (b) 2/3 ML H_2O. (c) 1/3ML-OH/1/3ML-H_2O and 5/12ML-OH/3/12ML-H_2O. (d) 1/4 ML O.

The relevant potential-dependent water/Pt(111) interfacial configurations are shown in Figure 5.8. For the modeling of these surfaces, A 2x2 unit cell is used for the 1/4 ML O surface, 3x3 cell for the 2/3 ML H_2O (with and without H-UPD present) and 1/3ML-OH/1/3ML-H_2O surfaces and 3x4 for the 5/12ML-OH/3/12ML-H_2O surface. Expanded unit cells were used when addition of adsorbates necessitated it. Additional DFT details are found in Chapter 2. At potentials below 450 mV wrt. RHE, the process of the hydrogen underpotential deposition on Pt takes place. Ab-initio thermodynamic studies have shown that under these conditions, a water layer with the water hydrogen atoms facing towards the surface rests above underpotential deposited hydrogen (H-UPD) atoms adsorbed in three-fold hollow sites (Figure 5.8a)[47,52]. As potential increases, the H-UPD atoms desorb from the surface, and the water layer above the Pt surface moves closer to the surface (Figure 5.8b). As potential further increases, the Pt surface approaches the potential of zero charge (pzc), allowing the water molecules to be more loosely arranged above the Pt surface[53].

Eventually, water molecules are split and the hydroxide adsorbate (OH) starts populating the surface above ~ 650 mV[12]. This leads to the formation of OH-H_2O hydrogen bonds which results in the establishment of the hydrogen bonding-reinforced hexagonal H_2O/OH network, which resides flat on the Pt surface (Figure 5.8c). At the electric potential above ~ 650 mV two OH/H_2O networks are considered: (1) a 1/3ML-OH/1/3ML-H_2O and a (2) 5/12ML-OH/3/12MLH_2O. Both structures have similar free energy and both have been identified as thermodynamically stable under these conditions[12,46]. As potential increases further above 0.9 V, the O-H bond in the adsorbed OH is cleaved and oxygen atoms are formed on the Pt surface. Vibrational modes are found for all interfacial structures with H, O, O_2, and OOH adsorbates added or replacing parts of these thermodynamically stable structures, resulting in 500+ vibrational modes. We note that due to the diversity of surface sites on our non-model nanoparticle system and dynamic fluctuations, there are significant overlaps between these different phases as a function of voltage.

As mentioned above, our approach was to embed various possible reaction intermediates (O_2, OOH, OH, O) in these thermodynamically stable water/Pt networks and use DFT to compute the Raman spectra associated with these intermediates. In this process, we identified the lowest energy states of the intermediates in these water/Pt networks, and by comparing the measured to the computed Raman spectra, we were able to identify the reaction intermediates as the function of potential.

We first focus on the analysis of the O_2 and electrode potential-sensitive spectral features at 933, 1072, 1102, 1131, 1404 cm^{-1}. The data in Figure 5.6b show that these Raman bands increase in intensity as the function of the electrode potential. Based on the DFT calculations, we assigned these bands to the structures where an O_2 molecule is embedded in a 1/3ML-OH/1/3ML-H_2O structure[12]. Collective atomic movements associated with these Raman active vibrational modes

are indicated by blue arrows in Figure 5.6c. For example, the DFT simulated mode at 903 cm^{-1} (measured at 933 cm^{-1}) is directly associated with the O-O stretch within the O_2 molecule on the Pt surface embedded in the 1/3ML-OH/1/3ML-H_2O network, giving us an indication for the presence of this intermediate. The other modes are associated with the movements of atoms in this 1/3ML-OH/1/3ML-H_2O network, which are influenced by the presence of O_2 within the network. The intensity of these modes increases as the function of potential, which is consistent with the fact that the OH/H_2O network starts appearing on the surface at higher voltages as the OH adsorbate starts to populate the surface Pt sites. Another piece of information that supports these Raman mode assignments is that the modes associated with the motions of atoms in the flat OH/H_2O network (1072, 1102, 1131, 1404 cm^{-1}) are very weak or do not appear in the He-purged electrolyte (i.e., without the O_2 present in the electrolyte). The reason is that the Raman selection rules for the hexagonal symmetry of the 1/3ML-OH/1/3ML-H_2O network makes these modes Raman inactive. The introduction of O_2 to the surface leads to the breaking of the symmetry of the hexagonal network, which gives rise to these modes.

The data in Figure 5.6b show that unlike the above discussed modes associated with the O_2 molecule on the surface, the intensity of the O_2-sensitive mode at 1441 cm^{-1} decreases with increasing potential. Based on DFT calculations, we assigned this peak to the OOH intermediate embedded in a network of 2/3 ML H_2O molecules with the H atoms in H_2O pointing to the Pt surface (Figure 5.6c and Figure 5.8b). This H_2O structure is more stable at lower potentials owing to the negatively charged Pt surface that electrostatically reorients the water molecules toward this configuration. The decreasing intensity of the vibrational mode with increasing potential suggests that the surface concentration of the OOH intermediate declines as the function of an increasing voltage.

To further confirm the in-situ Raman peak assignments, heavy oxygen (97 wt% O_2-18, Sigma Aldrich) was used in Raman experiments. The same conditions were used as described above, however, to conserve O_2-18 the electrolyte reservoirs were first saturated with helium to remove air from the system. Subsequently, O_2-18 or O_2-16 was slowly bubbled into the reservoir under the blanketing helium gas allowing for ORR to occur on the Ag-Pt nanoparticles. A 50x long working distance Raman objective (Olympus, SLMPlan N) was used to collect at least 3 spectra for each potential. Quite surprisingly we found that these Raman modes were insensitive to the nature of the O_2 isotope (Figure 5.9).

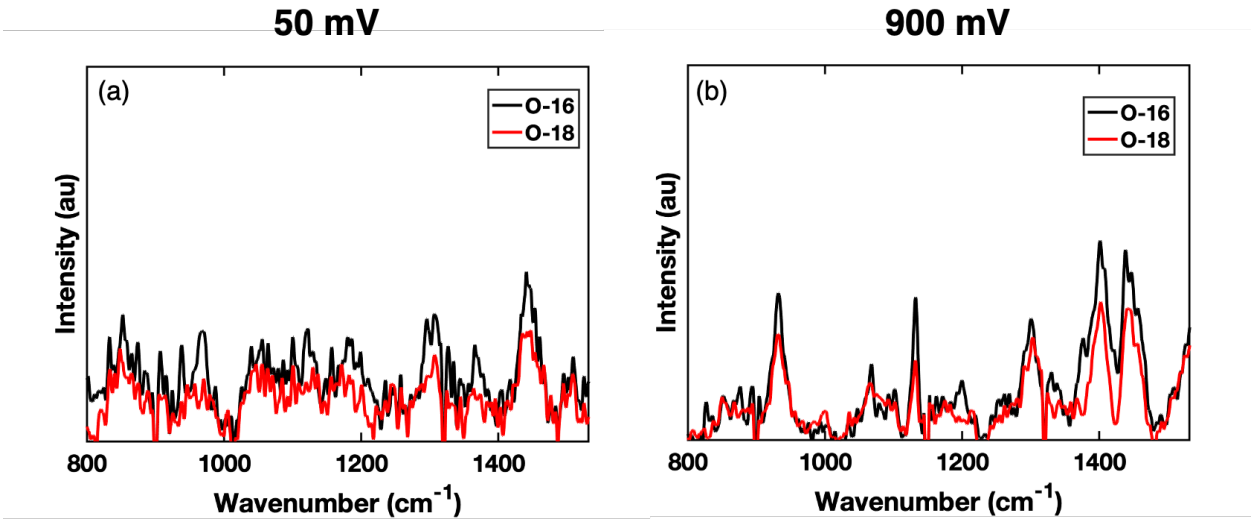


Figure 5.9 Operando Raman spectra of the Ag-Pt nanoparticles in 0.1 M NaOH at (a) 50 mV and (b) 900 mV where bubbled O_2-16 is in black and O_2-18 is in red.

To explain this observation, we performed DFT calculations to compute the Raman spectra for O_2-16 and O_2-18 in vacuum (Figure 5.10) and in the thermodynamically stable interfacial structures. In particular, the two relevant models identified, where O_2 and OOH are inserted in the 1/3 ML H_2O 1/3 ML OH and H-down facing 2/3 ML H_2O, were analyzed. The calculated vibrational mode frequencies are shown in Table 5.1 and Table 5.2.

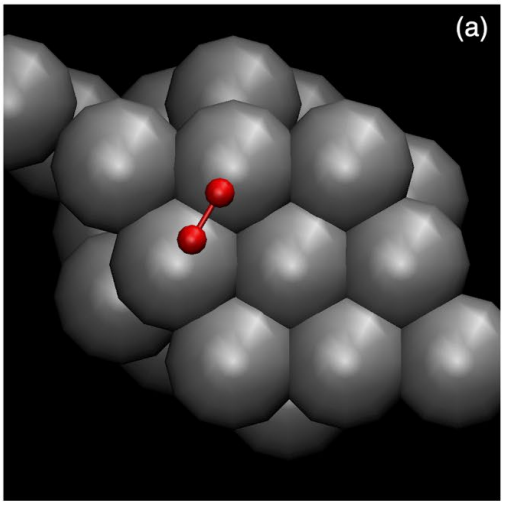
Table 5.1 Vibrational mode frequencies (in cm^{-1}) of O_2 in 1/3 ML H_2O 1/3 ML OH with O-16 or O-18 oxygens in O_2.

Experimental Band	1/3 ML H_2O 1/3 ML OH + O_2	
	O_2-16	O_2-18
933	**890.1**	**888.1**
1072	**1022.3**	**1021.9**
1102	**1086.7**	**1086.5**
1131	**1163.8**	**1163.7**
1404	**1476.0**	**1474.8**

Table 5.2 Vibrational mode frequencies (in cm^{-1}) of OOH in H-down facing 2/3 ML H_2O with O-16 or O-18 oxygens in OOH.

Experimental Band	H-down facing 2/3 ML H_2O + OOH	
	O_2-16	O_2-18
1441	**1498.0**	**1494.7**

The data in Table 5.1 and Table 5.2 show that, consistent with the experimental results, the complex vibrational modes do not exhibit significant shifts when O_2-18 is introduced in place of O_2-16. We also performed a control calculation of the vibrational modes associated with a single gas-phase O_2 adsorbed on clean 3x3 Pt(111) surface (shown in Figure 5.10) to demonstrate that our DFT methods could capture these shifts. The calculations showed that as expected, when switching from O_2-16 to O_2-18 vibrational modes shift to lower wavenumbers (Figure 5.10b). These calculations gave as a high degree of confidence that the approach was able to capture the isotope labeling induced shifts in the frequency of the affected modes.



(b)

O_2-16	O_2-18
856 cm^{-1}	808 cm^{-1}
546 cm^{-1}	515 cm^{-1}
406 cm^{-1}	385 cm^{-1}

Figure 5.10 (a) 1/9 ML O_2 adsorbed in a bridge site on a 3x3 Pt(111) surface. (b) DFT calculated Raman modes with oxygen masses of 16 in the left column and 18 in the right column.

These calculations support the experimental observations leading us to conclude that in this water environment, the O_2 isotopic labeling does not yield significant shifts in the observed Raman spectra associated with the O_2 intermediates due to the collective nature of the molecular vibrations (Table 5.1 and Table 5.2).

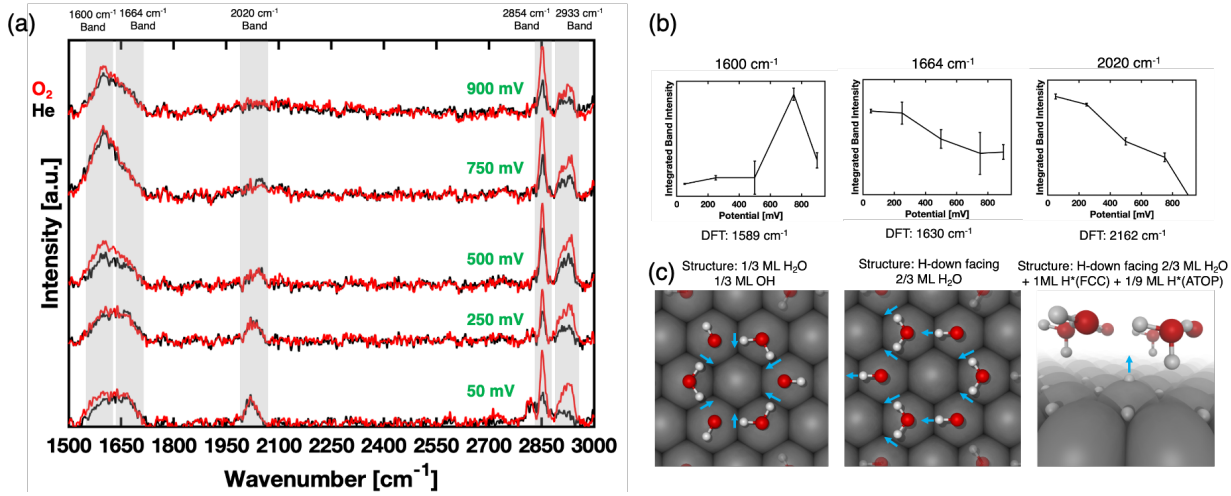


Figure 5.11 (a) Measured in-operando PER spectra of Ag-Pt nanoparticles in O_2 and He saturated 0.1 M NaOH from 50 to 900 mV vs. RHE. (b) Statistical analysis of potential dependent changes for oxygen insensitive modes at 1600, 1664, and 2020 cm^{-1}. Error bars are ± the standard error of the population mean of n spectra taken for each potential where n is a minimum of 3. (c) The arrows represent the DFT calculated movement of atoms corresponding to different Raman vibrational modes. A 3x3 surface unit cell was employed.

We also analyzed the potential-dependent behavior of the spectral features that are not sensitive to the presence of O_2 in the electrolyte and that appear with equal intensities in the O_2- and He-purged electrolyte (Figure 5.11). The Raman band centered at 1600 cm^{-1} increases with increasing potential reaching its maximum intensity at 750 mV (Figure 5.11b). Based in DFT calculations, we assign this peak to the H_2O bending mode in the 1/3ML-OH/1/3ML-H_2O network. The observed maximum intensity of this mode at the potential of around 750 – 800 mV is consistent with the notion that at the potentials higher than ~ 800 mV the H_2O/OH network is disrupted by the formation of the O atoms on the surface, while at significantly lower potentials the OH is not available on the surface. It is informative to note that unlike the above-discussed Raman inactive H_2O/OH modes (1072, 1102, 1131, 1404 cm^{-1}), which are not visible in the He electrolyte due to the hexagonal symmetry of the 1/3ML-OH/1/3ML-H_2O network on Pt, the mode at 1600 cm^{-1} can be detected in both electrolytes since it is not subject to the same Raman surface selection rules.

The data in Figure 5.11a and Figure 5.11b also show that the bands at 1664 cm^{-1} and 2020 cm^{-1} decrease in intensity as the potential is increased in both the He and O_2 electrolytes. Our DFT calculations show that the 1664 cm^{-1} mode corresponds to a molecular H_2O bending within the 2/3 ML H_2O structure with H atoms in water facing down to the Pt surface. We assigned the peak at 2020 cm^{-1} to the Pt-H vibrations, where H atoms in Pt top sites, surrounded by H_2O vibrate on the Pt surface. This H-vibration mode has also been previously identified in the literature to appear between 2000-2100 cm^{-1} [54]. It has also been proposed that this mode exhibits a strong Stark tuning effect, with its frequency changing with electric field intensity[47,51]. This Stark tuning effect is observed in our experimental data in Figure 5.11 that show this mode shifts to higher wavenumbers as the potential is increased. We note that in this same vibrational range, a linearly bonded CO on Pt would appear in CO-polluted electrolyte. To rule out CO contamination in the assignment of

the Pt-H at 2020 cm^{-1}, we performed a set of control experiments using CO saturated electrolyte. The results (Figure 5.12) show that the peak at 2020 cm^{-1} is likely not CO as the adsorption of CO is characterized by two Raman vibrational modes. This is a well-known fact as it has been observed that CO adsorbs on top and bridge Pt sites[55].

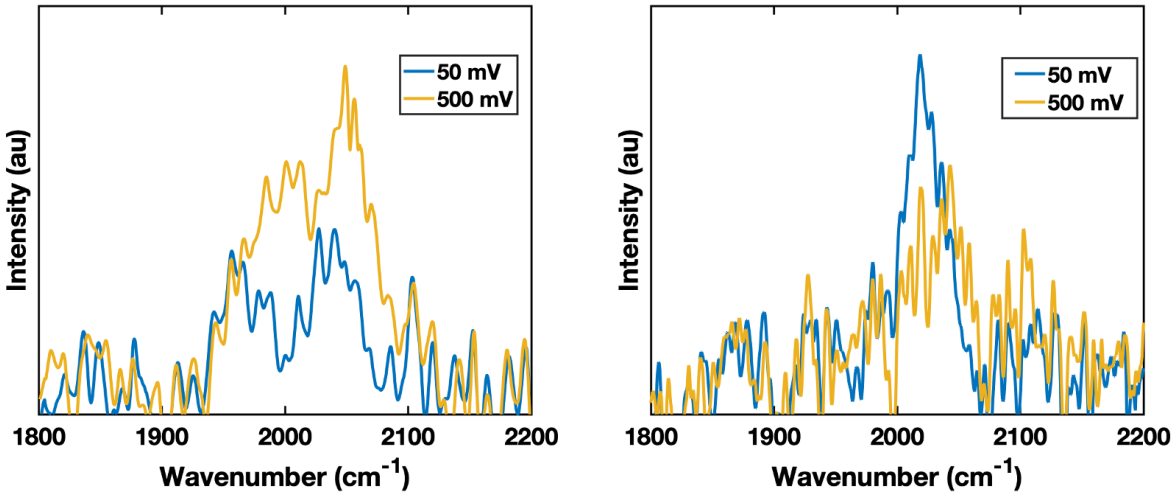


Figure 5.12 (Left) In-situ PERS measurements of CO on Ag-Pt nanoparticles in CO saturated 0.1 M NaOH. Two distinct CO peaks appear in the region between 1900 and 2100 wavenumbers. These peaks shift to higher wavenumber at higher potential. (Right) In-situ measurements on the Ag-Pt nanoparticles in the CO-free, oxygenated electrolyte for comparison. We ascribe this spectrum to H on Pt.

Additionally, we also detected Raman modes centered at 2854 and 2933 cm^{-1} in both, the oxygen and helium saturated electrolytes. These modes are more intense when O_2 is present and do not exhibit significant potential dependence (Figure 5.13). This is especially pronounced at 50 mV where the peak at 2854 cm^{-1} is increased 4x in intensity and the peak at 2933 cm^{-1} becomes detectable when O_2 is saturating the electrolyte. These peaks match well with modes associated with the movement of H atoms in the 1/3ML-OH/1/3ML-H_2O (2835, 2879 cm^{-1}) and the 5/12ML-OH/3/12ML-H_2O structures (2853, 2980 cm^{-1}). Since these OH/H_2O networks are not stable on the Pt(111) surface at the low potentials (50, 250 mV), we cannot associate these modes with these surface networks. Potential explanation for these modes is that, as pointed by Janik and coworkers, these OH/H_2O networks can exist on more chemically active non-(111) surface facets of Pt even

at low potentials (50, 250 mV)[56]. This would imply that these OH/H_2O networks could exist at low potentials on the Pt defects such as edges and kinks sites. Alternatively, these modes could simply be associated with the networks of OH^- surrounded with H_2O molecules in the vicinity or at the electrocatalyst surface. Since these modes are more pronounced when O_2 is present, this would indicate that the introduction of O_2 leads to an accumulation of OH^- at the surface within the double layer.

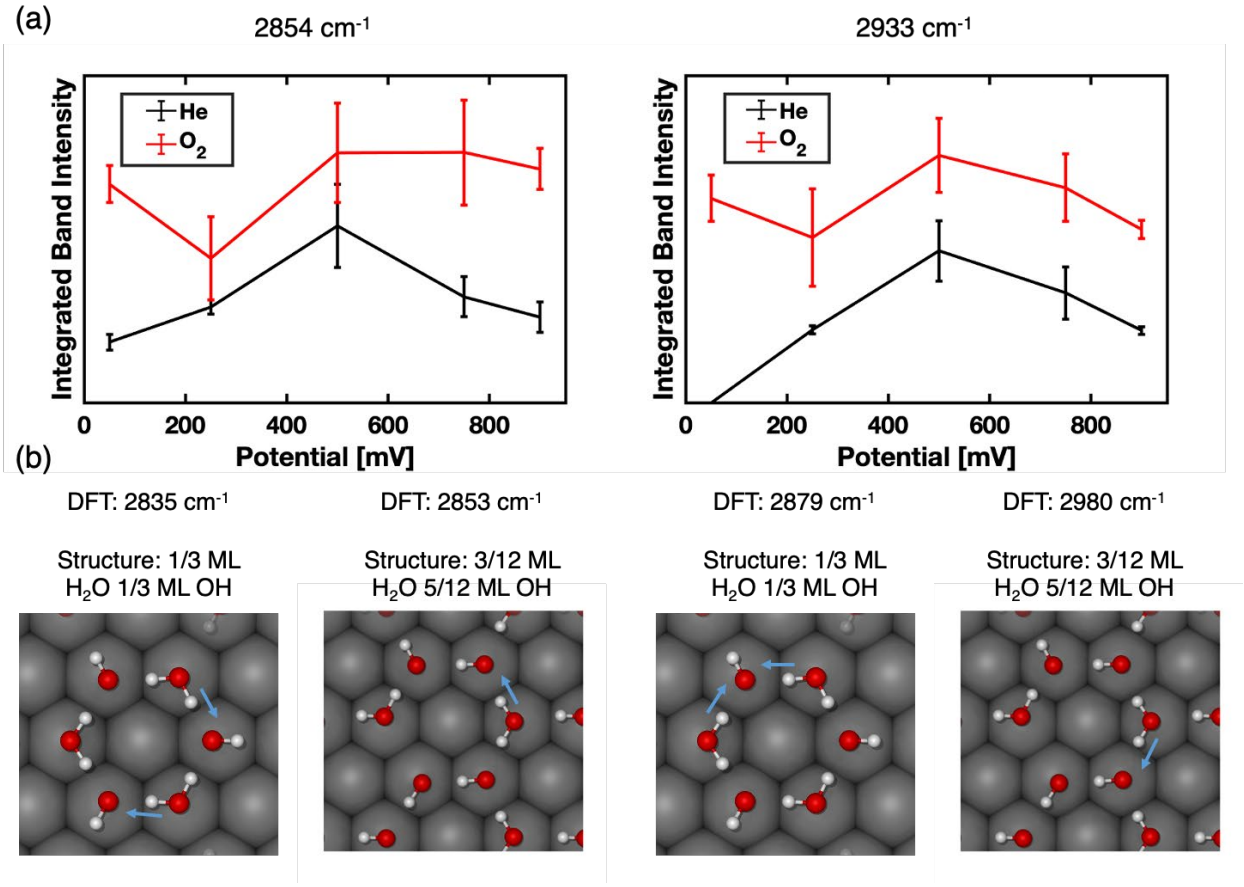


Figure 5.13 (a) Integrated band intensities of Raman peaks at 2854 and 2933 cm^{-1} in O_2 (red) and He (black). When O_2 concentrations are high in the electrolyte, no clear trend is observed with respect to potential. When O_2 is absent, the two peaks appear to reach a maximum size at 500 mV before decreasing in intensity. The band at 2933 cm^{-1} could not be detected at 50 mV without oxygen present in the electrolyte. Error bars are ± the standard error of the population mean of n spectra taken for each potential where n is a minimum of 3. (b) DFT calculated vibrational modes associated with the Raman active movement of H_2O on the Pt surface. Molecule perturbations are indicated with blue arrows for each simulated peak.

There are a few critical observations of the PERS studies that shed light on the reaction mechanism. First, the measured Raman spectra directly identifies the potential-dependent, thermodynamically

stable structures at the water/Pt electrified interface on Pt nanoparticle electrocatalysts. At low potentials, loosely bonded water molecules with hydrogens facing down populate the Pt surface. As the potential is increased, water and hydroxyl molecules are adsorbed more strongly on Pt top sites in a hexagonal 1/3ML-OH/1/3ML-H_2O surface patterns as evidenced by bands of peaks at 1072, 1102, 1131, 1404 and 1600 cm^{-1}. This structure seems to be the most pronounced at around 750 mV as OH and H_2O molecules are replaced with O atoms at higher voltages. Perhaps a surprising outcome of this work is that these different thermodynamically stable configurations seem to co-exist on the nanoparticle surface over relatively wide potential ranges, indicating that the diversity of the surface sites provides a wide range of binding energies for surface intermediates (mainly OH and O) that influence the existence of the different surface structures. Perhaps most importantly, our spectroscopic data point to the existence of surface intermediates with the preserved O-O chemical bond. The data showed that at high potentials, the O-O surface intermediate was observed (peak at 933 cm^{-1}). The data also show that at lower potentials the O-OH intermediate (peak at 1441 cm^{-1}) was detected which is consistent with the recent in-situ studies by Nayak et. al that showed decreasing abundance of OOH as a function of increasing potential[30]. These observations suggest that over a wide range of operating voltage, the oxygen reduction reaction could proceed via an associative mechanism where O_2 does not spontaneously, thermally decompose on the Pt surface upon its adsorption.

The sketch in Figure 5.14, shows the potential energy surface of the ORR on Pt surface sites that is consistent with the spectroscopic analysis reported herein. The potential-dependence of the relative abundance of these two intermediates (O-O and O-OH), where at high electrode potentials the O-O intermediate is detected at higher quantities, and at low potentials O-OH is a more abundant intermediate, is suggestive of the fact that the dissociation of O_2 involves a proton-

electron addition to the adsorbed O_2 and the formation of the O-OH intermediate. At high voltages (Figure 5.14), the proton-electron addition step (O_2* + (e^- + H^+) → *OOH in acid and O_2* + (e^- + H_2O) → *OOH + OH^- in base) is slow compared to the O-OH dissociation step, so we can observe the O-O intermediate on the surface. On the other hand, at lower voltages, the proton-electron addition step is fast, and the O-OH intermediate is trapped on the surface. The fact that we can even observe the O-OH intermediate leads us to conclude that the dissociation of this intermediate is an activated process with an activation barrier that is low but sufficient for the trapping of this intermediate on the surface. Finally, these spectroscopic studies support the notion that the Pt surface operates in two different kinetic regimes as a function of the Pt electrode potential. At high voltage, the reaction rate is affected by the presence of the packed network of OH and water, which makes it difficult for O_2 to find landing spots on the surface, and by the slow rates of proton-electron addition to the adsorbed O_2. On the other hand, at lower voltages (far from equilibrium) the surface is clean, and the rate is controlled by the formation of the O-OH intermediate and its conversion to OH and O.

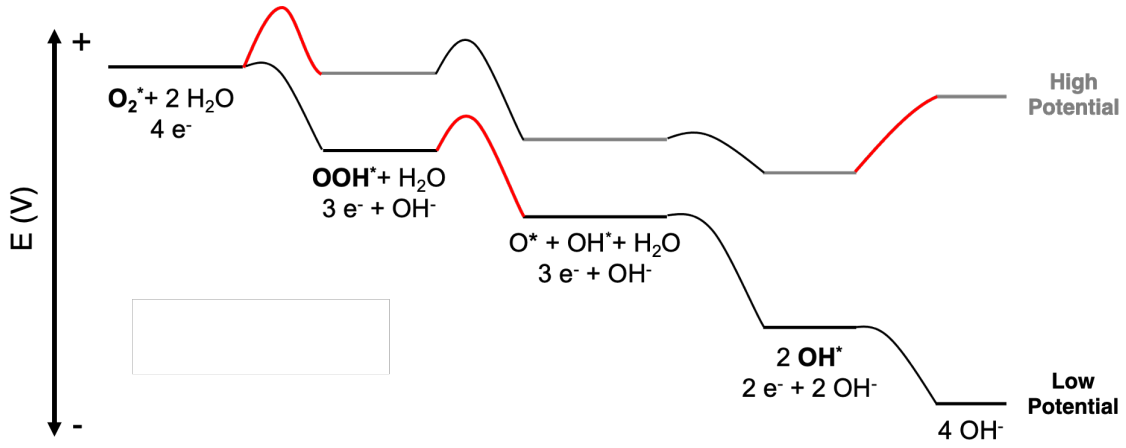


Figure 5.14 Potential energy surface for various intermediates of the ORR on Pt derived from the PERS data. High potential is consistent with ~750-900 mV while low potential refers to ~50-500 mV. The red barriers indicate kinetically relevant steps that trap reactant intermediates on the Pt surface allowing for spectroscopic detection.

5.4 Conclusions

In-operando characterization of heterogeneous electrochemical reactions at the levels of elementary steps and critical surface intermediates is challenging due to a buried, complex and potential-dependent electrolyte/electrocatalyst interface where these reactions take place. To address this challenge, we designed and synthesized Ag-Pt core-shell nanoparticle electrocatalysts that exhibits a high degree of surface enhancements in Raman spectroscopy. The Raman surface enhancements are derived from the Ag core which interacts strongly with visible light through the excitation of LSPR. This material platform allows us to study the (electro)chemical transformations that take place on Pt surfaces and probe surface intermediates with a high surface sensitivity. We note that monometallic Pt nanoparticles do not support surface enhancements in Raman spectroscopy. We have used these Ag-Pt nanoparticle materials to perform a detailed Raman spectroscopy study of the mechanism of electrochemical ORR. The studies showed that these materials exhibit the ORR activity consistent with monometallic Pt electrocatalysis. Based on the DFT computed assignments of Raman spectral features we identified the critical electrolyte/Pt interfacial structures as a function of electrode voltage. Furthermore, the spectroscopic studies allowed us to identify the O-O and O-OH surface intermediates on the Pt surface, suggesting that the associative ORR mechanism plays a critical role over a wide range of potentials. The spectroscopic studies also revealed that the Pt surface operates in two different ORR kinetic regimes as a function of the operating potential. At high voltage, the reaction rate is affected by the presence of the network of adsorbed OH and water, which makes it difficult for O_2 to find landing sites on the surface, and by the slow rates of proton-electron addition to the adsorbed O_2. On the other hand, at lower voltages the surface is clean, and the rate is controlled by the formation of the O-OH intermediate and its conversion to OH and O.

5.5 References

(1) Luo, M.; Sun, Y.; Zhang, X.; Qin, Y.; Li, M.; Li, Y.; Li, C.; Yang, Y.; Wang, L.; Gao, P.; Lu, G.; Guo, S. Stable High-Index Faceted Pt Skin on Zigzag-Like PtFe Nanowires Enhances Oxygen Reduction Catalysis. *Advanced Materials* **2018**. https://doi.org/10.1002/adma.201705515.

(2) Cleve, T. V.; Moniri, S.; Belok, G.; More, K. L.; Linic, S. Nanoscale Engineering of Efficient Oxygen Reduction Electrocatalysts by Tailoring the Local Chemical Environment of Pt Surface Sites. *ACS Catal.* **2017**, *7* (1), 17–24. https://doi.org/10.1021/acscatal.6b01565.

(3) Xin, H.; Holewinski, A.; Linic, S. Predictive Structure–Reactivity Models for Rapid Screening of Pt-Based Multimetallic Electrocatalysts for the Oxygen Reduction Reaction. *ACS Catal.* **2012**, *2* (1), 12–16. https://doi.org/10.1021/cs200462f.

(4) Huang, J.; Eikerling, M. Modeling the Oxygen Reduction Reaction at Platinum: A Brief Review of Recent Developments. *Current Opinion in Electrochemistry* **2019**. https://doi.org/10.1016/j.coelec.2019.01.004.

(5) Huang, X.; Zhao, Z.; Cao, L.; Chen, Y.; Zhu, E.; Lin, Z.; Li, M.; Yan, A.; Zettl, A.; Wang, Y. M.; Duan, X.; Mueller, T.; Huang, Y. High-Performance Transition Metal–Doped Pt3Ni Octahedra for Oxygen Reduction Reaction. *Science* **2015**, *348* (6240), 1230–1234. https://doi.org/10.1126/science.aaa8765.

(6) Zhang, G.-R.; Wöllner, S. Hollowed Structured PtNi Bifunctional Electrocatalyst with Record Low Total Overpotential for Oxygen Reduction and Oxygen Evolution Reactions. *Applied Catalysis B: Environmental* **2018**, *222* (Supplement C), 26–34. https://doi.org/10.1016/j.apcatb.2017.09.066.

(7) Wang, C.; Zhang, L.; Yang, H.; Pan, J.; Liu, J.; Dotse, C.; Luan, Y.; Gao, R.; Lin, C.; Zhang, J.; Kilcrease, J. P.; Wen, X.; Zou, S.; Fang, J. High-Indexed Pt3Ni Alloy Tetrahexahedral Nanoframes Evolved through Preferential CO Etching. *Nano Lett.* **2017**, *17* (4), 2204–2210. https://doi.org/10.1021/acs.nanolett.6b04731.

(8) Chen, C.; Kang, Y.; Huo, Z.; Zhu, Z.; Huang, W.; Xin, H. L.; Snyder, J. D.; Li, D.; Herron, J. A.; Mavrikakis, M.; Chi, M.; More, K. L.; Li, Y.; Markovic, N. M.; Somorjai, G. A.; Yang, P.; Stamenkovic, V. R. Highly Crystalline Multimetallic Nanoframes with Three-Dimensional Electrocatalytic Surfaces. *Science* **2014**, *343* (6177), 1339–1343. https://doi.org/10.1126/science.1249061.

(9) Jensen, K. D.; Tymoczko, J.; Rossmeisl, J.; Bandarenka, A. S.; Chorkendorff, I.; Escudero-Escribano, M.; Stephens, I. E. L. Elucidation of the Oxygen Reduction Volcano in Alkaline Media Using a Copper–Platinum(111) Alloy. *Angewandte Chemie International Edition* **2018**, *57* (11), 2800–2805. https://doi.org/10.1002/anie.201711858.

(10) Wang, D.; Xin, H. L.; Hovden, R.; Wang, H.; Yu, Y.; Muller, D. A.; DiSalvo, F. J.; Abruña, H. D. Structurally Ordered Intermetallic Platinum–Cobalt Core–Shell Nanoparticles with Enhanced Activity and Stability as Oxygen Reduction Electrocatalysts. *Nature Materials* **2013**, *12* (1), 81–87. https://doi.org/10.1038/nmat3458.

(11) Holewinski, A.; Linic, S. Elementary Mechanisms in Electrocatalysis: Revisiting the ORR Tafel Slope. *J. Electrochem. Soc.* **2012**, *159* (11), H864–H870. https://doi.org/10.1149/2.022211jes.

(12) Tripkovic, V.; Vegge, T. Potential- and Rate-Determining Step for Oxygen Reduction on Pt(111). *J. Phys. Chem. C* **2017**, *121* (48), 26785–26793. https://doi.org/10.1021/acs.jpcc.7b07472.

(13) Gómez-Marín, A.; Feliu, J.; Edson, T. Reaction Mechanism for Oxygen Reduction on Platinum: Existence of a Fast Initial Chemical Step and a Soluble Species Different from H2O2. *ACS Catal.* **2018**, 7931–7943. https://doi.org/10.1021/acscatal.8b01291.

(14) Ramaswamy, N.; Mukerjee, S. Fundamental Mechanistic Understanding of Electrocatalysis of Oxygen Reduction on Pt and Non-Pt Surfaces: Acid versus Alkaline Media. *Advances in Physical Chemistry* **2012**, *2012*, e491604. https://doi.org/10.1155/2012/491604.

(15) Jayasankar, B.; Karan, K. O2 Electrochemistry on Pt: A Unified Multi-Step Model for Oxygen Reduction and Oxide Growth. *Electrochimica Acta* **2018**, *273*, 367–378. https://doi.org/10.1016/j.electacta.2018.03.191.

(16) Huang, J.; Zhang, J.; Eikerling, M. Unifying Theoretical Framework for Deciphering the Oxygen Reduction Reaction on Platinum. *Physical Chemistry Chemical Physics* **2018**. https://doi.org/10.1039/C8CP01315B.

(17) Markovic, N.; Gasteiger, H.; Ross, P. N. Kinetics of Oxygen Reduction on Pt(Hkl) Electrodes: Implications for the Crystallite Size Effect with Supported Pt Electrocatalysts. *J. Electrochem. Soc.* **1997**, *144* (5), 1591–1597. https://doi.org/10.1149/1.1837646.

(18) Sui, S.; Wang, X.; Zhou, X.; Su, Y.; Riffat, S.; Liu, C. A Comprehensive Review of Pt Electrocatalysts for the Oxygen Reduction Reaction: Nanostructure, Activity, Mechanism and Carbon Support in PEM Fuel Cells. *Journal of Materials Chemistry A* **2017**, *5* (5), 1808–1825. https://doi.org/10.1039/C6TA08580F.

(19) Gauthier, J. A.; Ringe, S.; Dickens, C. F.; Garza, A.; Bell, A. T.; Head-Gordon, M.; Norskov, J. K.; Chan, K. Challenges in Modeling Electrochemical Reaction Energetics with Polarizable Continuum Models. *ACS Catalysis* **2018**. https://doi.org/10.1021/acscatal.8b02793.

(20) Sandoval-Rojas, A. P.; Gómez-Marín, A. M.; Suárez-Herrera, M. F.; Climent, V.; Feliu, J. M. Role of the Interfacial Water Structure on Electrocatalysis: Oxygen Reduction on Pt(1 1 1) in Methanesulfonic Acid. *Catalysis Today* **2016**, *262*, 95–99. https://doi.org/10.1016/j.cattod.2015.08.046.

(21) Che, F.; Gray, J. T.; Ha, S.; Kruse, N.; Scott, S. L.; McEwen, J.-S. Elucidating the Roles of Electric Fields in Catalysis: A Perspective. *ACS Catal.* **2018**, 5153–5174. https://doi.org/10.1021/acscatal.7b02899.

(22) Eslamibidgoli, M. J.; Eikerling, M. H. Approaching the Self-Consistency Challenge of Electrocatalysis with Theory and Computation. *Current Opinion in Electrochemistry* **2018**. https://doi.org/10.1016/j.coelec.2018.03.038.

(23) Sundararaman, R.; Goddard, W. A.; Arias, T. A. Grand Canonical Electronic Density-Functional Theory: Algorithms and Applications to Electrochemistry. *The Journal of Chemical Physics* **2017**, *146* (11), 114104. https://doi.org/10.1063/1.4978411.

(24) Stamenkovic, V. R.; Strmcnik, D.; Lopes, P. P.; Markovic, N. M. Energy and Fuels from Electrochemical Interfaces. *Nature Materials* **2017**, *16* (1), 57. https://doi.org/10.1038/nmat4738.

(25) Kunimatsu, K.; Yoda, T.; A. Tryk, D.; Uchida, H.; Watanabe, M. In Situ ATR-FTIR Study of Oxygen Reduction at the Pt / Nafion Interface. *Physical Chemistry Chemical Physics* **2010**, *12* (3), 621–629. https://doi.org/10.1039/B917306D.

(26) Shao, M. H.; Adzic, R. R. Spectroscopic Identification of the Reaction Intermediates in Oxygen Reduction on Gold in Alkaline Solutions. *J. Phys. Chem. B* **2005**, *109* (35), 16563–16566. https://doi.org/10.1021/jp053450s.

(27) Shao, M.; Liu, P.; Adzic, R. R. Superoxide Anion Is the Intermediate in the Oxygen Reduction Reaction on Platinum Electrodes. *J. Am. Chem. Soc.* **2006**, *128* (23), 7408–7409. https://doi.org/10.1021/ja061246s.

(28) Dong, J.-C.; Zhang, X.-G.; Briega-Martos, V.; Jin, X.; Yang, J.; Chen, S.; Yang, Z.-L.; Wu, D.-Y.; Feliu, J. M.; Williams, C. T.; Tian, Z.-Q.; Li, J.-F. In Situ Raman Spectroscopic Evidence for Oxygen Reduction Reaction Intermediates at Platinum Single-Crystal Surfaces. *Nature Energy* **2018**, 1. https://doi.org/10.1038/s41560-018-0292-z.

(29) Casalongue, H. S.; Kaya, S.; Viswanathan, V.; Miller, D. J.; Friebel, D.; Hansen, H. A.; Nørskov, J. K.; Nilsson, A.; Ogasawara, H. Direct Observation of the Oxygenated Species during Oxygen Reduction on a Platinum Fuel Cell Cathode. *Nature Communications* **2013**, *4*, 2817. https://doi.org/10.1038/ncomms3817.

(30) Nayak, S.; McPherson, I. J.; Vincent, K. A. Adsorbed Intermediates in Oxygen Reduction on Platinum Nanoparticles Observed by In Situ IR Spectroscopy. *Angewandte Chemie International Edition* **2018**, *57* (39), 12855–12858. https://doi.org/10.1002/anie.201804978.

(31) Aslam, U.; Linic, S. Addressing Challenges and Scalability in the Synthesis of Thin Uniform Metal Shells on Large Metal Nanoparticle Cores: Case Study of Ag–Pt Core–Shell Nanocubes. *ACS Appl. Mater. Interfaces* **2017**, *9* (49), 43127–43132. https://doi.org/10.1021/acsami.7b14474.

(32) Aslam, U.; Chavez, S.; Linic, S. Controlling Energy Flow in Multimetallic Nanostructures for Plasmonic Catalysis. *Nature Nanotechnology* **2017**, *12* (10), 1000–1005. https://doi.org/10.1038/nnano.2017.131.

(33) Chen, J. G.; Jones, C. W.; Linic, S.; Stamenkovic, V. R. Best Practices in Pursuit of Topics in Heterogeneous Electrocatalysis. *ACS Catal.* **2017**, *7* (9), 6392–6393. https://doi.org/10.1021/acscatal.7b02839.

(34) Moniri, S.; Van Cleve, T.; Linic, S. Pitfalls and Best Practices in Measurements of the Electrochemical Surface Area of Platinum-Based Nanostructured Electro-Catalysts. *Journal of Catalysis* **2017**, *345*, 1–10. https://doi.org/10.1016/j.jcat.2016.11.018.

(35) Nesselberger, M.; Ashton, S.; Meier, J. C.; Katsounaros, I.; Mayrhofer, K. J. J.; Arenz, M. The Particle Size Effect on the Oxygen Reduction Reaction Activity of Pt Catalysts: Influence of Electrolyte and Relation to Single Crystal Models. *J. Am. Chem. Soc.* **2011**, *133* (43), 17428–17433. https://doi.org/10.1021/ja207016u.

(36) Perez-Alonso, F. J.; McCarthy, D. N.; Nierhoff, A.; Hernandez-Fernandez, P.; Strebel, C.; Stephens, I. E. L.; Nielsen, J. H.; Chorkendorff, I. The Effect of Size on the Oxygen Electroreduction Activity of Mass-Selected Platinum Nanoparticles. *Angew. Chem. Int. Ed.* **2012**, *51* (19), 4641–4643. https://doi.org/10.1002/anie.201200586.

(37) Marimuthu, A.; Christopher, P.; Linic, S. Design of Plasmonic Platforms for Selective Molecular Sensing Based on Surface-Enhanced Raman Spectroscopy. *J. Phys. Chem. C* **2012**, *116* (17), 9824–9829. https://doi.org/10.1021/jp301443y.

(38) Boerigter, C.; Campana, R.; Morabito, M.; Linic, S. Evidence and Implications of Direct Charge Excitation as the Dominant Mechanism in Plasmon-Mediated Photocatalysis. *Nature Communications* **2016**, *7*, 10545. https://doi.org/10.1038/ncomms10545.

(39) Boerigter, C.; Aslam, U.; Linic, S. Mechanism of Charge Transfer from Plasmonic Nanostructures to Chemically Attached Materials. *ACS Nano* **2016**, *10* (6), 6108–6115. https://doi.org/10.1021/acsnano.6b01846.

(40) Chavez, S.; Rao, V. G.; Linic, S. Unearthing the Factors Governing Site Specific Rates of Electronic Excitations in Multicomponent Plasmonic Systems and Catalysts. *Faraday Discuss.* **2018**. https://doi.org/10.1039/C8FD00143J.

(41) Rao, V. G.; Aslam, U.; Linic, S. Chemical Requirement for Extracting Energetic Charge Carriers from Plasmonic Metal Nanoparticles to Perform Electron-Transfer Reactions. *J. Am. Chem. Soc.* **2019**, *141* (1), 643–647. https://doi.org/10.1021/jacs.8b11949.

(42) Aslam, U.; Rao, V. G.; Chavez, S.; Linic, S. Catalytic Conversion of Solar to Chemical Energy on Plasmonic Metal Nanostructures. *Nature Catalysis* **2018**, *1* (9), 656. https://doi.org/10.1038/s41929-018-0138-x.

(43) Chavez, S.; Aslam, U.; Linic, S. Design Principles for Directing Energy and Energetic Charge Flow in Multicomponent Plasmonic Nanostructures. *ACS Energy Lett.* **2018**, 1590–1596. https://doi.org/10.1021/acsenergylett.8b00841.

(44) Aslam, U.; Linic, S. Kinetic Trapping of Immiscible Metal Atoms into Bimetallic Nanoparticles through Plasmonic Visible Light-Mediated Reduction of a Bimetallic Oxide Precursor: Case Study of Ag–Pt Nanoparticle Synthesis. *Chem. Mater.* **2016**, *28* (22), 8289–8295. https://doi.org/10.1021/acs.chemmater.6b03381.

(45) Redox.me. Magnetic Mount Raman Electrochemical Flow Cell https://redox.me/collections/spectro-electrochemical-cells/products/raman-efc-4-mm-path-0-7-ml-raman-electrochemical-flow-cell.

(46) Hangaard Hansen, M.; Nilsson, A.; Rossmeisl, J. Modelling PH and Potential in Dynamic Structures of the Water/Pt(111) Interface on the Atomic Scale. *Physical Chemistry Chemical Physics* **2017**, *19* (34), 23505–23514. https://doi.org/10.1039/C7CP03576D.

(47) Skúlason, E.; Karlberg, G. S.; Rossmeisl, J.; Bligaard, T.; Greeley, J.; Jónsson, H.; Nørskov, J. K. Density Functional Theory Calculations for the Hydrogen Evolution Reaction in an Electrochemical Double Layer on the Pt(111) Electrode. *Phys. Chem. Chem. Phys.* **2007**, *9* (25), 3241–3250. https://doi.org/10.1039/B700099E.

(48) Osawa, M.; Tsushima, M.; Mogami, H.; Samjeské, G.; Yamakata, A. Structure of Water at the Electrified Platinum−Water Interface: A Study by Surface-Enhanced Infrared Absorption Spectroscopy. *J. Phys. Chem. C* **2008**, *112* (11), 4248–4256. https://doi.org/10.1021/jp710386g.

(49) Ataka, K.; Yotsuyanagi, T.; Osawa, M. Potential-Dependent Reorientation of Water Molecules at an Electrode/Electrolyte Interface Studied by Surface-Enhanced Infrared Absorption Spectroscopy. *J. Phys. Chem.* **1996**, *100* (25), 10664–10672. https://doi.org/10.1021/jp953636z.

(50) Otani, M.; Hamada, I.; Sugino, O.; Morikawa, Y.; Okamoto, Y.; Ikeshoji, T. Structure of the Water/Platinum Interface—a First Principles Simulation under Bias Potential. *Physical Chemistry Chemical Physics* **2008**, *10* (25), 3609–3612. https://doi.org/10.1039/B803541E.

(51) Tomonari, M.; Sugino, O. DFT Calculation of Vibrational Frequency of Hydrogen Atoms on Pt Electrodes: Analysis of the Electric Field Dependence of the Pt–H Stretching Frequency. *Chemical Physics Letters* **2007**, *437* (4), 170–175. https://doi.org/10.1016/j.cplett.2007.02.022.

(52) Kunimatsu, K.; Senzaki, T.; Tsushima, M.; Osawa, M. A Combined Surface-Enhanced Infrared and Electrochemical Kinetics Study of Hydrogen Adsorption and Evolution on a Pt Electrode. *Chemical Physics Letters* **2005**, *401* (4), 451–454. https://doi.org/10.1016/j.cplett.2004.11.100.

(53) Rizo, R.; Sitta, E.; Herrero, E.; Climent, V.; Feliu, J. M. Towards the Understanding of the Interfacial PH Scale at Pt(111) Electrodes. *Electrochimica Acta* **2015**, *162*, 138–145. https://doi.org/10.1016/j.electacta.2015.01.069.

(54) Zhu, S.; Qin, X.; Yao, Y.; Shao, M. PH-Dependent Hydrogen and Water Binding Energies on Platinum Surfaces as Directly Probed through Surface-Enhanced Infrared Absorption Spectroscopy. *J. Am. Chem. Soc.* **2020**. https://doi.org/10.1021/jacs.0c01104.

(55) Kunimatsu, K.; Sato, T.; Uchida, H.; Watanabe, M. Role of Terrace/Step Edge Sites in CO Adsorption/Oxidation on a Polycrystalline Pt Electrode Studied by in Situ ATR-FTIR Method. *Electrochimica Acta* **2008**, *53* (21), 6104–6110. https://doi.org/10.1016/j.electacta.2008.03.046.

(56) Janik, M. J.; McCrum, I. T.; Koper, M. T. M. On the Presence of Surface Bound Hydroxyl Species on Polycrystalline Pt Electrodes in the "Hydrogen Potential Region" (0–0.4 V-RHE). *Journal of Catalysis* **2018**. https://doi.org/10.1016/j.jcat.2018.09.031.

Chapter 6 Conclusions and Future Directions

6.1 General Conclusions

This dissertation presents a suite of tools and analysis to draw kinetic insights from electrocatalysts. In Chapter 3, the methods for ensuring accurate kinetic rate measurements are described. A modeling example is presented showing the effects of thin-film construction on kinetic rate measurements by calculating the Thiele modulus through a porous catalyst film and accurate surface area measurements. In Chapter 4, microkinetic modeling formalism is presented with an emphasis on shortcomings and recent developments to improve model accuracy. In Chapter 5, an in-operando study is presented, demonstrating the power of spectroscopic tools for reaction mechanism analysis. For the ORR, our study shows a crowded network of OH/H_2O at high potentials while a cleaner surface and OOH intermediates are observed at low potentials indicating an associative mechanism. Overall, this thesis provides a guide for future researchers to make impactful contributions in heterogeneous catalysis by leveraging both experimental and computational methods.

6.2 Future Directions

The methods and tools described in Chapters 2, 3, 4 and 5 can be expanded to many other electrochemical systems to yield powerful mechanistic insights. One electrochemical reaction where the reaction mechanism is still unknown is the hydrogen oxidation reaction (HOR). More specifically, the reaction rates drop several orders of magnitude (see Figure 6.1) when operating

the reaction at high pH (pH = 13) vs. low pH (pH = 1) for reasons still debated in the literature[1–5]. Alkaline exchange membrane fuel cells (AEMFCs) are a proposed alternative to PEMFCs where anions are transported across a selective membrane[6]. These types of fuel cells have the advantage of a basic environment around the cathodic electrocatalyst enabling a wider range of materials to be used due to their stability in alkaline condition. While opening a larger phase-space of cheaper materials at the cathode side, the amount of electrocatalyst at the anode (which is typically a small amount of Pt for PEMFCs) must be greatly increased due to the slow HOR kinetics, adding to the cost of the overall fuel cell. This in turn has a chilling effect on the commercialization of AEMFCs. The theories on the origin of this drastic pH-effect can be characterized by the following:

1. Co-adsorbed species (cations and/or interfacial water structure)
2. Bifunctional mechanism
3. Electric field effects

The first theory is that co-adsorbed species from the basic electrolyte block surface sites and alter the surface's catalytic activity, preventing the reaction. Cations such as K, Na and trace Pb, Fe, etc. can adsorb on the surface at the operating potentials (0-0.3 V). These cations are inherently part of the electrolyte (K and Na for KOH and NaOH) as opposed to an acidic electrolyte or are found as contaminants in basic electrolytes (Pb, Fe). One theory is that these co-adsorbed species alter the interfacial water structure preventing hydrogen adsorption, dissociation and/or oxidation to form water.

The second theory is that the instead of the posited Volmer step ($H^* + OH^- \rightarrow H_2O + e^- + *$) as the second step in the reaction mechanism, the reaction actually proceeds through an adsorbed OH^* by this step: $H^* + OH^* \rightarrow H_2O + 2^*$. This alternative mechanism would explain the slow kinetics as OH^* is not very abundant at such low potentials (though as discussed in Chapter 5, OH^* has

been observed at these potentials on higher index Pt facets[7]). This theory derives from works showing that added oxophilic species (such as $Ni(OH)_2$ and Ru) to the Pt surface greatly increased HOR activity[8,9].

The third theory is that due to the large differences in the electric fields in base vs. acid, the water organization and mobility is impacted preventing facile kinetics. Even though the reaction occurs at the same potential (0 V) vs. the reversible hydrogen electrode (RHE) at pH = 1 or pH = 13, the potential vs. the standard hydrogen electrode is very different (-0.059 V vs. -0.767 V, respectively). The point of zero free charge (pzfc, or pzc without contributions from adsorbed species) on platinum has been shown to be constant at 0.28 V vs. SHE regardless of pH[10], but the electric field through the double layer has been shown to increase[11] several orders of magnitude from ~0 V/m at pH = 1 to 10^8 V/m at pH = 7. This increased electric field strength has the effect of increasing the barrier for water reorganization which the theory posits is essential for facile hydrogen kinetics.

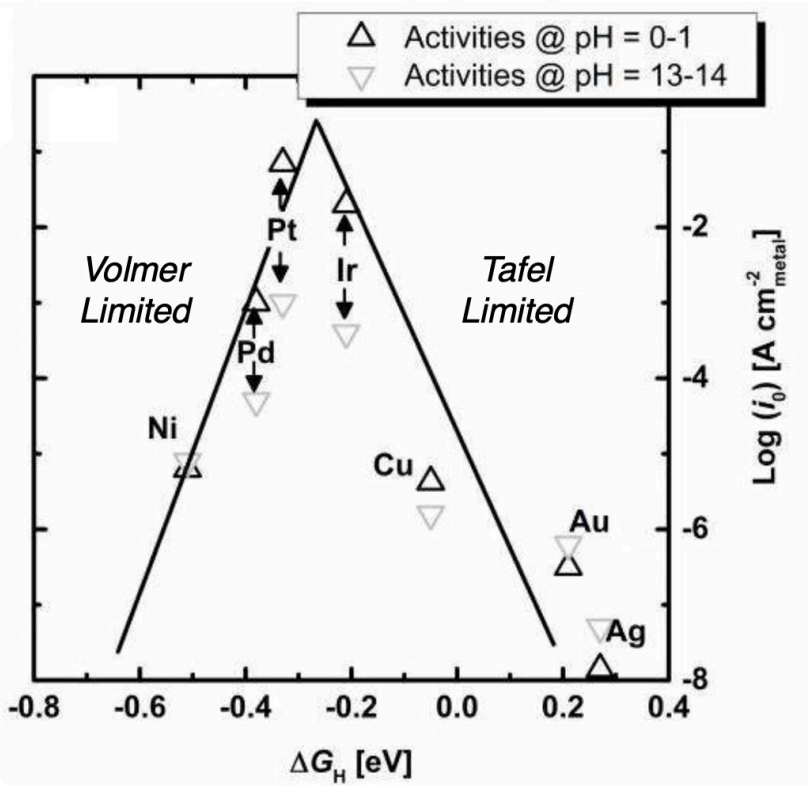


Figure 6.1 HOR exchange current densities for various metal electrocatlaysts with respect to hydrogen binding energy and pH. Adapted from ref [5].

Shedding light on the unexplained pH-effect of HOR activity can be accomplished using in-operando Raman spectroscopy. As shown in Chapter 5, interfacial structures and reaction intermediates were detected during reaction at a wide range of potentials. Due to the pH-effect it is necessary to collect spectrokinetic data at both high and low pH. To accomplish this, the core-shell Ag-Pt nanoparticles would need to be modified to ensure robust stability in acidic electrolytes. Switching of the silver core with a gold core could accomplish this as gold is stable at the operating potentials while gold is not. The Au-Pt nanoparticles would be synthesized and characterized, and using the methods in Chapter 3, their per area kinetic rates would be measured to ensure Pt HOR activity. A spectroscopic study like that of Chapter 5 would be conducted and with information on active structures at different potentials, a robust microkinetic model could be constructed using the methods detailed in Chapter 4.

Another simpler future direction could involve doping the Ag-Pt nanoparticles with oxophilic species (Ni islands) and performing in-operando analysis during HOR to see if there is an increase in OH species at the surface of the Pt nanoparticles. This study could help explain whether the bifunctional mechanism is occurring on Pt while simultaneously searching for indications of adsorbed electrolyte cations when the oxophilic species species are not present. Updated DFT surface structure models would be needed to include the effects of adsorbed cations.

6.3 References

(1) McCrum, I. T.; Koper, M. T. M. The Role of Adsorbed Hydroxide in Hydrogen Evolution Reaction Kinetics on Modified Platinum. *Nature Energy* **2020**, 1–9. https://doi.org/10.1038/s41560-020-00710-8.

(2) Rebollar, L.; Intikhab, S.; Oliveira, N. J.; Yan, Y.; Xu, B.; McCrum, I. T.; Snyder, J. D.; Tang, M. H. "Beyond Adsorption" Descriptors in Hydrogen Electrocatalysis. *ACS Catal.* **2020**, 14747–14762. https://doi.org/10.1021/acscatal.0c03801.

(3) Wang, F.; Xu, G.; He, Y.; Liu, Z.; Zhang, Z.; Mao, Q.; Huang, Y. Into the "Secret" Double Layer: Alkali Cation Mediates the Hydrogen Evolution Reaction in Basic Medium. *Journal of Energy Chemistry* **2020**. https://doi.org/10.1016/j.jechem.2020.03.037.

(4) Rebollar, L.; Intikhab, S.; Zhang, S.; Deng, H.; Zeng, Z.; Snyder, J. D.; Tang, M. H. On the Relationship between Potential of Zero Charge and Solvent Dynamics in the Reversible Hydrogen Electrode. *Journal of Catalysis* **2021**. https://doi.org/10.1016/j.jcat.2021.04.008.

(5) Durst, J.; Simon, C.; Siebel, A.; Rheinländer, P. J.; Schuler, T.; Hanzlik, M.; Herranz, J.; Hasché, F.; Gasteiger, H. A. (Invited) Hydrogen Oxidation and Evolution Reaction (HOR/HER) on Pt Electrodes in Acid vs. Alkaline Electrolytes: Mechanism, Activity and Particle Size Effects. *ECS Trans.* **2014**, *64* (3), 1069–1080. https://doi.org/10.1149/06403.1069ecst.

(6) Gu, S.; Cai, R.; Luo, T.; Zhongwei, C.; Minwei, S.; Yan, L.; Gaohong, H.; Yushan, Y. A Soluble and Highly Conductive Ionomer for High-Performance Hydroxide Exchange Membrane Fuel Cells. *Angewandte Chemie International Edition* **2009**, *48* (35), 6499–6502.

(7) Janik, M. J.; McCrum, I. T.; Koper, M. T. M. On the Presence of Surface Bound Hydroxyl Species on Polycrystalline Pt Electrodes in the "Hydrogen Potential Region" (0–0.4 V-RHE). *Journal of Catalysis* **2018**. https://doi.org/10.1016/j.jcat.2018.09.031.

(8) Strmcnik, D.; Uchimura, M.; Wang, C.; Subbaraman, R.; Danilovic, N.; Vliet, D. van der; Paulikas, A. P.; Stamenkovic, V. R.; Markovic, N. M. Improving the Hydrogen Oxidation Reaction Rate by Promotion of Hydroxyl Adsorption. *Nat Chem* **2013**, *5* (4), 300–306. https://doi.org/10.1038/nchem.1574.

(9) Li, J.; Ghoshal, S.; Bates, M. K.; Miller, T. E.; Davies, V.; Stavitski, E.; Attenkofer, K.; Mukerjee, S.; Ma, Z.-F.; Jia, Q. Experimental Proof of the Bifunctional Mechanism for the Hydrogen Oxidation in Alkaline Media. *Angewandte Chemie International Edition* **2017**, *56* (49), 15594–15598. https://doi.org/10.1002/anie.201708484.

(10) Rizo, R.; Sitta, E.; Herrero, E.; Climent, V.; Feliu, J. M. Towards the Understanding of the Interfacial PH Scale at Pt(111) Electrodes. *Electrochimica Acta* **2015**, *162*, 138–145. https://doi.org/10.1016/j.electacta.2015.01.069.

(11) Ryu, J.; Surendranath, Y. Tracking Electrical Fields at the Pt/H2O Interface during Hydrogen Catalysis. *J. Am. Chem. Soc.* **2019**. https://doi.org/10.1021/jacs.9b05148.